6-30-2016

Ultrathin Microporous Metal Oxide Coatings: Preparation by Molecular Layer Deposition, Characterization And Application

Zhuonan Song
University of South Carolina

ULTRATHIN MICROPOROUS METAL OXIDE COATINGS: PREPARATION BY MOLECULAR LAYER DEPOSITION, CHARACTERICATION AND APPLICATION

by

Zhuonan Song

Bachelor of Engineering
Dalian University of Technology, 2012

Submitted in Partial Fulfillment of the Requirements

For the Degree of Doctor of Philosophy in

Chemical Engineering

College of Engineering and Computing

University of South Carolina

2016

Accepted by:

Miao Yu, Major Professor

John R. Regalbuto, Committee Member

James A. Ritter, Committee Member

John W. Weidner, Committee Member

Aaron K. Vannucci, Committee Member

Lacy Ford, Senior Vice Provost and Dean of Graduate Studies

DEDICATION

To my wife, my parents, my parents-in-law and my grandparents.

ACKNOWLEDGEMENTS

First of all, I would like to express my deepest gratitude to Professor Miao Yu, my advisor, for his support, encouragement, and patience during these four years graduate study in his research group. Under his guidance, I have learnt a lot, including sense of deep thinking, scientific writing and presentation skills, which would be extremely beneficial to my entire career. I would never have been able to complete this thesis without his help. Sincere thanks also go to my committee members: Professor John Regalbuto, Professor James Ritter, Professor John Weidner, and Professor Aaron Vannucci for their valuable time and precious advices.

I would like to thank all the former and current group members in Yu's group: Dr. Xiaojie Zhang, Dr. Yi Huang, Dr. Mahdi Fathizadeh, Dr. Konstantin Khivantsev, Dr. Huynh Ngoc Tien, Hang Li, Lei Wang, Weiwei Xu, and Fanglei Zhou, for many useful suggestions and discussions about my research. Especially, I thank Dr. Xiaojie Zhang, for building and testing the atomic layer deposition system. And Dr. Yi Huang, for his kind instructions on a lot of technical characterization facilities. Additionally, I would like to thank Dr. Shiguang Li from Gas Technology Institute, Professor Moises Carreon, Zhaowang Zong, and Xuhui Feng from Colorado School of Mines, for their valuable collaborations.

I want to thank all my dear friends in Columbia for the wonderful time including: Qiuli Liu, Yiying Wang, Chao Wang, Zhiyong Wang, Weijian Diao, Yiling Dai, Fan Wu,

Yating Mao, Yunya Zhang, Shuo Cao, Tianyuan Xie, Shuai Tan, Lichao Sun, Qingfeng Zhang et al.

I would like to thank the staff in the Chemical Engineering department at University of South Carolina, especially, Charles Holland, for his help in building the pressure transducer system.

Last but not least, I am truthfully grateful to my wife, Weizhuo, and my family for their continuous love and support.

ABSTRACT

Molecular layer deposition (MLD), a gas phase deposition technique, was applied to deposit conformal organic-inorganic hybrid coatings by conducting a series of sequential, self-limiting surface reactions on substrates with exquisite thickness control at the sub-nanometer level. Obtained organic-inorganic hybrid coatings can subsequently be converted into porous coatings by removing the organic compound. Potential of functional coatings and membranes prepared by MLD was explored for applications from adsorptive separation, water purification, to gas storage.

We demonstrated a new concept, pore misalignment, to continuously fine tune the molecular-sieving "gate" of 5A zeolite by adjusting the external porous Al_2O_3 MLD coating thickness. For the first time, small organic molecules with sub-0.01 nm size differences were effectively distinguished by size. As an extension of the pore misalignment concept, a composite zeolite adsorbent was prepared by depositing an ultrathin porous TiO_2 coating on 5A zeolite by MLD. This composite adsorbent showed great potential for effective C_3H_6/C_3H_8 separation based on both equilibrium and adsorption kinetics differences (approximately 5 times higher ideal adsorption selectivity and 44 times higher diffusivity, compared to uncoated 5A zeolite). MLD coated zeolite (5A and 13X) composite adsorbents were also found to have great potential for CO_2 capture from flue gases; greatly enhanced CO_2/N_2 ideal adsorption selectivity was obtained, while maintaining high CO_2 adsorption capacity, by controlling calcination conditions.

Molecular layer deposition was also used as a highly controllable method to prepare TiO_2 nanofiltration membranes by depositing microporous TiO_2 coating on mesoporous anodic aluminum oxide (AAO) support with excellent control of coating quality, thickness and nanometer-sized membrane pores for water purification. Optimized TiO_2 nanofiltration membranes had a pure water permeability as high as ~48 L/(m^2·h·bar). Salt and dye rejection measurements showed moderate rejection of Na_2SO_4 (43%) and $MgSO_4$ (35%) and high rejection of methylene blue (~96%). In addition, natural organic matter (NOM) removal testing showed high rejection (~99%) as well as significantly improved antifouling performance and recovery capability.

A novel concept of utilizing nanoporous coatings as effective nano-valves on microporous adsorbents was developed for high capacity natural gas storage at low storage pressure. For the first time, the concept of nano-valved adsorbents capable of sealing high pressure CH_4 inside the adsorbents and storing it at low pressure was demonstrated. Traditional natural gas storage tanks are thick and heavy, which makes them expensive to manufacture and highly energy-consuming to carry around. Our design uses unique adsorbent pellets with nano-scale pores surrounded by a coating that functions as a valve to help manage the pressure of the gas and facilitate more efficient storage and transportation. The optimal nano-valved adsorbents comprise of a ~7.5 μm thick MCM-48 mesoporous layer coated on the outer surface of 5A beads. After modification by 3 cycles of MLD, the steady state CH_4 storage capacity of MLD-MCM-48-5A adsorbent (loading pressure 50 bar, storage pressure 1 bar) was about 55.8-58.4% (40.7-42.6 V/V) of the maximum capacity of the uncoated 5A beads in three CH_4 storage cycles, which is about 200% higher than storage capacity of the uncoated 5A beads at the same storage pressure.

TABLE OF CONTENTS

LIST OF TABLES

LIST OF FIGURES

LIST OF ABBREVIATIONS

AAO ..... Anodic Aluminum Oxide

ADOR ..... Assembly Disassembly Organization Reassemble

AFM ..... Atomic Force Microscopy

ALD ..... Atomic Layer Deposition

ALE ..... Atomic Layer Epitaxy

ANG ..... Adsorbed Natural Gas

BET ..... Brunauer Emmett Teller

COF ..... Covalent Organic Framework

CNG ..... Compressed Natural Gas

CTAB ..... Cetyltrimethyl Ammonium Bromide

CVD ..... Chemical Vapor Deposition

DMB ..... Dimethylbutane

EG ..... Ethylene Glycol

EDX ..... Energy Dispersive X-ray Spectroscopy

FESEM ..... Field Emission Scanning Electron Microscopy

GC ..... Gas Chromatography

LNG ..... Liquefied Natural Gas

MB ..... Methylene Blue

MF ..... Microfiltration

MLD ..... Molecular Layer Deposition

MMFF ..... Molecular Mechanics Force Field

MOF ..... Metal Organic Framework

NF ..... Nanofiltration

NGV ..... Natural Gas Vehicle

NOM ..... Natural Organic Matter

CDRI ..... Central Drug Research Institute

PDMS ..... Polydimethylsiloxane

PVD ..... Physical Vapor Deposition

QCM ..... Quartz Crystal Microbalance

RO ..... Reverse Osmosis

SRHA ..... Suwannee River Humic Acid

TEM ..... Transmission Electron Microscopy

TFEL ..... Thin Film Electroluminescence

TMA ..... Trimethylaluminum

UF ..... Ultrafiltration

XPS ..... X-ray Photoelectron Spectroscopy

XRD ..... X-ray Diffraction

XRR ..... X-ray Relectivity

ZIF ..... Zeolitic Imidazolate Framework

CHAPTER 1

INTRODUCTION AND LITERATURE REVIEW

1.1 SEPARATION BASED ON ADSORPTIVE PROCESS

Mixture separation constitutes a large and costly component of chemical and petrochemical industrial processes. [1] Various separation technologies, such as solvent extraction, distillation, crystallization, and adsorption etc., have been applied to separate mixtures. [2] Among these technologies, separation based on adsorptive process, has been widely considered as a low operation cost, low energy requirement, and low maintenance method.[3-6] Adsorptive separation can be achieved based on the differences on either the strength of adsorption (equilibrium-based separation) or the rate of adsorption (kinetics-based separation).[7] Most of the adsorptive separation processes are equilibrium-based separation due to easier design and operation.[8] The core of the adsorptive separation process is adsorbent. An effective adsorbent is capable of separating one component from another based on the different interactions with them. In addition, adsorbents should also possess high surface area, high porosity, reversible adsorption/desorption capability, structure stability, and potential for surface modification.[9, 10] Adsorbents can be classified into selective adsorption adsorbents and molecular sieving adsorbents based on separation mechanism.[11] For selective adsorption adsorbents, which are the most studied, the desired component interacts with adsorbents more strongly and thus result in a more preferential equilibrated uptake versus the other.[12-14] In contrast, the much less

extensively reported molecular sieving adsorbents are relying on size exclusion.[15, 16] Apparently, development of more energy-efficient adsorptive separation process is strongly related with the characteristics of the adsorbents.

Many porous materials have been prepared and explored for adsorptive separation processes, including porous polymer,[17] activated carbon,[18] carbon nanotube,[19] carbon molecular sieves[20], zeolites,[21-23] mesoporous metal oxides,[24] metal organic frameworks (MOFs),[5] and zeolitic imidazolate frameworks (ZIFs) [7]. Among them, zeolites are one of the most promising adsorbents that may realize true molecular-sieving separation under harsh separation conditions, attributing to their uniform, molecular-sized pores and high chemical, thermal and mechanical stabilities.[25]

1.1.1 CRYSTALLINE MICROPOROUS MATERIAL: ZEOLITES

Zeolites are crystalline aluminosilicates with uniform micropores in the range of 0.3 ~ 1.3 nm, and have been widely used as catalysts, ion-exchangers and adsorbents.[26, 27] They are well known as 'molecular sieves', due to their molecular-sized pores, which only allow molecules smaller than the pore size to diffuse into, while excluding larger molecules. Zeolite structures are composed of an infinitely extended three-dimensional, corner-sharing AlO_4 and SiO_4 tetrahedra linked to each other by sharing of oxygen atoms.[28] Each tetrahedral atom (T atom) is connected to four oxygen atoms, and each oxygen atom is connected to two T atoms, where T may also be B, Ge, and Ga.[29, 30] A pure tetravalent (Si, and Ge) framework is neutral. The presence of trivalent atoms (Al, B and Ga) in the framework results in a net negative charge, which is balanced by cations such as K^+, Na^+ and Ca^{2+} [31, 32]. The cations are relatively mobile and can be exchanged with other cations.[33] Up to now more than 200 distinct framework structures of zeolites

are known.[34] Each known framework structure is assigned a three letter code by international zeolite associate (IZA).[35] For example, LTA is for linde type A [36], MFI is for ZSM-5 [37], FAU is for faujasite [38], and CHA is for chabazite [39].

Zeolites have been studied and applied as adsorbent for many applications. Zeolite 4A (LTA-type zeolite) was studied for propylene/propane adsorptive separation.[23] Zeolite ZSM-5 (MFI-type zeolite) and zeolite Y (FAU-type zeolite) were studied for removal of CO_2 from CO_2/CH_4 mixture by adsorptive separation.[22] Zeolite 13X (FAU-type zeolite) and zeolite 5A (LTA-type zeolite) were widely studied for CO_2 capture from CO_2/N_2 mixture.[40, 41] Zeolite NaKA (potassium exchanged LTA-type zeolite) showed preferential adsorption of oxygen over nitrogen. [16] However, the pore sizes of traditional zeolites are relative fixed and discrete from each other; for example, the well-known pore openings are 0.38, 0.50, and 0.74 nm for SAPO-34 [42], 5A [36] and 13X zeolite [43]. It is difficult to achieve highly efficient adsorptive separation for molecules with small size differences without modification of zeolite pore sizes.

Pore size and/or structure of zeolites can be adjusted by several techniques.[44-47] Ion exchange has been used as an effective way of adjusting the pore sizes of LTA-type zeolites.[32] The framework of some zeolites, such as zeolite rho, may deform substantially upon adsorption of some molecules, [44] ion-exchange, dehydration, and cation relocation.[45, 46] A molecular sieve, ETS-4, has been shown to contract gradually through dehydration at elevated temperatures so that its effective pore size can be adjusted at approximately 0.01 nm step.[47] Despite a large selection pool of zeolites/molecular sieves and available techniques to adjust their pore sizes, not all desired pore sizes can be obtained for target separations. This is especially the case for separating molecules that are

very close in size. In addition, pore modification and structure changes were always realized by sacrificing adsorption capacity or internal cavity. [11, 47-49]

1.1.2 ADSORPTION ISOTHERM MEASUREMENT

Adsorption is usually described through isotherms, that is, the amount of adsorbate (the molecule being adsorbed) on the adsorbent as a function of equilibrium pressure (gas or vapor phase). The most common experimental technique for determining single component adsorption isotherm is volumetric method (Figure 1.1) [50]. In the volumetric method, the equilibrium adsorption uptake amount is measured in two steps. In the first step, a specific gas/vapor is confined in a calibrated volume (reference tank), and the amount of the gas/vapor in the reference tank can be calculated from the volume, temperature, and pressure. In the second step, the valve is then opened and the gas/vapor is expanded into the adsorption tank with a known amount of adsorbent and allowed to equilibrate. The equilibrium amount of adsorbate in the gas/vapor phase can be calculated from the final pressure, temperature, and the total volume of the system. The difference between the initial amount and the amount in the gas/vapor phase at equilibrium is the adsorbed amount. The volume of the adsorption tank with adsorbent is calibrated using helium. Commonly, helium is assumed not to adsorb.[51] The next point on the adsorption isotherm is then obtained by adding another calibrated dose of gas/vapor at higher pressure and repeating the process. Another experimental method for measuring adsorption isotherm is gravimetric method.[52] In the gravimetric method, the adsorption uptake capacity is determined from weight change of adsorbent, after exposure to a specific gas/vapor.

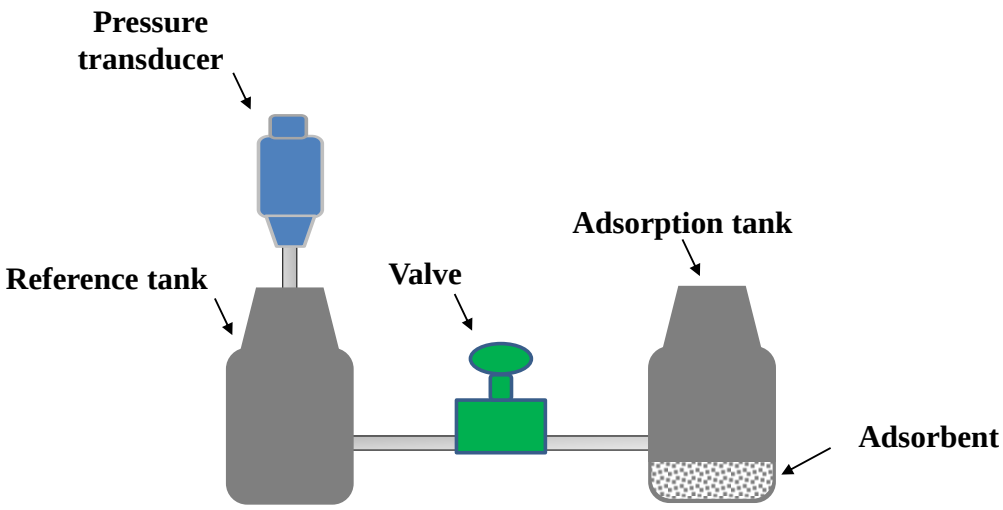

Figure 1.1 Schematic representation of the experimental set up of volumetric method for adsorption isotherm measurement.

1.2 SEPARATION BASED ON MEMBRANE PROCESS

Besides adsorptive separation, membrane separation is also considered to be an energy-efficient alternative to conventional separation processes.[53, 54] A membrane is defined as a selective barrier between two homogeneous phases [55]. The influent of a membrane is called the feed, and a feed flows into one side of a membrane and separates into two streams: retentate (on the same side as the feed) and permeate (on the other side of the membrane), as shown in Figure 1.2. The driving force for membrane separation is a gradient of chemical potential or electrical potential between two separated phases at each side of the membrane [56]. Some components are allowed to permeate through the membrane into a permeate stream, whereas others are retained in the retentate stream. Membrane separation is widely used for both gas separation and liquid filtration. The separation performance of a membrane can be characterized by two fundamental properties: one is mass transport rate, and the other one is separating capability.

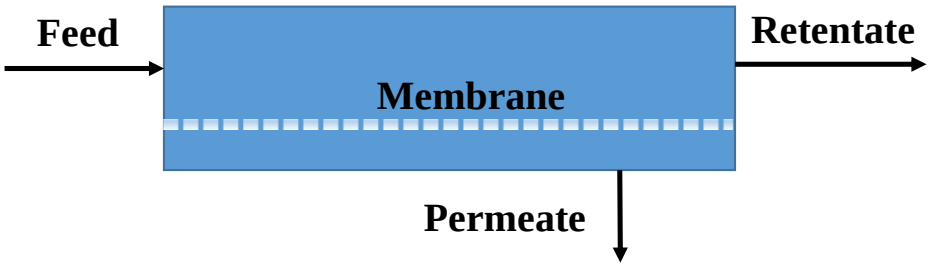

Figure 1.2 Schematic representation of the membrane-based separation process.

For gas separation membrane, the mass transport rate is represented by permeability, and separating capability is represented by selectivity. [57] For a pure gas (A) permeating through a membrane, the permeability P_A is defined as:

$$P_A = (N_A) \times (l)/(\Delta p_A) \tag{1.1}$$

where l is the membrane thickness, N_A is the steady-state gas flux, and Δp_A is the pressure difference between upstream and downstream. Selectivity of a membrane to separate two gases is defined as follows:

$$\alpha_{AB} = P_A/P_B \tag{1.2}$$

where P_A and P_B are the permeability of gases A and B, respectively.

Gas separation membranes have been applied and/or widely studied in natural gas purification (removal of CO_2 and H_2S), CO_2 capture (removal CO_2 from flue gas), hydrogen recovery from ammonia purge gas, olefin/paraffin separation, and nitrogen enrichment (oxygen-nitrogen separation) [58-61].

For liquid filtration membranes, the mass transport rate is represented by flux; and separating capability is represented by rejection (retention) [62]. Flux is defined as the liquid volume flowing though the membrane per unit area, and per unit time:

$$J = V/(A_m \times t) \tag{1.3}$$

where V is the total collected volume of the permeate after permeation time t, A_m is the membrane area. Rejection is calculated as a function of the permeate concentration and feed concentration by:

$$R = \left(1 - \frac{c_p}{c_f}\right) \times 100\% \tag{1.4}$$

where c_p and c_f is the concentration of solute in the permeate and feed solution, respectively.

Liquid filtration, including microfiltration (MF), ultrafiltration (UF), nanofiltration (NF), and reverse osmosis (RO) as listed in Table 1.1, is typically carried out by a pressure-driven process. MF membranes have the largest pore size typically from 10 to 0.1 μm, and normally operate under low pressure (< 1 bar) [63]. UF membranes are also recognized as a low-pressure membrane filtration process [64], with pore sizes from 0.1 to 0.01 μm [65]. Pore size of NF membranes ranges from 0.01 to 0.001 μm [66], and RO membranes have the smallest pore size (< 0.001 μm) [67].

Table 1.1: Comparison of liquid filtration membranes

Membrane type	Symbol	Pore size, μm	Operating pressure, bar
Microfiltration	MF	10.0-0.1	<1
Ultrafiltration	UF	0.1-0.01	1-3.5
Nanofiltration	NF	0.01-0.001	5-20
Reverse Osmosis	RO	<0.001	15-70

Among these pressure-driven liquid filtration processes, NF membranes are relatively recently developed. They are now widely used in water treatment for drinking water production and wastewater treatment, as well as pretreatment for desalination owing to their ability to completely remove suspended solids, bacteria, viruses, and partially remove some multivalent ions (Figure 1.3).[68-71] Comparing with traditional RO membrane, NF membranes offer the potential for a wider range of ion selectivity and can be operated at a relatively low pressure drop with a higher flux.[72] This opens lots of doors for a variety of separation applications across many industries, ranging from sulfate removal from sea water to lactose concentration in demineralization of dairy processing, to the concentration of sugars in the food industry, as well as the wastewater treatment in textile printing and dyeing industry.[70] NF membranes are generally classified into two major groups based on membrane material: organic/polymeric and inorganic ceramic membranes.[73] The dominant material of NF membranes is polymers, such as cellulose acetate, polyamide, polyimide, and poly(ether)sulfone.[70, 74] Most of the polymeric NF membranes have advantages of flexibility, simple preparation process, and relatively low cost.[68] However, their application is limited to moderate temperature and feed streams that are not too corrosive.[73] Ceramic NF membranes are usually manufactured from inorganic material, such as alumina (Al_2O_3), zirconia (ZrO_2), silica (SiO_2), and titania (TiO_2).[75, 76] Comparing with polymeric NF membranes, ceramic NF membranes have better chemical (pH 1-14), thermal (up to 500℃) and mechanical stability, long lifetime, and thus may be used in applications under extreme operating conditions.[68] Currently, ceramic NF membranes are usually prepared by solution-based sol-gel method.[77, 78] The basic idea is the hydrolysis of metal akoxide; the hydrolysis reaction rate is very fast,

and many factors may influence the membrane quality. Typically, in this process, a gel needs to be carefully prepared from a colloidal or polymeric solution by adding organic additives to control the hydrolysis and condensation of alkoxides.[79, 80] In addition, membrane thickness cannot be precisely controlled at the sub-nanometer scale. This may severely limit sol-gel method for preparing ultrathin, high flux ceramic NF membranes. More importantly, pore sizes of ceramic NF membranes, prepared by the sol-gel method, are difficult to be precisely controlled at about 1 nm, especially for stable metal oxides, such as TiO_2. Attempts to prepare TiO_2 NF membranes started from 1990s, and the average pore sizes obtained in these initial studies were in the range of 1.5~4.0 nm.[79-83] To date, the tightest reported TiO_2 NF membranes, prepared by optimizing the sol-gel processing conditions, had a pore size of ~0.9 nm.[77, 80] Hydrolysis conditions of titanium alkoxides, however, need to be strictly controlled because of the extremely fast hydrolysis rate to avoid any local excess of water at any moment.[77] Therefore, new methods with easier operations, and better thickness and pore size control are needed for ceramic NF membrane preparation.

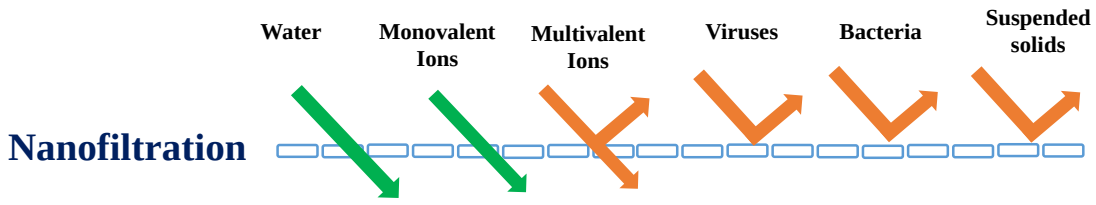

Figure 1.3 Nanofiltration membrane process characteristics.

1.3 METHANE STORAGE

Methane, the predominant component of natural gas, is considered as an alternative clean fuel for vehicles due to the lowest ratio of CO_2 emissions to energy supplied. [84-86]

In recently years, the fracking technology dramatically makes natural gas retrieving from shale much more cost-effective.[86] Therefore, there is an increasing concentration on the development of natural gas vehicles (NGV). However, the widespread use of methane as fuel for transportation depends on safe and high-energy density storage of methane. Natural gas is typically stored in a cryogenic tank as liquefied natural gas (LNG) at 113 K due to the low critical temperature of methane (T_c = 191 K) or as compressed natural gas (CNG) at 200-300 bar in pressure vessels which requiring an heavy equipment and expensive multistage compression.[85, 87] A promising alternative is adsorbed natural gas (ANG), where the gas is stored as an adsorbed phase in porous materials. However, CH_4 storage capacity of current adsorbents at ambient temperature and moderate pressure, typically at 35 bar, is much lower than the CH_4 storage volumetric target set by U.S. Department of Energy (DOE) which corresponds to 263 V (STP: 273.15 K, 1 atm)/V.[86, 88] Therefore, it is critical to develop a new method capable of storing high capacity CH_4 within the adsorbents at a relatively low pressure that facilitates more efficient storage and transportation.

1.4 ATOMIC/MOLECULAR LAYER DEPOSITION

Atomic layer deposition (ALD), originally called atomic layer epitaxy (ALE), was invented in the 1970s by T. Suntala and coworkers for producing high-quality, large-area flat panel displays based on thin film electroluminescence (TFEL).[89] In the early days of its development, ALD was limited to deposit epitaxial layers of II-VI or III-V semiconductors.[90] However, the requirement of nano-thin films and miniaturization of devices in semiconductor industry has led to the enormous development of ALD in recent years.[91] To date, ALD is considered as a powerful technology for depositing conformal

thin films, such as metal oxides [92], nitrides [93], sulfides [94], and metals [95] with the thickness down to several nanometers.

ALD is based on sequential, self-limiting surface reactions to deposit thin films in a cyclic manner. Most of the ALD processes use two chemicals, typically called precursors. Normally one growth cycle consists of six steps: 1) exposure of the substrate surface to the first precursor, 2) chemisorption of the first precursor onto the substrate, 3) purge of the reaction chamber with inert gas to remove the excess unreacted precursor and by-products, 4) exposure of the substrate surface to the second precursor, 5) surface reaction to produce the thin film, and 6) a further purge of the reaction chamber to remove the second unreacted precursor and by-products.[96] The growth cycles are repeated as many times as required for the desired film thickness. A schematic showing the successive, self-limiting surface reactions during Al_2O_3 ALD is illustrated in Figure 1.4. ALD of Al_2O_3 using trimethylaluminum (TMA) and water is one of the most commonly studied ALD processes, because of its wide applications and ease of growth on a wide range of substrates. As with any ALD process, the reactions on the surface can be separated into two half reactions:

$$Al\text{-}OH^* + Al(CH_3)_3 \rightarrow Al\text{-}O\text{-}Al\text{-}CH_3^* + CH_4 \quad (1.5)$$

$$Al\text{-}CH_3^* + H_20 \rightarrow Al\text{-}OH^* + CH_4 \quad (1.6)$$

where the asterisks denote the surface species.

Molecular layer deposition (MLD) is similar to ALD and can be used to deposit ultrathin inorganic-organic hybrid films with precise control of thickness on a variety of substrates.[97-99] During deposition, again two self-limiting half reactions are used alternately to introduce metal source and organic source into the hybrid film. Each set of

half-reaction deposits a layer that conforms to the surface of the underlying substrates. A layer of desired thickness can be deposited by repeating the reaction sequence. The film thickness can be controlled at the sub-nanometer level because each half reaction is self-limiting. MLD growth has been demonstrated for a variety of organic-inorganic hybrid coatings by using suitable metal and organic precursors [100]. One of the first examined hybrid organic-inorganic materials grown by MLD was "alucone" based on the reaction between TMA and ethylene glycol (EG) [101]. The EG molecule, HO-CH_2-CH_2-OH, contains two hydroxyls groups and is analogous to H_2O as a reactant in Al_2O_3 ALD. The difference is that the -CH_2-CH_2- molecular fragment is introduced into the hybrid organic-inorganic film. A schematic showing the growth of the alucone based on TMA and EG is displayed in Figure 1.5. In the first half-reaction, TMA reacts with surface hydroxyl groups to generate CH_4 and replace hydroxyl groups with methyl groups; after removing gas phase excess TMA, ethylene is introduced to react with terminal methyl groups and regenerate surface hydroxyl groups. This vapor-phased based deposition method does not require solvents or catalysts [100], and operates at relatively low temperature (100 - 175 ºC) [36, 101].

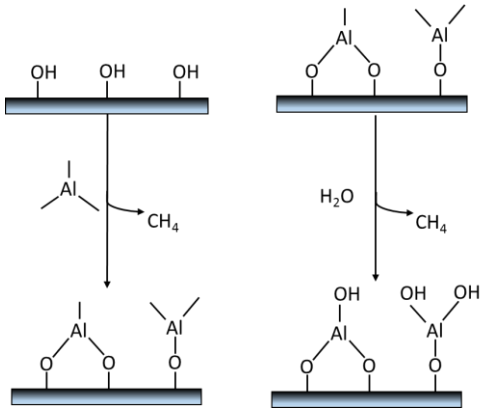

Figure 1.4 Illustration of surface chemistry for Al_2O_3 ALD using TMA and H_2O as precursors.

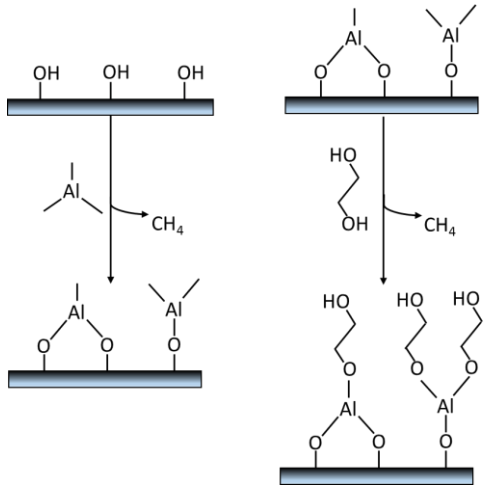

Figure 1.5. Schematic depicting alucone MLD growth using TMA and EG.

Compared with the dense inorganic coatings prepared by ALD, MLD growth has been demonstrated for a variety of organic-inorganic hybrid coatings by using suitable metal and organic precursors.[100] The obtained organic-inorganic hybrid coatings can subsequently be converted into porous coatings by removing the organic compound by calcination in air, annealing or wet-etching procedures [36, 102-104].

1.4.1 CHARACTERISTICS OF MOLECULAR LAYER DEPOSITION

MLD has its own distinct advantages over other coating deposition methods. First, MLD provides exquisite control of the coating thickness down to several angstroms by its layer-by-layer growth mechanism. Taking alucone MLD for example, the coating thickness grows linearly with the number of MLD cycles with a growth rate of 0.4 Å/cycle at 175 ℃ [101]. Second, MLD can achieve conformal, pinhole free, and uniform coating on substrates even with high-aspect-ratio features/complex three-dimensional (3D) structures because of its self-limiting nature. [105, 106] Physical vapor deposition (PVD) and chemical vapor deposition (CVD) are well-known thin film deposition techniques.

However, compared with MLD, PVD shows very poor step coverage and limited rearrangement, and line-of-sight deposition. Films prepared by PVD will be coated more heavily directly above the source. Therefore, large surface area or higher aspect ratio substrates can not be coated uniformly. CVD has been widely used for depositing coatings on substrates with high aspect ratio features with the presence of laminar gas flow. MLD is a special variant of the well-known chemical vapor deposition (CVD) method. However, the difference between MLD and CVD is obvious. CVD techniques are not able to effectively control the use of precursors because the precursors react at the same time on the surface and in the gas phase and precursors can decompose, whereas MLD comprises of self-limiting chemical reactions between precursors and a surface. In addition, CVD will leave defects and pinholes in the deposited film,[107-109] whereas the self-limiting nature of MLD gives rise to a conformal growth behavior and an additional control over the whole coating thickness.

1.4.2 CHARACTERIZATION TECHNIQUES FOR MOLECULAR LAYER DEPOSITION

In situ mass spectrometry can be used to monitor products in gas phase and reactants in the MLD reactions [98]. In situ quartz crystal microbalance (QCM) can be used to examine the growth dynamics of the deposition [110]. X-ray reflectivity (XRR) can be used for evaluating MLD coating growth rate and density [110]. The crystallinity of the MLD coatings can be examined by X-ray diffraction (XRD) [36]. The topography and roughness of the MLD coating can be investigated by using atomic force microscopy (AFM) [111]. Fourier transform infrared (FTIR) spectroscopy can be applied for analyzing the chemical state of the MLD coatings [112, 113]. The composition of the MLD coating

can be studied by X-ray photoelectron spectroscopy (XPS) [36]. Transmission electron microscopy (TEM) was used to observe MLD coating thickness and estimate the MLD coating growth rate [36, 103]. Pore size distribution of porous MLD coatings can be calculated by using N_2 adsorption isotherm at -196 °C [114].

1.4.3 APPLICATIONS OF MOLECULAR LAYER DEPOSITION

MLD can be used to deposit conformal organic-inorganic hybrid coatings with precisely controlled thickness, and the hybrid coating can be subsequently converted into ultrathin porous coatings after removing the organic components. Therefore, MLD has been explored for applications in many areas, such as surface modification, nanoparticle encapsulation, and photocatalytic films.

Gong et al. reported a novel application of aluminum alkoxide MLD coatings for polydimethylsiloxane (PDMS) surface modification to increase its wetting properties and stability [115]. PDMS is an important polymer material widely used for microfluidic device and lithography [116, 117]. However, the hydrophobic nature of PDMS severely limits its application in aqueous solutions. Alter 100 cycles of MLD deposition, the hydrophilicity of PDMS substrate was greatly enhanced, with the water contact angle decreased from ~116 to 40°, and the contact angle remains stable in air for 14 days.[115] Aluminum alkoxide MLD coatings were prepared using TMA and glycidol.

Qin et al. reported a method to form small size and good dispersion Cu oxide nanoparticles by annealing the hybrid MLD coating encapsulated metal nanoparticles in air [118]. The MLD hybrid coating was prepared by using TMA and EG; after organic components removal, the hybrid MLD coating was converted to porous Al_2O_3 coating. The

channels of porous Al_2O_3 coating led to the fragmentation of Cu nanoparticles, and facilitated copper outward diffusion and inhibited oxygen inward diffusion due to the smaller size of Cu atom.

Liang et al. used the MLD thin coating to prepare thermally-stable, highly-dispersed metal nanoparticle catalysts [119]. Supported noble metal catalysts deactivate at high temperature when these metal particles sinter to from larger particles [120]. Porous Al_2O_3 coating was prepared by using TMA and EG followed by calcination in air at 400 ºC. The thermal stability of metal particles was studied by holding the catalysts at elevated temperature for 4 h. A catalyst with 40 cycles of MLD coating showed greatly improved thermal-stability compared with original uncoated catalysts after calcination in air even at 800 ºC.

Sheng et al. reported a metal core with porous MLD coating shell to be used as a size-selective catalyst [121]. Alucone MLD coating was deposited using TMA and EG. Porous Al_2O_3 coating was then formed by oxidation in air at 400 ºC. The size selective effect was demonstrated by catalytic hydrogenation of olefins (n-hexene, and cis-cyclooctene). For uncoated catalyst, the conversion of n-hexene and cis-cyclooctene was 9.1% and 6.9%, respectively. With ~4 nm thick of Al_2O_3 coatings, no obvious cis-cyclooctene conversion (<0.02%) was observed. In contrast, conversion of n-hexene only decreased to 4.5%. It is believed that the porous Al_2O_3 coatings allows smaller reactants, n-hexene, to access the encapsulated active sites, and excludes the reactants with larger molecular size.

Ishchuk et al. deposited titanium alkoxide using $TiCl_4$ and EG as precursors for highly active photocatalytic films [122]. The photocatalytic performance was examined by porphyrin decomposition. The best photocatalytic performance was obtained when the titanium alkoxide MLD annealed at 650 ºC by producing an intermediate state of crystalline regions embedded in an amorphous film.

Yu et al. deposited a 10-nm thick alucone MLD coating using TMA and EG as precursors on synthesized SAPO-34 zeolite membranes, to evaluate the potential of using microporous MLD coating to reduce SAPO-34 zeolite pores [123]. After the organic component was removed by oxidation, the resulting ultra-thin microporous layers increased the H_2/N_2 selectivity of the SAPO-34 membranes; the highest selectivity was 1040, in strong contrast with the selectivity of 8 for SAPO-34 membranes without coating. The H_2/CO_2 selectivity also increased significantly from ~1.3 to 23.2.

1.5 THESIS SCOPE

The main objective of this thesis is to study the ultra-thin porous metal oxide coatings prepared by molecular layer deposition (MLD) technique, to characterize the microstructure of MLD coatings, and to utilize their structural properties for adsorptive separation, water purification and gas storage. Chapter 2 introduces a new concept, pore misalignment, to continuously adjust the effective pore size of 5A zeolite for small organic molecules separations by controlling the Al_2O_3 MLD coating thickness. In chapter 3, a composite zeolite adsorbent was prepared by depositing TiO_2 MLD coating on the external surface of 5A zeolite for CO_2/CH_4, CO_2/N_2 and C_3H_6/C_3H_8 separation. Chapter 4 reports the separation performance of MLD coated zeolite composite sorbents can be further improved by controlling the calcination processing conditions for high efficient CO_2

capture. In chapter 5, MLD was used as a highly controllable method to prepare TiO_2 nanofiltration membranes for water purification. Chapter 6 demonstrates a novel concept of utilizing nanoporous coatings prepared by hydrothermal method and MLD modification as effective nano-valves on microporous adsorbents for high capacity natural gas storage at low storage pressure. Chapter 7 summarizes conclusions.

1.6 REFERENCES

[1] J.L. Humphrey, Separation processes: Playing a critical role, Journal Name: Chemical Engineering Progress; Journal Volume: 91; Journal Issue: 10; Other Information: PBD: Oct 1995 (1995) Medium: X; Size: pp. 31-41.

[2] B. Van de Voorde, B. Bueken, J. Denayer, D. De Vos, Adsorptive separation on metal-organic frameworks in the liquid phase, Chem. Soc. Rev. 43 (2014) 5766-5788.

[3] X. Xu, X. Zhao, L. Sun, X. Liu, Adsorption separation of carbon dioxide, methane and nitrogen on monoethanol amine modified β-zeolite, Journal of Natural Gas Chemistry 18 (2009) 167-172.

[4] X. Xu, X. Zhao, L. Sun, X. Liu, Adsorption separation of carbon dioxide, methane, and nitrogen on Hβ and Na-exchanged β-zeolite, Journal of Natural Gas Chemistry 17 (2008) 391-396.

[5] C.Y. Lee, Y.-S. Bae, N.C. Jeong, O.K. Farha, A.A. Sarjeant, C.L. Stern, P. Nickias, R.Q. Snurr, J.T. Hupp, S.T. Nguyen, Kinetic Separation of Propene and Propane in Metal−Organic Frameworks: Controlling Diffusion Rates in Plate-Shaped Crystals via Tuning of Pore Apertures and Crystallite Aspect Ratios, J. Am. Chem. Soc. 133 (2011) 5228-5231.

[6] K. Morishige, Adsorption and Separation of CO2/CH4 on Amorphous Silica Molecular Sieve, The Journal of Physical Chemistry C 115 (2011) 9713-9718.

[7] K. Li, D.H. Olson, J. Seidel, T.J. Emge, H. Gong, H. Zeng, J. Li, Zeolitic Imidazolate Frameworks for Kinetic Separation of Propane and Propene, J. Am. Chem. Soc. 131 (2009) 10368-10369.

[8] D.M. Ruthven, S.C. Reyes, Adsorptive separation of light olefins from paraffins, Microporous Mesoporous Mat. 104 (2007) 59-66.

[9] H. Jasuja, J. Zang, D.S. Sholl, K.S. Walton, Rational Tuning of Water Vapor and CO2 Adsorption in Highly Stable Zr-Based MOFs, The Journal of Physical Chemistry C 116 (2012) 23526-23532.

[10] C.A. Grande, Advances in Pressure Swing Adsorption for Gas Separation, ISRN Chemical Engineering 2012 (2012) 13.

[11] S. Aguado, G. Bergeret, C. Daniel, D. Farrusseng, Absolute Molecular Sieve Separation of Ethylene/Ethane Mixtures with Silver Zeolite A, J. Am. Chem. Soc. 134 (2012) 14635-14637.

[12] A. Van Miltenburg, W. Zhu, F. Kapteijn, J.A. Moulijn, Adsorptive Separation of Light Olefin/Paraffin Mixtures, Chemical Engineering Research and Design 84 (2006) 350-354.

[13] A. Miltenburg, J. Gascon, W. Zhu, F. Kapteijn, J.A. Moulijn, Propylene/propane mixture adsorption on faujasite sorbents, Adsorption 14 (2008) 309-321.
[14] S.U. Rege, J. Padin, R.T. Yang, Olefin/paraffin separations by adsorption: π-Complexation vs. kinetic separation, Aiche J. 44 (1998) 799-809.
[15] Y. Lee, B.A. Reisner, J.C. Hanson, G.A. Jones, J.B. Parise, D.R. Corbin, B.H. Toby, A. Freitag, J.Z. Larese, New Insight into Cation Relocations within the Pores of Zeolite Rho: In Situ Synchrotron X-Ray and Neutron Powder Diffraction Studies of Pb- and Cd-Exchanged Rho, The Journal of Physical Chemistry B 105 (2001) 7188-7199.
[16] C.D. Chudasama, J. Sebastian, R.V. Jasra, Pore-Size Engineering of Zeolite A for the Size/Shape Selective Molecular Separation, Ind. Eng. Chem. Res. 44 (2005) 1780-1786.
[17] W. Lu, D. Yuan, D. Zhao, C.I. Schilling, O. Plietzsch, T. Muller, S. Bräse, J. Guenther, J. Blümel, R. Krishna, Z. Li, H.-C. Zhou, Porous Polymer Networks: Synthesis, Porosity, and Applications in Gas Storage/Separation, Chem. Mat. 22 (2010) 5964-5972.
[18] C. Moreno-Castilla, Adsorption of organic molecules from aqueous solutions on carbon materials, Carbon 42 (2004) 83-94.
[19] A.T. Nasrabadi, M. Foroutan, Air adsorption and separation on carbon nanotube bundles from molecular dynamics simulations, Computational Materials Science 61 (2012) 134-139.
[20] E.C.d. Oliveira, C.T.G.V.M.T. Pires, H.O. Pastore, Why are carbon molecular sieves interesting?, Journal of the Brazilian Chemical Society 17 (2006) 16-29.
[21] G.-M. Nam, B.-M. Jeong, S.-H. Kang, B.-K. Lee, D.-K. Choi, Equilibrium Isotherms of CH4, C2H6, C2H4, N2, and H2 on Zeolite 5A Using a Static Volumetric Method, Journal of Chemical & Engineering Data 50 (2005) 72-76.
[22] Y. Li, H. Yi, X. Tang, F. Li, Q. Yuan, Adsorption separation of CO2/CH4 gas mixture on the commercial zeolites at atmospheric pressure, Chem. Eng. J. 229 (2013) 50-56.
[23] C.A. Grande, A.E. Rodrigues, Adsorption Kinetics of Propane and Propylene in Zeolite 4A, Chemical Engineering Research and Design 82 (2004) 1604-1612.
[24] Y. Ren, Z. Ma, P.G. Bruce, Ordered mesoporous metal oxides: synthesis and applications, Chem. Soc. Rev. 41 (2012) 4909-4927.
[25] D.M. Ruthven, Zeolites as selective adsorbents, Chem. Eng. Prog. 84 (1988) 42-50.
[26] K.D. Hammonds, V. Heine, M.T. Dove, Rigid-unit modes and the quantitative determination of the flexibility possessed by zeolite frameworks, J. Phys. Chem. B 102 (1998) 1759-1767.
[27] H. Peng, S.M. Liu, L. Ma, Z.J. Lin, S.J. Wang, Growing process of CdS nanoclusters in zeolite Y studied by positron annihilation, Journal of Crystal Growth 224 (2001) 274-279.
[28] J.A. Kaduk, J. Faber, Crystal structure of zeolite Y as a function of ion exchange, Rigaku J 12 (1995) 14-34.
[29] V.A. Tuan, J.L. Falconer, R.D. Noble, Isomorphous substitution of Al, Fe, B, and Ge into MFI-zeolite membranes, Microporous Mesoporous Mat. 41 (2000) 269-280.
[30] M.T. Weller, Where zeolites and oxides merge: semi-condensed tetrahedral frameworks, Journal of the Chemical Society, Dalton Transactions (2000) 4227-4240.
[31] D.W. Breck, W.G. Eversole, R.M. Milton, T.B. Reed, T.L. Thomas, Crystalline zeolites. 1. The properties of a new synthetic zeolite, type-A, J. Am. Chem. Soc. 78 (1956) 5963-5971.

[32] D.W. Breck, W.G. Eversole, R.M. Milton, T.B. Reed, T.L. Thomas, CRYSTALLINE ZEOLITES .1. THE PROPERTIES OF A NEW SYNTHETIC ZEOLITE, TYPE-A, J. Am. Chem. Soc. 78 (1956) 5963-5971.
[33] J. Lindmark, J. Hedlund, S.K. Wirawan, D. Creaser, M. Li, D. Zhang, X. Zou, Impregnation of zeolite membranes for enhanced selectivity, J. Membr. Sci. 365 (2010) 188-197.
[34] Z. Song, Y. Huang, L. Wang, S. Li, M. Yu, Composite 5A zeolite with ultrathin porous TiO 2 coating for selective gas adsorption, Chem. Commun. 51 (2015) 373-375.
[35] L. Huang, X. Yang, D. Cao, From Inorganic to Organic Strategy To Design Porous Aromatic Frameworks for High-Capacity Gas Storage, The Journal of Physical Chemistry C 119 (2015) 3260-3267.
[36] Z.N. Song, Y. Huang, W.W. Xu, L. Wang, Y. Bao, S.G. Li, M. Yu, Continuously Adjustable, Molecular-Sieving "Gate" on 5A Zeolite for Distinguishing Small Organic Molecules by Size, Sci. Rep. 5, 13981 (2015).
[37] S. Sato, Y. Yu-u, H. Yahiro, N. Mizuno, M. Iwamoto, Cu-ZSM-5 zeolite as highly active catalyst for removal of nitrogen monoxide from emission of diesel engines, Applied Catalysis 70 (1991) L1-L5.
[38] F. Dougnier, J. Patarin, J.L. Guth, D. Anglerot, Synthesis, characterization, and catalytic properties of silica-rich faujasite-type zeolite (FAU) and its hexagonal analog (EMT) prepared by using crown-ethers as templates, Zeolites 12 (1992) 160-166.
[39] E. Kim, T. Lee, H. Kim, W.-J. Jung, D.-Y. Han, H. Baik, N. Choi, J. Choi, Chemical Vapor Deposition on Chabazite (CHA) Zeolite Membranes for Effective Post-Combustion CO2 Capture, Environ. Sci. Technol. 48 (2014) 14828-14836.
[40] S.V. Sivakumar, D.P. Rao, Modified Duplex PSA. 1. Sharp Separation and Process Intensification for CO2−N2−13X Zeolite System, Ind. Eng. Chem. Res. 50 (2011) 3426-3436.
[41] J. Merel, M. Clausse, F. Meunier, Experimental Investigation on CO2 Post−Combustion Capture by Indirect Thermal Swing Adsorption Using 13X and 5A Zeolites, Ind. Eng. Chem. Res. 47 (2008) 209-215.
[42] Y. Huang, L. Wang, Z. Song, S. Li, M. Yu, Growth of High-Quality, Thickness-Reduced Zeolite Membranes towards N2/CH4 Separation Using High-Aspect-Ratio Seeds, Angewandte Chemie 127 (2015) 10993-10997.
[43] C. Covarrubias, R. Arriagada, J. Yanez, R. García, M. Angélica, S. Barros, P. Arroyo, E.F. Sousa-Aguiar, Removal of chromium (III) from tannery effluents, using a system of packed columns of zeolite and activated carbon, Journal of Chemical Technology and Biotechnology 80 (2005) 899-908.
[44] B.F. Mentzen, P. Gelin, The silicate p-xylene system. 1. Flexibility of the MFI framework and sorption mechanism observed during p-xylene pore-filling by x-ray-powder diffraction at room-temperature, Mater. Res. Bull. 30 (1995) 373-380.
[45] T.M. Nenoff, J.B. Parise, G.A. Jones, L.G. Galya, D.R. Corbin, G.D. Stucky, Flexibility of the zeolite RHO framework. In situ X-ray and neutron powder structural characterization of cation-exchanged BePO and BeAsO RHO analogs, J. Phys. Chem. 100 (1996) 14256-14264.
[46] G.M. Johnson, B.A. Reisner, A. Tripathi, D.R. Corbin, B.H. Toby, J.B. Parise, Flexibility and cation distribution upon lithium exchange of aluminosilicate and aluminogermanate materials with the RHO topology, Chem. Mat. 11 (1999) 2780-2787.

[47] S.M. Kuznicki, V.A. Bell, S. Nair, H.W. Hillhouse, R.M. Jacubinas, C.M. Braunbarth, B.H. Toby, M. Tsapatsis, A titanosilicate molecular sieve with adjustable pores for size-selective adsorption of molecules, Nature 412 (2001) 720-724.
[48] A. Anson, C.C.H. Lin, T.M. Kuznicki, S.M. Kuznicki, Separation of ethylene/ethane mixtures by adsorption on small-pored titanosilicate molecular sieves, Chem. Eng. Sci. 65 (2010) 807-811.
[49] M. Shi, A.M. Avila, F. Yang, T.M. Kuznicki, S.M. Kuznicki, High pressure adsorptive separation of ethylene and ethane on Na-ETS-10, Chem. Eng. Sci. 66 (2011) 2817-2822.
[50] S. Pakseresht, M. Kazemeini, M.M. Akbarnejad, Equilibrium isotherms for CO, CO2, CH4 and C2H4 on the 5A molecular sieve by a simple volumetric apparatus, Sep. Purif. Technol. 28 (2002) 53-60.
[51] S. Gumma, O. Talu, Gibbs dividing surface and helium adsorption, Adsorption 9 (2003) 17-28.
[52] J.A. Dunne, R. Mariwala, M. Rao, S. Sircar, R.J. Gorte, A.L. Myers, Calorimetric Heats of Adsorption and Adsorption Isotherms. 1. O2, N2, Ar, CO2, CH4, C2H6, and SF6 on Silicalite, Langmuir 12 (1996) 5888-5895.
[53] X. Feng, C.Y. Pan, J. Ivory, D. Ghosh, Integrated membrane/adsorption process for gas separation, Chem. Eng. Sci. 53 (1998) 1689-1698.
[54] A.D. Ebner, J.A. Ritter, State-of-the-art adsorption and membrane separation processes for carbon dioxide production from carbon dioxide emitting industries, Sep. Sci. Technol. 44 (2009) 1273-1421.
[55] J.G. Bitter, Transport mechanisms in membrane separation processes, Springer Science & Business Media, 2012.
[56] W.W. Ho, K.K. Sirkar, Membrane handbook, Springer Science & Business Media, 1992.
[57] B.D. Freeman, Basis of Permeability/Selectivity Tradeoff Relations in Polymeric Gas Separation Membranes, Macromolecules 32 (1999) 375-380.
[58] M.A. Aroon, A.F. Ismail, T. Matsuura, M.M. Montazer-Rahmati, Performance studies of mixed matrix membranes for gas separation: A review, Sep. Purif. Technol. 75 (2010) 229-242.
[59] T.-S. Chung, L.Y. Jiang, Y. Li, S. Kulprathipanja, Mixed matrix membranes (MMMs) comprising organic polymers with dispersed inorganic fillers for gas separation, Progress in Polymer Science 32 (2007) 483-507.
[60] D.F. Sanders, Z.P. Smith, R. Guo, L.M. Robeson, J.E. McGrath, D.R. Paul, B.D. Freeman, Energy-efficient polymeric gas separation membranes for a sustainable future: A review, Polymer 54 (2013) 4729-4761.
[61] C. Staudt-Bickel, W.J. Koros, Olefin/paraffin gas separations with 6FDA-based polyimide membranes, J. Membr. Sci. 170 (2000) 205-214.
[62] P. Marchetti, M.F. Jimenez Solomon, G. Szekely, A.G. Livingston, Molecular Separation with Organic Solvent Nanofiltration: A Critical Review, Chem. Rev. 114 (2014) 10735-10806.
[63] L.V. Saboyainsta, J.-L. Maubois, Current developments of microfiltration technology in the dairy industry, Le Lait 80 (2000) 541-553.
[64] W. Gao, H. Liang, J. Ma, M. Han, Z.-l. Chen, Z.-s. Han, G.-b. Li, Membrane fouling control in ultrafiltration technology for drinking water production: A review, Desalination 272 (2011) 1-8.

[65] A.L. Zydney, Chapter 15 - High Performance Ultrafiltration Membranes: Pore Geometry and Charge Effects, in: S.T. Oyama, M.S.-W. Susan (Eds.) Membrane Science and Technology, Elsevier, 2011, pp. 333-352.
[66] G. Vatai, Nanofiltration application in food technology and environmental protection, in: Integration of Membrane Processes into Bioconversions, Springer, 2000, pp. 155-163.
[67] K. Khulbe, C. Feng, T. Matsuura, Pore size, pore size distribution, and roughness at the membrane surface, Synthetic Polymeric Membranes: Characterization by Atomic Force Microscopy (2008) 101-139.
[68] Y. Han, Z. Xu, C. Gao, Ultrathin Graphene Nanofiltration Membrane for Water Purification, Adv. Funct. Mater. 23 (2013) 3693-3700.
[69] N. Hilal, H. Al-Zoubi, N.A. Darwish, A.W. Mohammad, M. Abu Arabi, A comprehensive review of nanofiltration membranes: Treatment, pretreatment, modelling, and atomic force microscopy, Desalination 170 (2004) 281-308.
[70] A.W. Mohammad, Y.H. Teow, W.L. Ang, Y.T. Chung, D.L. Oatley-Radcliffe, N. Hilal, Nanofiltration membranes review: Recent advances and future prospects, Desalination 356 (2015) 226-254.
[71] D.A.L. Mahmut Selim Ersan , and Tanju Karanfil N-Nitrosodimethylamine (NDMA) Precursors Leach from Nanofiltration Membranes, Environ. Sci. Technol. Lett. 2 (2015) 66-69.
[72] L.P. Raman, M. Cheryna, N. Rajagopalan, Consider nanofiltration for membrane separations, Chemical Engineering Progress;(United States) 90 (1994).
[73] T. Van Gestel, H. Kruidhof, D.H.A. Blank, H.J.M. Bouwmeester, ZrO2 and TiO2 membranes for nanofiltration and pervaporation - Part 1. Preparation and characterization of a corrosion-resistant ZrO2 nanofiltration membrane with a MWCO < 300, J. Membr. Sci. 284 (2006) 128-136.
[74] B. Van der Bruggen, Chemical Modification of Polyethersulfone Nanofiltration Membranes: A Review, J. Appl. Polym. Sci. 114 (2009) 630-642.
[75] T. Fujioka, S.J. Khan, J.A. McDonald, L.D. Nghiem, Nanofiltration of trace organic chemicals: A comparison between ceramic and polymeric membranes, Sep. Purif. Technol. 136 (2014) 258-264.
[76] B. Van der Bruggen, C. Vandecasteele, T. Van Gestel, W. Doyen, R. Leysen, A review of pressure-driven membrane processes in wastewater treatment and drinking water production, Environmental progress 22 (2003) 46-56.
[77] J. Sekulic, J.E. ten Elshof, D.H.A. Blank, A microporous titania membrane for nanofiltration and pervaporation, Adv. Mater. 16 (2004) 1546-1500.
[78] P. Puhlfurss, A. Voigt, R. Weber, M. Morbe, Microporous TiO2 membranes with a cut off < 500 Da, J. Membr. Sci. 174 (2000) 123-133.
[79] S. Benfer, U. Popp, H. Richter, C. Siewert, G. Tomandl, Development and characterization of ceramic nanofiltration membranes, Sep. Purif. Technol. 22-3 (2001) 231-237.
[80] P. Marchetti, M.F.J. Solomon, G. Szekely, A.G. Livingston, Molecular Separation with Organic Solvent Nanofiltration: A Critical Review, Chem. Rev. 114 (2014) 10735-10806.
[81] Q. Xu, M.A. Anderson, Sol–Gel Route to Synthesis of Microporous Ceramic Membranes: Preparation and Characterization of Microporous TiO2 and ZrO2 Xerogels, J. Am. Ceram. Soc. 77 (1994) 1939-1945.

[82] R.A. Peterson, M.A. Anderson, C.G. Hill Jr, Development of TiO2 membranes for gas phase nanofiltration, J. Membr. Sci. 94 (1994) 103-109.
[83] T. Van Gestel, C. Vandecasteele, A. Buekenhoudt, C. Dotremont, J. Luyten, R. Leysen, B. Van der Bruggen, G. Maes, Salt retention in nanofiltration with multilayer ceramic TiO2 membranes, J. Membr. Sci. 209 (2002) 379-389.
[84] D.A. Gómez-Gualdrón, C.E. Wilmer, O.K. Farha, J.T. Hupp, R.Q. Snurr, Exploring the limits of methane storage and delivery in nanoporous materials, The Journal of Physical Chemistry C 118 (2014) 6941-6951.
[85] L.D. Tran, J.I. Feldblyum, A.G. Wong-Foy, A.J. Matzger, Filling Pore Space in a Microporous Coordination Polymer to Improve Methane Storage Performance, Langmuir 31 (2015) 2211-2217.
[86] B. Li, H.-M. Wen, H. Wang, H. Wu, M. Tyagi, T. Yildirim, W. Zhou, B. Chen, A porous metal–organic framework with dynamic pyrimidine groups exhibiting record high methane storage working capacity, J. Am. Chem. Soc. 136 (2014) 6207-6210.
[87] V.C. Menon, S. Komarneni, Porous Adsorbents for Vehicular Natural Gas Storage: A Review, Journal of Porous Materials 5 (1998) 43-58.
[88] Y. Peng, V. Krungleviciute, I. Eryazici, J.T. Hupp, O.K. Farha, T. Yildirim, Methane Storage in Metal–Organic Frameworks: Current Records, Surprise Findings, and Challenges, J. Am. Chem. Soc. 135 (2013) 11887-11894.
[89] T. Suntola, US Patent 4058430 (1977).
[90] H. Kim, H.B.R. Lee, W.J. Maeng, Applications of atomic layer deposition to nanofabrication and emerging nanodevices, Thin Solid Films 517 (2009) 2563-2580.
[91] M. Leskela, M. Ritala, Atomic layer deposition chemistry: Recent developments and future challenges, Angew. Chem.-Int. Edit. 42 (2003) 5548-5554.
[92] P. Ardalan, C. Musgrave, S.F. Bent, Effects of Surface Functionalization on Titanium Dioxide Atomic Layer Deposition on Ge Surfaces, ECS Transactions 25 (2009) 131-139.
[93] L. Chen, H. Chung, S.M. Seutter, X. Yang, X. Ming, V. Ku, D.-y. Wu, A. Ouye, N. Nakashima, B. Chin, Integration of ALD tantalum nitride and alpha-phase tantalum for copper metallization application, in, US Patent 20,030,124,262, 2003.
[94] J.R. Bakke, J.S. King, H.J. Jung, R. Sinclair, S.F. Bent, Atomic layer deposition of ZnS via in situ production of H2S, Thin Solid Films 518 (2010) 5400-5408.
[95] T. Aaltonen, M. Ritala, T. Sajavaara, J. Keinonen, M. Leskelä, Atomic Layer Deposition of Platinum Thin Films, Chem. Mat. 15 (2003) 1924-1928.
[96] M. Ritala, Handbook of Thin Film Materials, 2001.
[97] N.M. Adarnczyk, A.A. Dameron, S.M. George, Molecular layer deposition of poly(p-phenylene terephthalamide) films using terephthaloyl chloride and p-phenylenediamine, Langmuir 24 (2008) 2081-2089.
[98] X. Liang, D.M. King, P. Li, S.M. George, A.W. Weimer, Nanocoating Hybrid Polymer Films on Large Quantities of Cohesive Nanoparticles by Molecular Layer Deposition, Aiche J. 55 (2009) 1030-1039.
[99] T. Yoshimura, S. Tatsuura, W. Sotoyama, POLYMER-FILMS FORMED WITH MONOLAYER GROWTH STEPS BY MOLECULAR LAYER DEPOSITION, Appl. Phys. Lett. 59 (1991) 482-484.
[100] X. Liang, A.W. Weimer, An overview of highly porous oxide films with tunable thickness prepared by molecular layer deposition, Current Opinion in Solid State and Materials Science 19 (2015) 115-125.

[101] A.A. Dameron, D. Seghete, B.B. Burton, S.D. Davidson, A.S. Cavanagh, J.A. Bertrand, S.M. George, Molecular layer deposition of alucone polymer films using trimethylaluminum and ethylene glycol, Chem. Mat. 20 (2008) 3315-3326.
[102] X.H. Liang, M. Yu, J.H. Li, Y.B. Jiang, A.W. Weimer, Ultra-thin microporous-mesoporous metal oxide films prepared by molecular layer deposition (MLD), Chem. Commun. (2009) 7140-7142.
[103] Z.N. Song, Y. Huang, L. Wang, S.G. Li, M. Yu, Composite 5A zeolite with ultrathin porous TiO2 coating for selective gas adsorption, Chem. Commun. 51 (2015) 373-375.
[104] D. Seghete, B.D. Davidson, R.A. Hall, Y.J. Chang, V.M. Bright, S.M. George, Sacrificial layers for air gaps in NEMS using alucone molecular layer deposition, Sensors and Actuators A: Physical 155 (2009) 8-15.
[105] H. Zhou, S.F. Bent, Fabrication of organic interfacial layers by molecular layer deposition: Present status and future opportunities, J. Vac. Sci. Technol. A 31 (2013) 18.
[106] P. Sundberg, M. Karppinen, Organic and inorganic–organic thin film structures by molecular layer deposition: A review, Beilstein J. Nanotechnol. 5 (2014) 1104-1136.
[107] A.S. da Silva Sobrinho, G. Czeremuszkin, M. Latrèche, G. Dennler, M.R. Wertheimer, A study of defects in ultra-thin transparent coatings on polymers, Surface and Coatings Technology 116–119 (1999) 1204-1210.
[108] A. da Silva Sobrinho, G. Czeremuszkin, M. Latreche, M. Wertheimer, Defect-permeation correlation for ultrathin transparent barrier coatings on polymers, J. Vac. Sci. Technol. A 18 (2000) 149-157.
[109] A. Roberts, B. Henry, A. Sutton, C. Grovenor, G. Briggs, T. Miyamoto, M. Kano, Y. Tsukahara, M. Yanaka, Gas permeation in silicon-oxide/polymer (SiO x/PET) barrier films: role of the oxide lattice, nano-defects and macro-defects, J. Membr. Sci. 208 (2002) 75-88.
[110] A.I. Abdulagatov, R.A. Hall, J.L. Sutherland, B.H. Lee, A.S. Cavanagh, S.M. George, Molecular Layer Deposition of Titanicone Films using TiCl4 and Ethylene Glycol or Glycerol: Growth and Properties, Chem. Mat. 24 (2012) 2854-2863.
[111] H. Zhou, S.F. Bent, Highly Stable Ultrathin Carbosiloxane Films by Molecular Layer Deposition, The Journal of Physical Chemistry C 117 (2013) 19967-19973.
[112] A. Sood, P. Sundberg, J. Malm, M. Karppinen, Layer-by-layer deposition of Ti–4,4′-oxydianiline hybrid thin films, Applied Surface Science 257 (2011) 6435-6439.
[113] J.W. DuMont, S.M. George, Pyrolysis of Alucone Molecular Layer Deposition Films Studied Using In Situ Transmission Fourier Transform Infrared Spectroscopy, The Journal of Physical Chemistry C 119 (2015) 14603-14612.
[114] R.L. Patel, Y.-B. Jiang, X. Liang, Highly Porous Titania Films Coated on Sub-micron Particles with Tunable Thickness by Molecular Layer Deposition in a Fluidized Bed Reactor, Ceramics International 41 (2014) 2240-2246.
[115] B. Gong, J.C. Spagnola, G.N. Parsons, Hydrophilic mechanical buffer layers and stable hydrophilic finishes on polydimethylsiloxane using combined sequential vapor infiltration and atomic/molecular layer deposition, J. Vac. Sci. Technol. A 30 (2012) 01A156.
[116] E. Delamarche, A. Bernard, H. Schmid, B. Michel, H. Biebuyck, Patterned delivery of immunoglobulins to surfaces using microfluidic networks, Science 276 (1997) 779-781.
[117] J.C. McDonald, G.M. Whitesides, Poly(dimethylsiloxane) as a Material for Fabricating Microfluidic Devices, Accounts of Chemical Research 35 (2002) 491-499.

[118] Y. Qin, Y. Yang, R. Scholz, E. Pippel, X. Lu, M. Knez, Unexpected Oxidation Behavior of Cu Nanoparticles Embedded in Porous Alumina Films Produced by Molecular Layer Deposition, Nano Letters 11 (2011) 2503-2509.
[119] X. Liang, J. Li, M. Yu, C.N. McMurray, J.L. Falconer, A.W. Weimer, Stabilization of Supported Metal Nanoparticles Using an Ultrathin Porous Shell, ACS Catal. 1 (2011) 1162-1165.
[120] R.M.J. Fiedorow, B.S. Chahar, S.E. Wanke, The sintering of supported metal catalysts: II. Comparison of sintering rates of supported Pt, Ir, and Rh catalysts in hydrogen and oxygen, J. Catal. 51 (1978) 193-202.
[121] Z. Shang, R.L. Patel, B.W. Evanko, X. Liang, Encapsulation of supported metal nanoparticles with an ultra-thin porous shell for size-selective reactions, Chem. Commun. 49 (2013) 10067-10069.
[122] S. Ishchuk, D.H. Taffa, O. Hazut, N. Kaynan, R. Yerushalmi, Transformation of Organic–Inorganic Hybrid Films Obtained by Molecular Layer Deposition to Photocatalytic Layers with Enhanced Activity, ACS Nano 6 (2012) 7263-7269.
[123] M. Yu, H.H. Funke, R.D. Noble, J.L. Falconer, H2 separation using defect-free, inorganic composite membranes, J. Am. Chem. Soc. 133 (2011) 1748-1750.

CHAPTER 2

CONTINUOUSLY ADJUSTABLE, MOLECULAR-SIEVING "GATE" ON 5A ZEOLITE FOR DISTINGUISHING SMALL ORGANIC MOLECULES BY SIZE

2.1 ABSTRACT

Zeolites/molecular sieves with uniform, molecular-sized pores are important for many adsorption-based separation processes. Pore size gaps, however, exist in the current zeolite family. This leads to a great challenge of separating molecules with size differences at ~0.01 nm level. Here, we report a novel concept, pore misalignment, to form a continuously adjustable, molecular-sieving "gate" at the 5A zeolite pore entrance without sacrificing the internal capacity. Misalignment of the micropores of the alumina coating with the 5A zeolite pores was related with and facilely adjusted by the coating thickness. For the first time, organic molecules with sub-0.01 nm size differences were effectively distinguished via appropriate misalignment. This novel concept may have great potential to fill the pore size gaps of the zeolite family and realize size-selective adsorption separation.

2.2 INTRODUCTION

Zeolites/molecular sieves are one of the most promising adsorbents that may help realize true molecular-sieving separation, because of their uniform, molecular-sized pores (0.3~1.3 nm) and high chemical, thermal, and mechanical stabilities [1]. Pore size gaps, however, exist in the current zeolite family, which leads to the difficulty in separating molecules with small size/shape differences, especially at the 0.01 nm level.

Pore size of zeolites/molecular sieves can be adjusted by several techniques, including ion exchange [2], framework control [3-7], and zeolite external surface modification [8-10]. Ion exchanges have been used as an effective way of adjusting the pore sizes of LTA (Linde Type A) zeolites.[2] The framework of some zeolites, such as zeolite rho, may deform substantially upon adsorption of some molecules [3]. A molecular sieve, ETS-4, has been shown to contract gradually through dehydration at elevated temperatures so that its effective pore size can be adjusted at approximately 0.01 nm step.[4] Recently, a novel method, called ADOR (assembly-disassembly-organization-reassembly), is applied to chemically selectively remove germanium from germanosilicate zeolite UTL in a top-down strategy to prepare a series of IPC zeolites with continuously tuneable surface area and micropore volume [5-7]. Pore opening size of mordenite zeolite was reduced at 0.1 nm level by chemical vapor deposition (CVD) of silica coatings on the external surface of zeolites [8]. The CVD modified ZSM-5 zeolite showed increased shape selectivity of xylene isomers, and HZSM-5 zeolite showed enhanced para-selectivity in the methylation of toluene [9, 10]. But, the pore opening reduction mechanism for CVD modified zeolite was not clear [8-10]. Despite a large selection pool of zeolites/molecular sieves and available techniques to adjust their pore sizes, not all desired pore sizes can be

obtained for target separations. This is especially the case for separating molecules that are very close in size. In addition, pore modification and structure changes were always realized by sacrificing adsorption capacity or internal cavity [4, 11-13]. Here, we report, for the first time, a bottom-up approach, precise pore mouth size adjustment for 5A zeolite from 0.5 to 0.46 nm without sacrificing internal cavity by pore misalignment; organic molecules with size differences as small as 0.01 nm were effectively distinguished by appropriate misalignment.

2.3 EXPERIMENT RESULTS AND DISCUSSION

We used molecular layer deposition (MLD) to form a conformal hybrid aluminum alkoxide_(alucone) coating on the 5A zeolite surface (Supplementary Materials). The hybrid alucone coating was subsequently calcined in air to remove the organic compound to generate a porous alumina coating [14]. MLD provides exquisite control of the coating thickness at the sub-nanometer level and thus achieves conformal coating on substrates even with high-aspect-ratio features [15-19]. Figure 2.1a shows a transmission electron microscopy (TEM) image of 5A zeolite with 60 cycles of MLD; after calcination an approximately 20 nm thick coating was deposited on the 5A zeolite surface, corresponding to a nominal porous alumina deposition rate of 0.33 nm/cycle. The weight percentage of 60 cycles of MLD coating on 5A zeolite is estimated to be < 2% by applying the coating density [19] and thickness, 5A zeolite solid density [20], and external surface area of 5A zeolite crystals, estimated from the average particle size and shape (Figure 2.9 in Supplementary Materials). X-ray photoelectron (XP) spectra (Figure 2.1b) shows after 120 cycles of MLD, silicon (2p binding energy at 102.3 eV) in 5A zeolite can hardly be seen due to the shorter excited electron mean free path than MLD coating thickness; the MLD

coatings are composed of alumina (Table 2.1 and Figure 2.10 in Supplementary Materials). X-ray diffraction (XRD) confirmed LTA zeolite structure before and after MLD, and MLD coatings did not change zeolite structure (Figure 2.11 in Supplementary Materials). Brunauer–Emmett–Teller (BET) measurement and N_2 sorption analysis show that 5A zeolites with and without MLD coatings had almost identical surface area (343.5 ± 8.3 m^2/g) (Figure 2.1c), and identical micropore volume (0.20 cm^3/g) (Figure 2.1c), argon sorption analysis further confirms there is no change in micropore volume after MLD coating deposition (Figure 2.12e), suggesting coatings were only on the external surface of 5A zeolite and the internal cavity of the zeolite was maintained. We also measured vapor adsorption isotherm of the MLD precursor, trimethyl aluminum (TMA), and found negligible adsorbed amounts (Figure 2.6 in Supplementary Materials). Therefore, MLD coatings are expected to be only on the external surface of 5A zeolite, instead of inside the zeolite pores. To further confirm the ultrathin MLD coating is on the 5A zeolite surface and has negligible effect on the internal cavity of 5A zeolite, we also measured CH_4 adsorption isotherms on 5A zeolite and 5A zeolite with different cycles of MLD coatings (Figure 2.1d); almost identical CH_4 adsorbed amounts were found, indicating ultrathin MLD coating did not enter zeolite internal pores. These results demonstrate that ultrathin, porous MLD coatings were deposited only on the external surface of 5A zeolite.

We measured vapor adsorption isotherms of organic molecules with different sizes/shapes (critical diameter: ethanol, 0.450 nm; 1-propanol, 0.456 nm; 1-butanol, 0.463 nm; acetone, 0.479 nm; and 2-propanol, 0.490 nm (Figure 2.5 in Supplementary Materials)) to explore the effective pore sizes (Figure 2.8 in Supplementary Materials). Figure 2.2a shows the sorption capacity of different molecules on 5A zeolite and 5A zeolite with

different cycles of MLD coatings, corresponding to different coating thicknesses. 5A zeolite adsorbs all these molecules because its pore size is larger than them. Also, 5A zeolite shows low ideal adsorption selectivity for these molecules due to the small size differences of these molecules and the similar adsorption strength, with the highest for ethanol over acetone (~4). We found these organic molecules, from the largest molecule

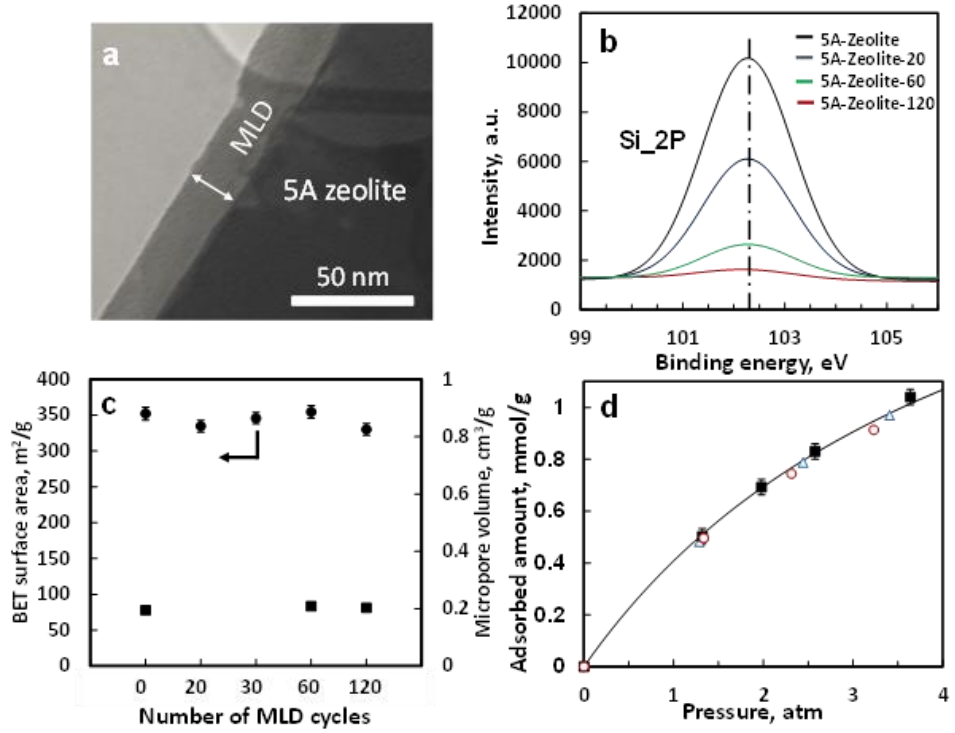

Figure 2.1 Characterization of 5A zeolite and 5A zeolite with molecular layer deposition (MLD) coatings. (a) Transmission electron microscopy (TEM) image of 5A-Zeolite-60. **(b)** X-ray photoelectron spectra (XPS) of Si 2P of 5A zeolite and 5A zeolite with different cycles of MLD coating on 5A zeolite. **(c)** BET surface area of 5A zeolite and 5A zeolite with different cycles of MLD coatings (●), and micropore volume of 5A zeolite and 5A zeolite with different cycles of MLD coatings (■). Error bar is given automatically by Micromeritcs ASAP 2020 unit. **(d)** CH_4 adsorption isotherms at 20℃ on 5A zeolite (■),5A-Zeolite-30 (○), and 5A-Zeolite-60 (Δ). Solid black line is a fit of adsorption points of CH_4 on 5A zeolite by the Langmuir model. All MLD coatings have been calcined in air following the procedure described in the supplementary information.

(2-propanol) to the second smallest molecule (1-propanol), were excluded from the zeolite pores one by one with the increase of MLD cycles, indicating effective pore size decreased

gradually. Figure 2.2b summarizes the pore size change with the coating thickness, and a clear gradual decrease trend of the pore size can be seen. This demonstrates the effective pore size can be precisely controlled at a step change of approximately 0.01 nm by controlling the coating thickness or MLD cycles. In addition, sorption capacity of the smallest molecule, ethanol, decreased only approximately 15% with the increase of MLD cycles up to 60, while rejecting larger molecules. Two most probable mechanisms may result in the observed effective pore size reduction: 1) the decreasing micropore size in the MLD coating with the increase of MLD cycles; 2) the reducing interface pores between the MLD coating and the 5A zeolite pores due to the pore misalignment, as depicted in Figure 2.2c, which slightly and gradually reduces the zeolite pore entrance size or forms a molecular "gate" at the entrance. We propose pore misalignment as the pore reduction mechanism, whereas the first possibility is much less likely based on more evidences discussed in the next paragraphs. In addition, due to the amorphous feature of the MLD coating, we expect the extent of pore misalignment is not exactly the same above all the zeolite pores, and thus a pore entrance size distribution is likely.

We conducted a series of experiments to investigate the pore reduction mechanism, as discussed below. Figure 2.3a shows that after pre-adsorbing 2-propanol, the CH_4 adsorbed amounts on 5A zeolite with 30 cycles of MLD coating (5A-Zeolite-30, abbreviation will be used in the following description) did not change and were essentially the same as those on bare 5A zeolite. However, 5A zeolite, after pre-adsorbing 2-propanol, had negligible CH_4 uptake. Apparently, without the microporous coating 5A zeolite pores have been occupied by 2-propanol, while with 30 cycles of MLD all the zeolite pores are available for CH_4 adsorption. This is consistent with the result in Figure 2.2a, which

shows5A-Zeolite-30 successfully excluded 2-propanol. Although pre-adsorbed 2-propanol had negligible effects on equilibrium CH_4 uptake, it drastically influenced CH_4 uptake

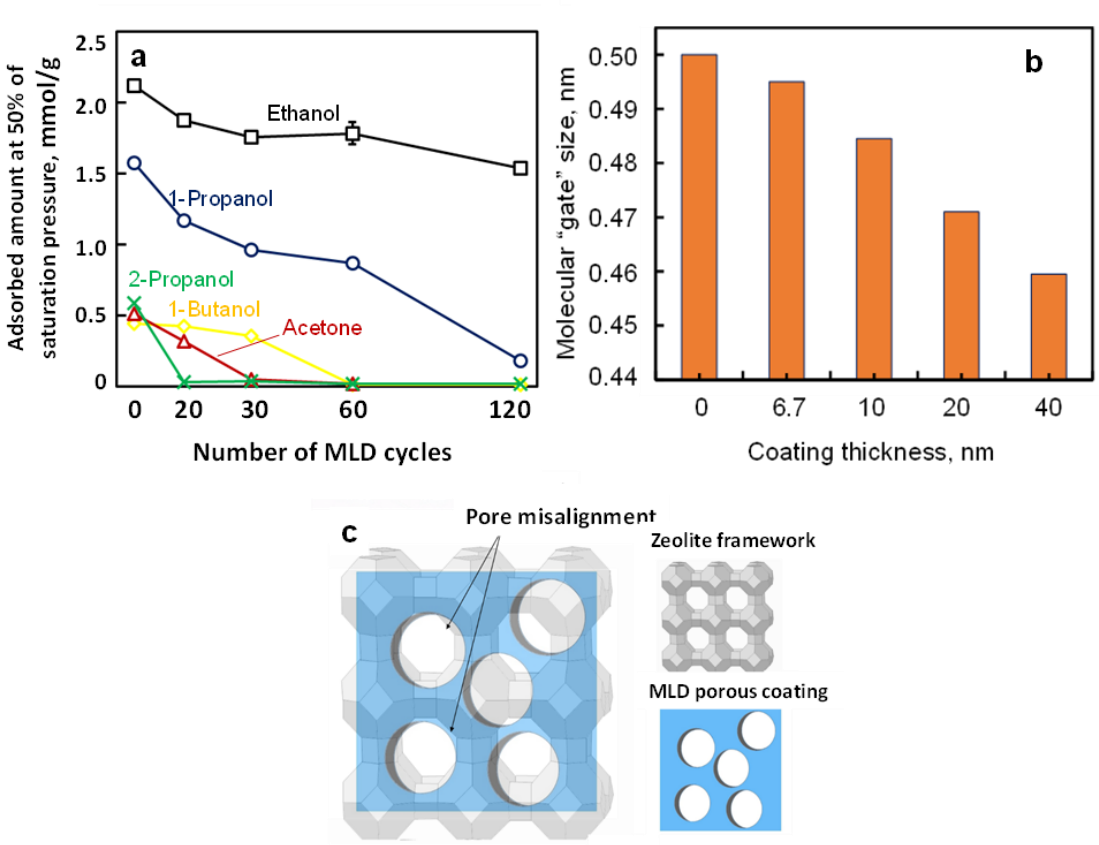

Figure 2.2 Exclusion of organic molecules with different sizes by 5A zeolite and 5A zeolite with MLD coatings. (a) Adsorption capacity of molecules on 5A zeolite and 5A zeolite with different cycles of MLD coating: ethanol (□), 1-propanol (○), 1-butanol (◊), acetone (Δ), and 2-propanol (×); equilibrium pressure is at 50% of the saturation pressure of each component. Error bar shows standard deviation of triplicate measurements. (b) Molecular "gate" sizes with different thickness of microporous alumina coatings; the "gate" size is defined as the average of the smallest excluded molecule and the largest molecule that can be adsorbed; an excluded molecule is defined as a molecule whose adsorbed amount is less than 10% of that in 5A. **(c)** Schematic representation of the proposed pore size reduction mechanism: misalignment of the micropores of the MLD coating with 5A zeolite crystal pores.

kinetics. Figure 2.3b shows that CH_4 uptake rate is almost the same on 5A zeolite and5A-Zeolite-30. This makes sense because the "gate" size (> 0.47 nm) of 5A zeolite with

ultrathin MLD coating is too large to affect the CH_4 (kinetic diameter: 0.38nm [21]) uptake rate. After pre-adsorbing 2-propanol on 5A-Zeolite-30 for 90 minute, CH_4 uptake rate decreased approximately 50 times, as suggested by the diffusivity difference, calculated from the short time update results [22]. Since 2-propanol can't enter zeolite pores of 5A-Zeolite-30, the drastically slowed CH_4 uptake rate must be due to the blocking of MLD coating pores by pre-adsorbed 2-propanol. Therefore, we conclude MLD coating pores must be larger than 2-propanol, but the "gate" size is smaller than 2-propanol so that it can't enter 5A zeolite pores. When a much larger molecule, 2, 2-dimethylbutane (DMB) (kinetic diameter: 0.63 nm [23]), was used to pre-adsorb on5A-Zeolite-30, the CH_4 uptake rate was hardly influenced. Apparently, DMB can't be adsorbed in the MLD coating pores and thus had negligible influence on CH_4 uptake. In these uptake experiments, the equilibrium CH_4 adsorbed amounts (M_∞) for 5A zeolite, 5A-Zeolite-30, and 5A-Zeolite-30after pre-adsorbing 2-propanol and DMB were very close to each other (0.70, 0.68, 0.66 and 0.69 mmol/g, respectively). Therefore, comparison of CH_4 uptake processes is fair. We also measured ethanol adsorption kinetics on 5A zeolite and 5A zeolite with different cycles (30 and 60) of MLD coatings (Figure 2.7). Much slower ethanol uptake rate after MLD coating was observed, but different thickness of MLD coatings had negligible effect on ethanol uptake rate. This again suggests the major transport resistance is not in the MLD coating layer.

To further rule out the possibility that the narrowest pore or transport resistance is at the external surface of the MLD coatings or in the MLD coatings, we crushed samples with 60 cycles of MLD coating (5A-Zeolite-60C) in an attempt to damage the MLD coating. TEM image (Figure 2.14a in Supplementary Materials) showed that after crushing

the MLD coating was partially damaged and showed irregular surface morphology. XP spectra (Figure 2.14b in Supplementary Materials) showed drastically increased amount of

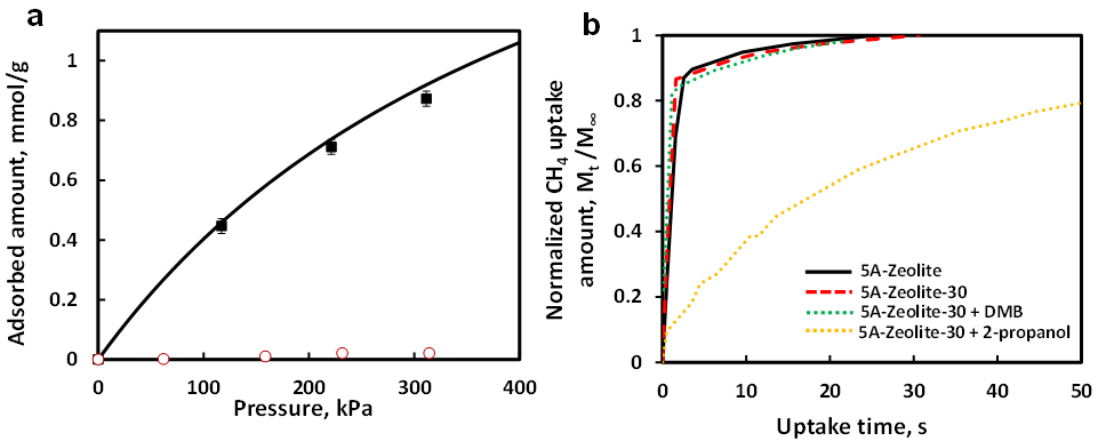

Figure 2.3 Adsorption isotherms and kinetics of CH_4 on 5A zeolite and 5A-Zeolite-30 at 20℃. (a) Adsorption isotherms of CH_4 at 20℃ on 5A zeolite (solid black line), 5A zeolite with pre-adsorbed 2-propanol (○), and 5A-Zeolite-30with pre-adsorbed 2-propanol (■). Error bar shows standard deviation of triplicate measurements. (b) CH_4 adsorption kinetics on 5A zeolite (solid black line), 5A-Zeolite-30(dash red line), 5A-Zeolite-30 pre-adsorbed with 2,2-dimethyl butane (dot green line), and 5A-Zeolite-30 pre-adsorbed with 2-propanol (dot yellow line); M_t is adsorbed amount of CH_4 at time t, and M_∞ is adsorbed amount at equilibrium.

exposed silicon, compared with that without crushing. This again suggests the damage of MLD coating and thus is consistent with the TEM image. However, vapor adsorption isotherms of 2-proponal on 5A-Zeolite-60C was essentially the same as that before crushing (Figure 2.15 in Supplementary Materials). This indicates crushing damaged the MLD coating but did not change the interface between the MLD coating and 5A zeolite. Apparently, the narrowest pores are neither on the external surface of MLD coatings nor in the MLD coatings, but at the interface of the MLD coating and zeolite pores. These adsorption kinetics and equilibrium results strongly support that the narrowest size of MLD coated 5A zeolite must be at the interface between the MLD coating and the 5A zeolite

pores and pore misalignment is the actual mechanism. We speculate the extent of misalignment is related with the thermal stress generated at the interface during calcination. Analytical modelling study [24] has shown that interfacial shear stress due to thermomechnical loading increases with the increase of the adhesive/coating thickness, and thus larger shift/displacement is expected with thicker coatings (also see analysis in Figure 2.16 in Supplementary Materials).

The designable 5A zeolite with desired molecular-sieving "gate" offers a new opportunity for separating small organic molecules based on size differences as small as 0.01 nm. Figure 2.4a shows adsorption isotherms of ethanol and 1-butanol on 5A-Zeolite-60, and an ideal selectivity as high as ~196 has been obtained, in strong contrast with ~ 4 for 5A zeolite, showing its potential for extracting ethanol from 1-butanol, for example, in catalytic conversion of ethanol into 1-butanol [25-29]. In addition, 5A-Zeolite-30 may be used for 1-butanol/acetone separation (Figure 2.4b) in the second important large-scale industrial fermentation, acetone butanol ethanol (ABE) fermentation [30]. 5A-Zeolite-20 may be used for acetone/2-propanol separation (Figure 2.4c) in the hydrogenation of acetone to 2-propanol [31] These examples suggest 5A zeolite can be rationally designed via appropriate pore misalignment by MLD to obtain desired molecular "gate" sizes for size-selective adsorption separation. We also measured 50/50 ethanol/butanol liquid mixture adsorption on 5A zeolite and 5A-Zeolite-60 and found that the adsorbed phase contains ~10% butanol in 5A zeolite but <0.5% in 5A-Zeolite-60, indicating great potential of MLD coated 5A for molecular-sieving separation of liquid mixtures.

2.4 SUPPORTING INFORMATION

2.4.1 MATERIALS AND METHODS

2.4.1.1 MOLECULAR LAYER DEPOSITION ON 5A ZEOLITE

We used 5A zeolite pellets from W.R.Grace & Co.-Conn. Zeolite pellets were firstly outgassed at 200°C for 4 h. The alucone MLD coatings were prepared by using

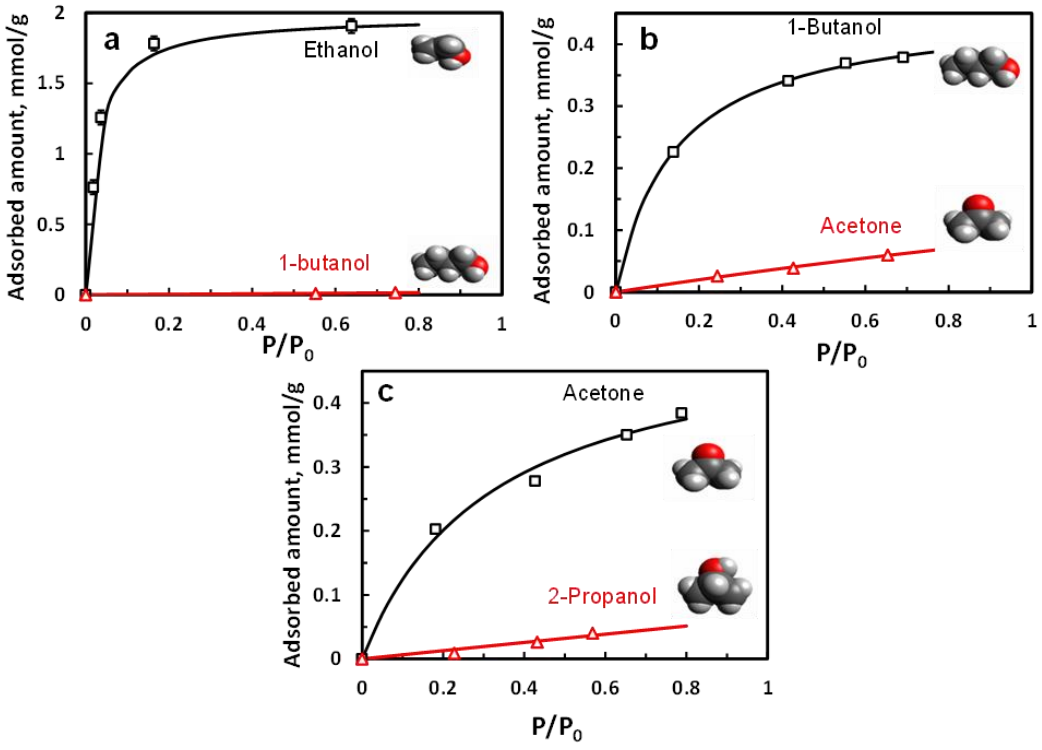

Figure 2.4 Adsorption isotherms of organic molecules at 20°C on 5A zeolite with different cycles of MLD coatings. (a) ethanol and 1-butanol on 5A-Zeolite-60; Error bar shows standard deviation of triplicate measurements. (b) 1-butanol and acetone on 5A-Zeolite-30; (c) acetone and 2-propanol on 5A-Zeolite-20. P is the vapor pressure, and P_0 is the saturation pressure. $P_{0(Ethanol)}$=50 Torr, $P_{0(1\text{-}Butanol)}$=7 Torr, $P_{0(Acetone)}$=201 Torr, $P_{0(2\text{-}Propanol)}$=36 Torr.

trimethyl aluminum (TMA) ($Al(CH_3)_3$; 97%, Sigma Aldrich) and ethylene glycol ($HO(CH_2)_2OH$; 99%, Alfa Aesar) as precursors. Each MLD cycle started with 240 s

vacuum. Ethylene glycol was then introduced into the reactor until a pressure of 50 mTorr and settled for 120 s, and then 240 s vacuum was followed to evacuate extra unreacted ethylene glycol. Ultrahigh purity N_2 (Airgas) was used as the purge gas at 20 sccm for 30 second. Then 240 s vacuum was applied to evacuate N_2. After that, TMA was fed into the reactor until a pressure of 300 mTorr and then settled for 120 s, followed by 240 s vacuum to evacuate extra unreacted TMA. Ultrahigh purity N_2 (Airgas) was again used as the purge gas at 20 sccm for 30 second. Then 240 s vacuum was applied to evacuate N_2. This whole process finishes one MLD cycle. MLD reactions were conducted at 100 °C. Then the coated samples were heated in air from room temperature to 250°C at a rate of 1°C/min, kept at 250°C for 4 h, and then cooled to room temperature at the same rate.

2.4.1.2 ADSORPTION EQUILIBRIUM AND KINETICS MEASUREMENTS

Adsorption isotherms of ethanol (99.5%, Sigma-Aldrich), 1-propanol (99.5%, Alfa Aesar), 1-butanol (99%, Sigma-Aldrich), acetone (99.5%,VWR) and 2-propanol (99%, Sigma-Aldrich) on 5A zeolite and MLD coated 5A zeolite were measured by a volumetric method using a home-built adsorption system. Sorbent (~0.20 g) was firstly outgassed at 200℃ for 2 h. Helium was then used to calibrate the volume of adsorption cell with sorbent at 20℃. Commonly, helium is assumed not to adsorb and used as an inert molecule for volume calibration.[32] After removing residue helium in the adsorption system, interested vapors were introduced at 20℃ to measure the adsorption isotherms. All the vapor adsorption isotherms are shown in Figure 2.5. 5A zeolite adsorbs all the molecules because its pore size is larger than them. But, for MLD coated 5A zeolite, the effective pore sizes gradually decreases with the increase of MLD cycles, and thus rejected molecules one by one starting from the largest 2-propanol. Specifically, 5A-Zeolite-20, 5A-Zeolite-30 and

5A-Zeolite-60 almost completely rejected 2-propanol, acetone, and1-butanol, respectively, while 5A-Zeolite-180 almost excluded 1-propanol. Adsorption isotherm of TMA on 5A zeolite at 20℃ is shown in Figure 2.6. Adsorption kinetics was measured by monitoring vapor pressure change with time. For the pre-adsorption process, we followed the same procedure for organic vapor adsorption, and then introduced CH_4 for its adsorption isotherm measurements and adsorption kinetics measurements with the presence of organic vapor.

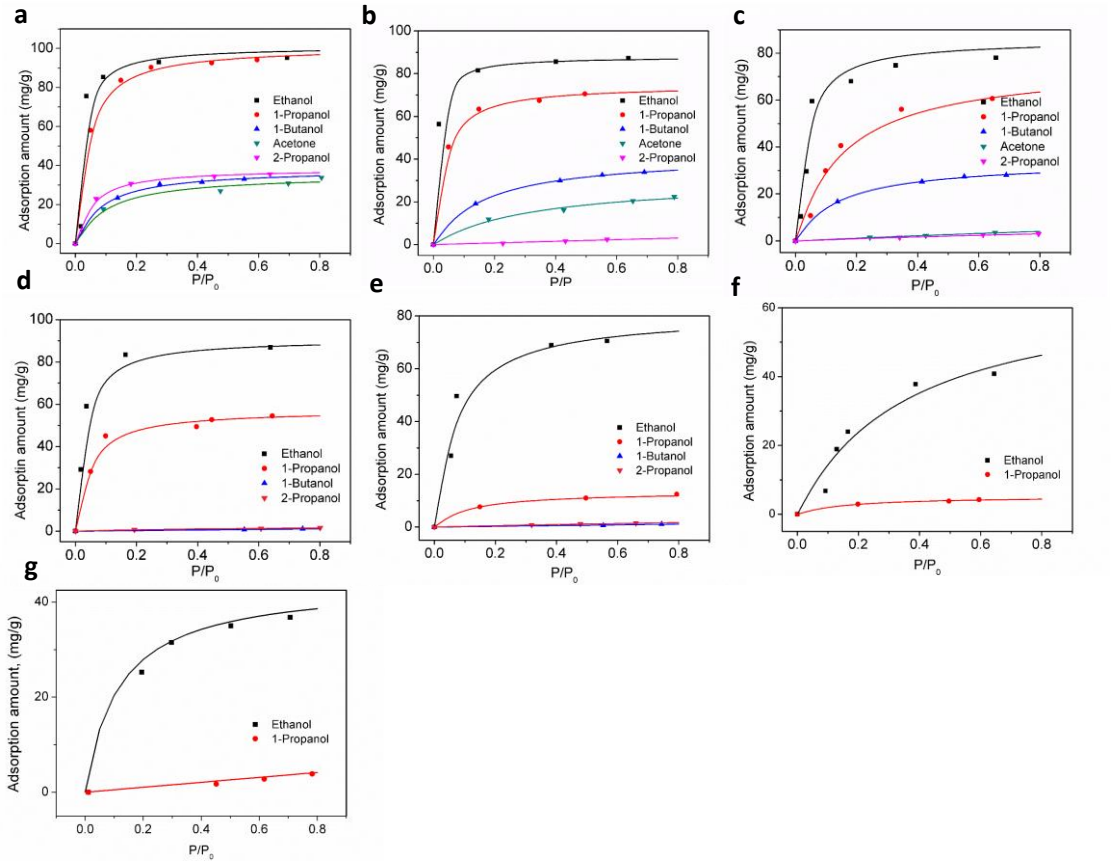

Figure 2.5: Adsorption isotherms of ethanol, 1-propanol, 1-butanol, acetone and 2-propanol at 20℃ on (a) 5A zeolite, (b) 5A-Zeolite-20, (c) 5A-Zeolite-30, (d) 5A-Zeolite-60, (e) 5A-Zeolite-120, (f) 5A-Zeolite-180, and (g) 5A-Zeolite-300. P is the vapor pressure, and P_0 is the saturation pressure. $P_{0(Ethanol)}$=50 Torr, $P_{0(1\text{-}Propanol)}$=18 Torr, $P_{0(1\text{-}Butanol)}$=7 Torr, $P_{0(Acetone)}$=201 Torr, $P_{0(2\text{-}Propanol)}$=36 Torr.

Adsorption kinetics profiles (M_t/M_∞ vs. time) of ethanol on 5A zeolite and MLD coated 5A zeolite were shown in Figure 2.7. M_t is the mass adsorbed at time t, and M_∞ is the mass adsorbed at infinite time. In these experiments, the values of M_∞ for 5A zeolite, 30, and 60 cycles of MLD coated 5A zeolite were18.8, 19.2 and 18.1 mg/g, respectively. Bare 5A zeolite showed much faster uptake of ethanol than that of MLD coated 5A zeolite.

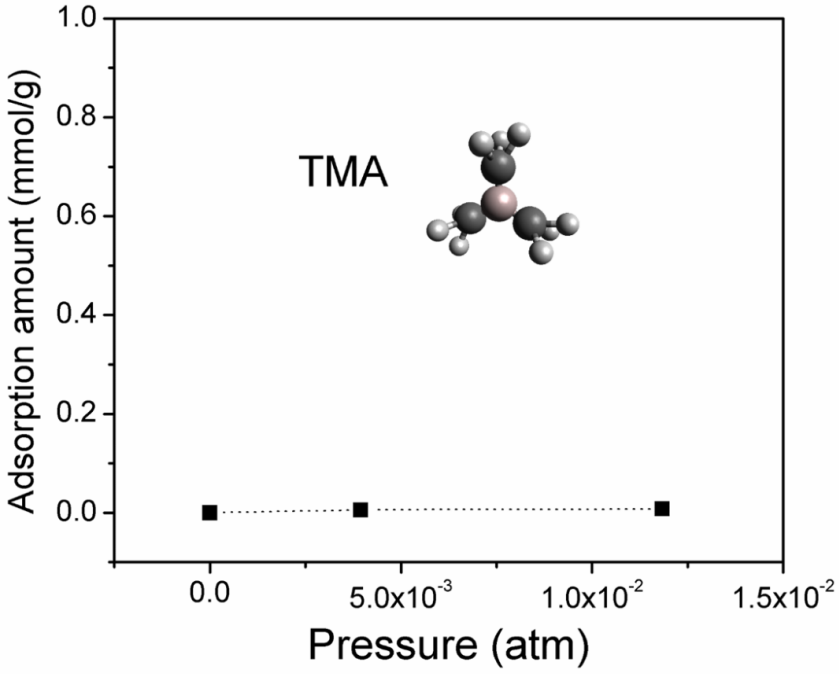

Figure 2.6 Vapor adsorption isotherm of TMA on 5A zeolite at 20℃.

However, ethanol uptake rate did not change much as the MLD cycle number increased. The ethanol diffusivity in 5A zeolite and MLD coated 5A zeolite were estimated by fitting the uptake data with a simplified solution given by Kaerger and Ruthven for short times[22]:

$$\frac{M_t}{M_\infty} = \frac{6}{\sqrt{\pi}}\sqrt{\frac{Dt}{r^2}}$$

Where D is the Fickian diffusivity, and r is the edge length of the cubic crystal. A Fickian diffusivity of 1.354×10^{-14} m^2/s was obtained for ethanol in 5A zeolite. In contrast, the

diffusivity of ethanol in 30 cycles of MLD coated 5A zeolite(1.710×10^{-17} m^2/s) and 60 cycles of MLD coated 5A zeolite (1.613×10^{-17} m^2/s) were similar and about three orders of magnitude lower than that in bare 5A zeolite. This suggests MLD coating does not dominate ethanol update process. These results demonstrate that the ethanol diffusion kinetics was drastically affected by the interface between the MLD coating and 5A zeolite but not the MLD coating thickness.

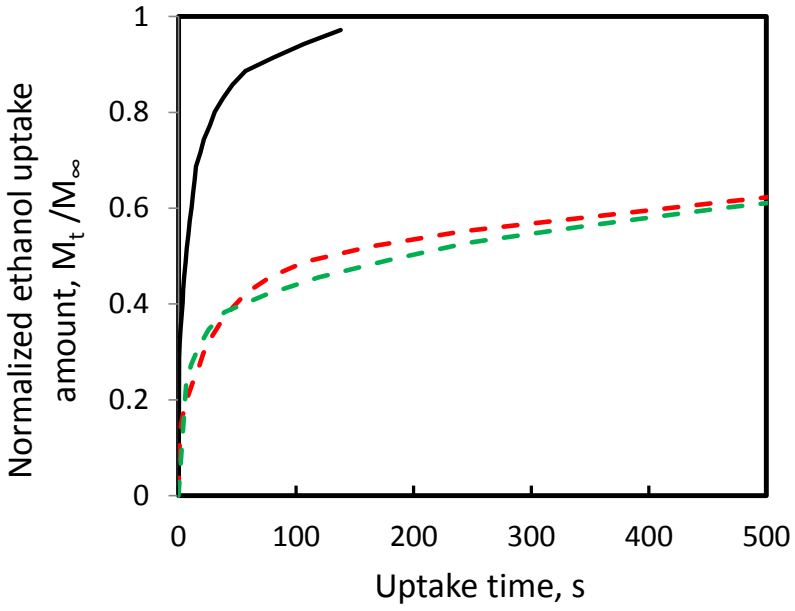

Figure 2.7 Ethanol adsorption kinetics on 5A zeolite (solid black line) and 5A-Zeolite-30 (dash red line) and 5A-Zeolite-60 (dash green line). M_t is adsorbed amount of ethanol at time t, and M_∞ is adsorbed amount at equilibrium.

2.4.1.3 LIQUID MIXTURE ADSORPTION MEASUREMENTS

5A zeolite pellets (~2.0 g) and 60 cycles of MLD coated 5A zeolite pellets (~2.0 g) were firstly outgassed at 200°C for 4 h. Then the adsorbents were sealed immediately in two 20 ml vials to avoid water uptake. After cooling down to room temperature, a 50/50 (mole ratio) ethanol/butanol liquid mixture was added into a microliter vial then placed in

the 20 ml vials with 5A zeolite and 60 cycles of MLD coated 5A zeolite. Parafilms were used to wrap tightly outside the 20 ml vials to prevent vapor evaporation. Liquid mixture samples were analyzed after adsorption at room temperature for 30 h by a 5890 SERIES II Gas Chromatography (GC) equipped with a 30 meter long, 0.25mm internal diameter Stabilwax column.

2.4.1.4 MOLECULAR DIMENSION SIMULATION

All the models of molecules (ethanol, 1-propanol, 1-butanol, acetone and 2-propanol) were generated by usingAvogadro, the geometry of the molecules was optimized under Molecular Mechanics Force Field (MMFF). Critical diameter is calculated by the diameter of the smallest cylinder that can be drawn around the molecule in its lowest energy conformer. The critical diameter of all molecules are shown in Figure 2.8.

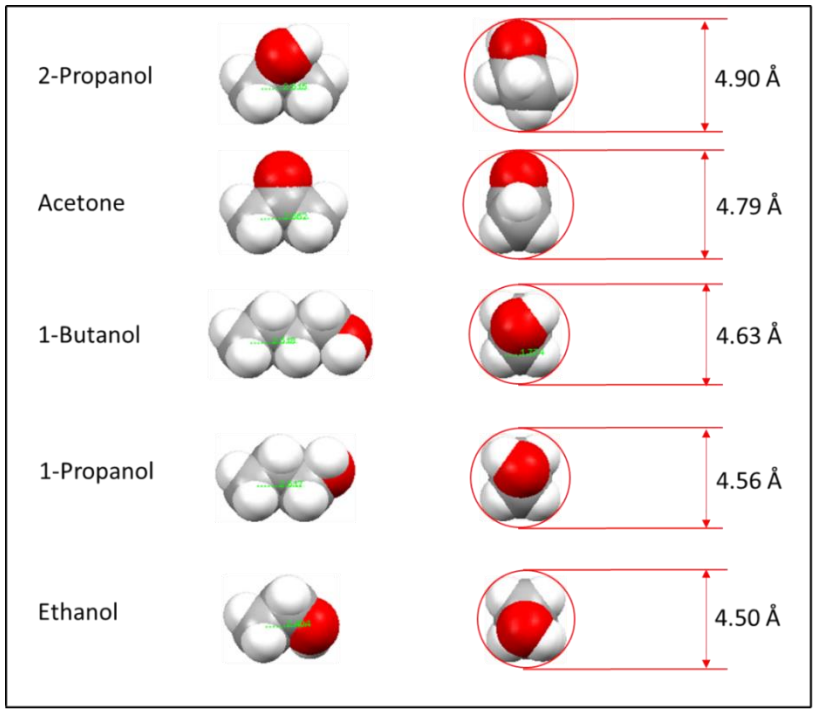

Figure 2.8 Molecular structures and critical diameters of 2-propanol, acetone, 1-butanol, 1-propanol and ethanol. Carbon atom: grey; oxygen atom: red; hydrogen atom: white.

2.4.2 CHARACTERIZATION

2.4.2.1 FIELD EMISSION SCANNING ELECTRON MICROSCOPY (FE-SEM)

The FE-SEM (Zeiss Ultraplus Thermal Field Emission Scanning Electron Microscope) image of 5A zeolite crystals were shown in Figure 2.9. 5A zeolite crystals are cubic and have an average particle size of approximately 2 μm. A proper concentration of 5A zeolite was dispersed in DI water and sonicated for 1 h and then dripped on the conductive carbon tape.

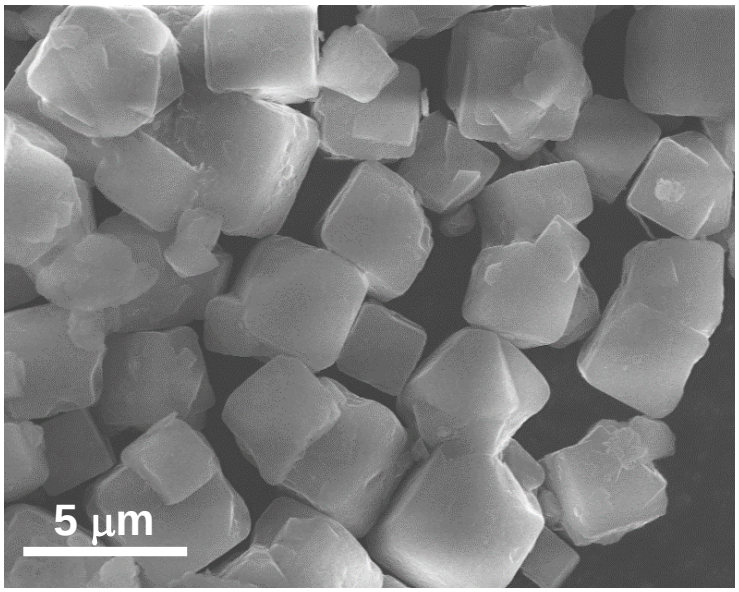

Figure 2.9 FE-SEM image of 5A zeolite.

2.4.2.2 X-RAY PHOTOELECTRON SPECTROSCOPY (XPS) ANALYSIS

The surface chemical compositions of 5A zeolite and MLD coated 5A zeolite were analyzed by XPS (Kratos Axis Ultra DLD instrument equipped with a monochromated Al Ka x-ray source and hemispherical analyzer capable of an energy resolution of 0.5 eV). As the MLD alucone coating thickness increased, much smaller amount underlying silicon can

be seen (Figure 2.10).The Al and Si atomic concentration and Al/Si ratio was listed in Table 2.1

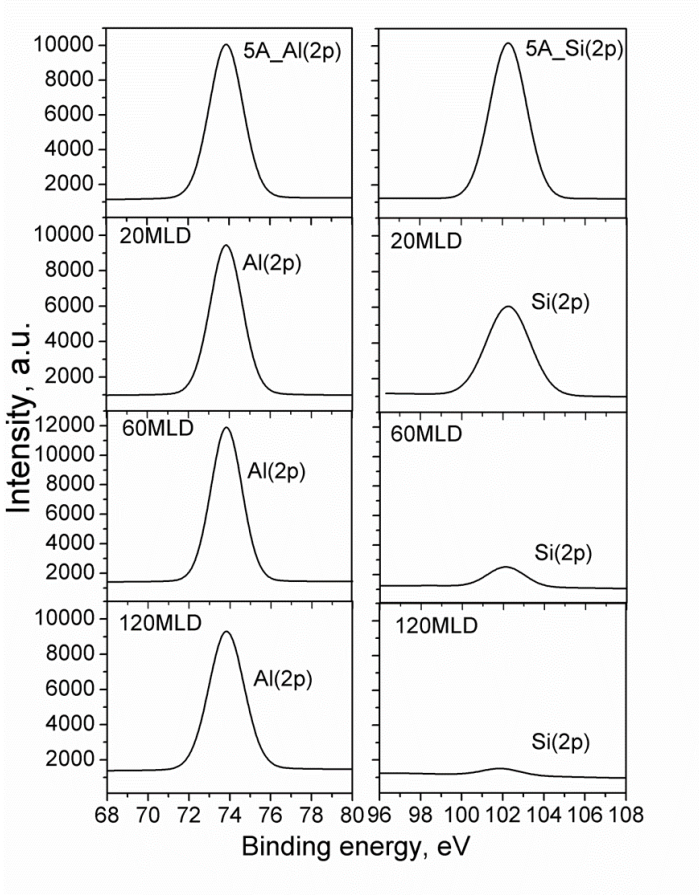

Figure 2.10 XP spectra of Al 2P and Si 2P on 5A zeolite and 5A zeolite with different cycles of MLD coatings (after calcination).

Table 2.1. Surface atomic concentrations of Al, Si, and O of 5A zeolite and 5A zeolite with different cycles of MLD coatings (after calcination), measured from XP spectra of Al 2P, Si 2P and O 1S.

Cycles of MLD on 5A zeolite	**Atomic concentration (%)**			**Al/Si ratio**
	Al	**Si**	**O**	
0	15.9	16.0	68.1	1.0
20	22.6	10.2	67.2	2.2
60	29.4	2.5	68.1	11.7
120	32.3	0.7	67.0	46.1
180	33.0	0.3	66.7	110

2.4.2.3 X-RAY DIFFRACTION (XRD)

X-ray powder diffraction (XRD) was carried out using a Rigaku MiniFlex II diffractometer with Cu Kα radiation (λ = 0.15418 nm). The diffraction data was recorded for 2θ angles between 5° and 50°. XRD pattern was shown in Figure 2.11. XRD confirmed LTA zeolite structure before and after MLD, and suggested MLD coatings were amorphous.

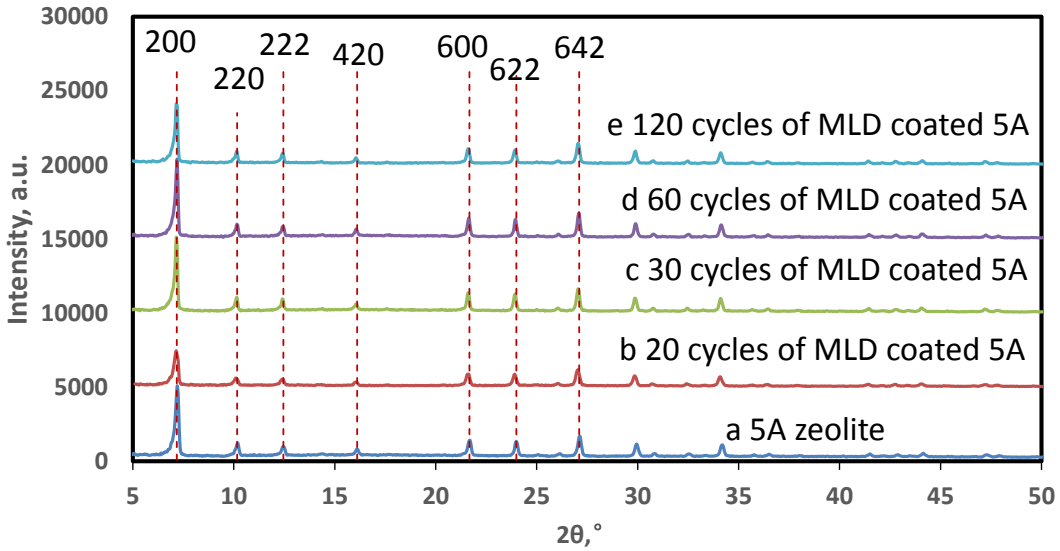

Figure 2.11 XRD patterns of 5A zeolite and 5A zeolite with different cycles of MLD coatings.

2.4.2.4 BET MEASUREMENTS

The BET surface areas were measured by a Micromeritcs ASAP 2020 unit. Prior to analysis, the materials were degassed in situ for 10 h at 250°C. The BET surface was calculated from the BET equation in the 0.05-0.3 relative pressure range and shown in Figure 2.1c.

2.4.2.5 N_2 AND Ar SORPTION ANALYSIS

N_2 adsorption isotherms at 77 K were measured on a Micromeritcs ASAP 2020 unit. Prior to analysis, the materials were degassed in situ for 10 h at 250°C. The micropore volume was analyzed by the t-plot. Pore size distribution was also calculated using adsorption branch of the isotherms. The results were shown in Figure 2.12. Figure 2.12a showed that the N_2 adsorption isotherms of 5A zeolite, 5A-Zeolite-60, and 5A-Zeolite-120 were almost the same. Figure 2.12b showed micropore volume for 5A zeolite, 5A-Zeolite-60, and 5A-Zeolite-120 are 0.195, 0.208, and 0.203 cm^3/g, respectively. This is consistent that the MLD coating is only deposited outside 5A zeolite surface. Figure 2.12c showed pore size distributions of 5A zeolite, 5A-Zeolite-60, and 5A-Zeolite-120, which were all centered at approximately 0.5 nm. This suggests MLD coating has similar pore size as 5A zeolite pores. Also, from pre-adsorption experiment (Fig. 2.3b), we concluded that MLD coating pore size is between 0.49 and 0.63 nm. This is consistent with the pore size distribution calculated from N_2 isotherms. In a very recent study from our group,[33] we deposited TiO_2 coating on 5A surface by MLD and calculated MLD coating pore size distribution using N_2 adsorption isotherms. We found a peak for TiO_2 MLD pores at ~1.1 nm, suggesting the sensitivity of using N_2 isotherms to calculate pore size distribution of MLD coating. This again supports our above conclusion that MLD coating pores are similar to 5A pores and there is no pores larger than 1 nm in the Al_2O_3 MLD coatings. Ar adsorption isotherms were also measured at 77 K (Figure 2.12d). The result again showed very similar Ar adsorption isotherms for 5A zeolite and 5A-Zeolite-60. The micropore volumes calculated by t-plot were 0.177 and 0.175 cm^3/g for 5A zeolite and 5A-Zeolite-60 (Figure 2.12e). This again shows that the micropore volume was not changed after MLD

coating deposition. Micropore volume calculated by using Ar is 10~15% less than that of N_2 (0.195 and 0.208 cm^3/g). This trend is also reported by Raj[34] for the micropore volume calculation for 13X zeolite when using N_2 and Ar.

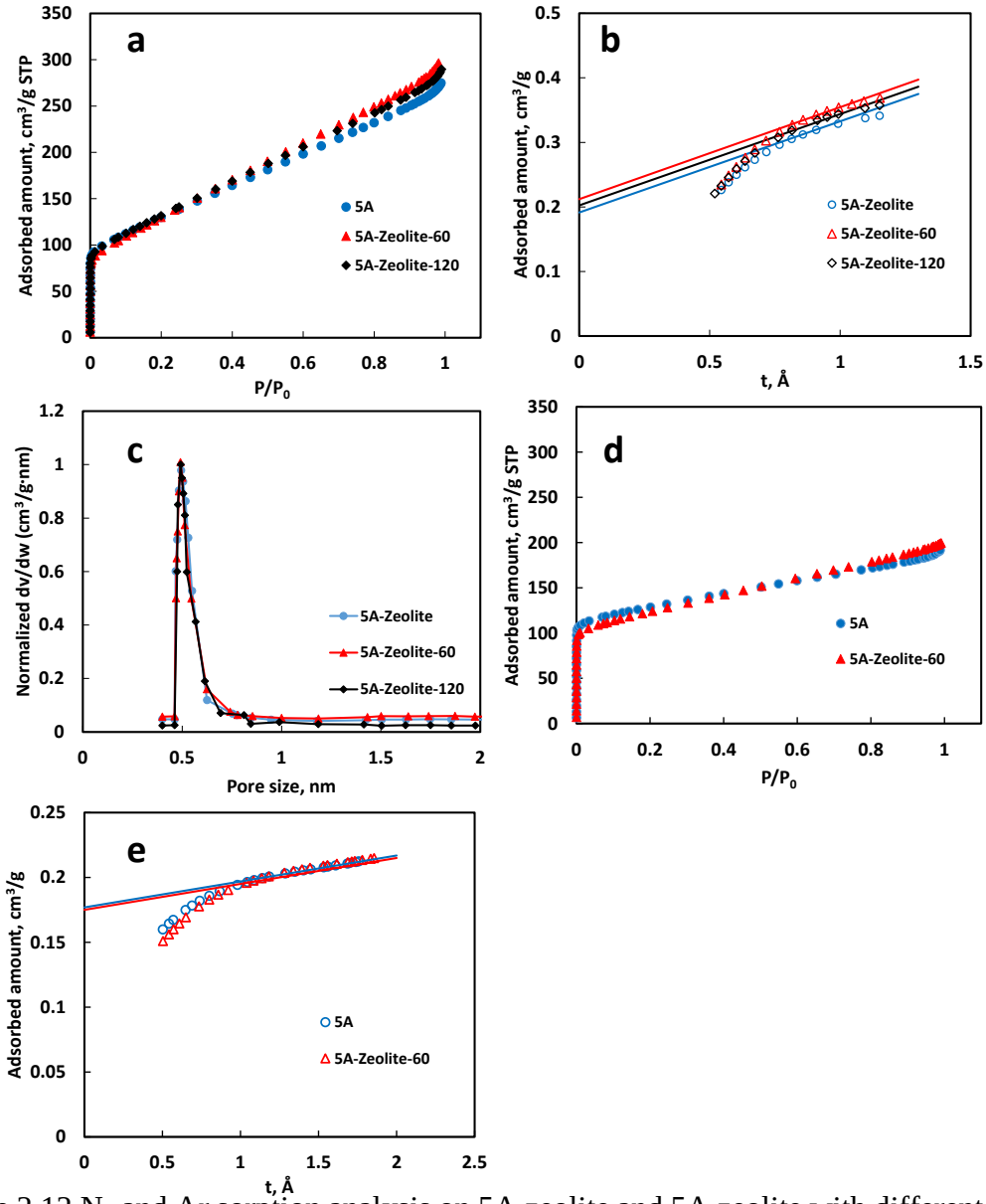

Figure 2.12 N_2 and Ar sorption analysis on 5A zeolite and 5A zeolite with different cycles of MLD coatings: (a) N_2 adsorption isotherms of 5A zeolite, 5A-Zeolite-60, and 5A-Zeolite-120 at 77 K; (b) t-plots for 5A zeolite, 5A-Zeolite-60, and 5A-Zeolite-120 calculated by using N_2; (c) Pore size distribution for 5A zeolite, 5A-Zeolite-60, and 5A-Zeolite-120; (d) Ar adsorption isotherms of 5A zeolite, and 5A-Zeolite-60 at 77 K; (e) t-plots for 5A zeolite and 5A-Zeolite-60 calculated by using Ar.

2.4.2.6 TRANSMISSION ELECTRO MICROSPOCY (TEM)

The samples were dispersed in ethanol, dropped ono a carbon-coated copper grid, and dried. The TEM (Hitachi H8000 Scanning Transmission Electron Microscope) images of MLD coated 5A zeolite were shown in Figure 2.1a and Figure 2.13. Figure 2.13a and b showed the TEM images of 5A-Zeolite-60. A uniform ~20 nm thick MLD coating was deposited on the outside surface of 5A zeolite crystal. Figure 2.13c showed ~10 nm thick MLD coating on the 5A zeolite outside surface deposited by 30 cycles of MLD. This is consistent with the layer-by-layer growth mechanism of MLD process.

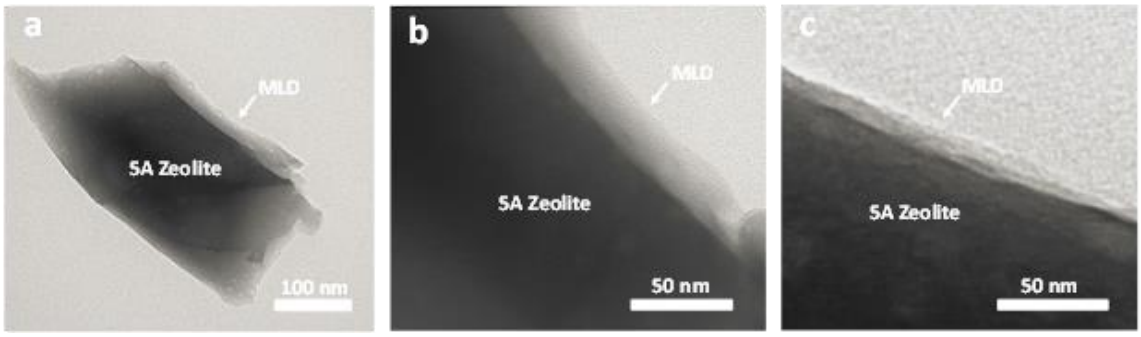

Figure 2.13 TEM images of 5A-Zeolite-60 at low (a) and high (b) magnification; (c) 5A-Zeolite-30

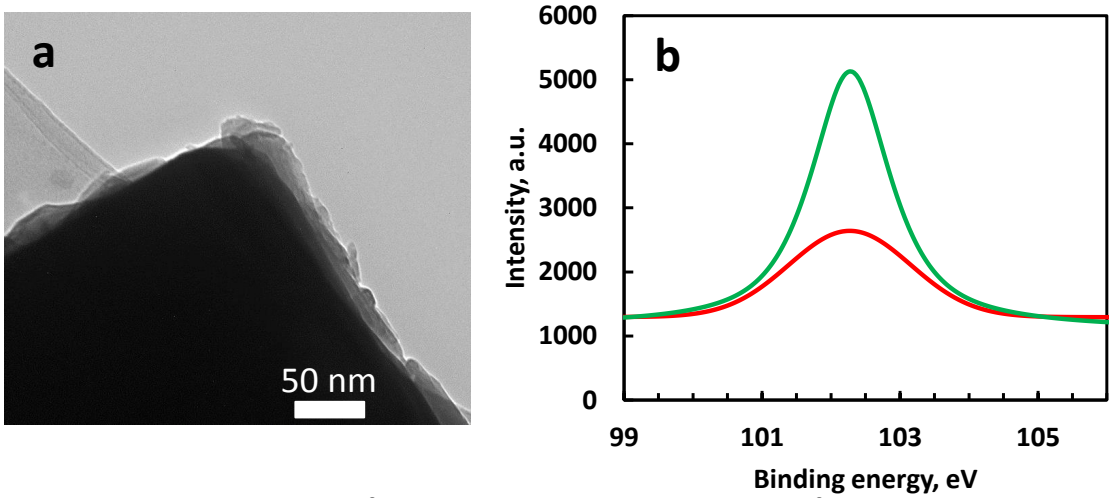

Figure 2.14 (a) TEM image of 5A-Zeolite-60C; (b) XP spectra of Si 2P on 5A zeolite with 60 cycles MLD before (red) and after (green) crushing.

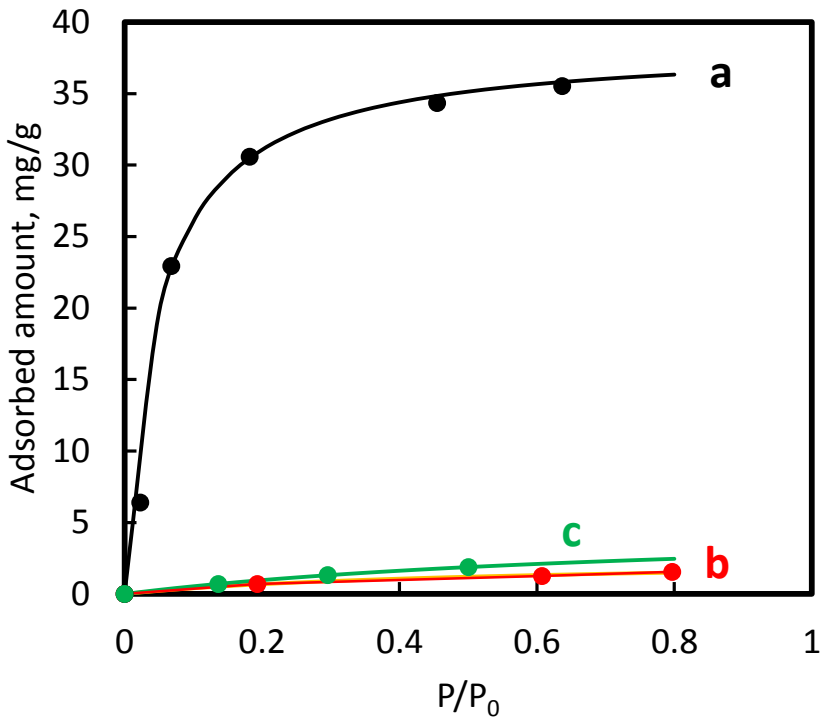

Figure 2.15 Adsorption isotherms of 2-propanol at 20℃ on (a) 5A-zeolite, (b) 5A-Zeolite-60, and (C) 5A-Zeolite-60C. P is the vapor pressure, and P_0 is the saturation pressure, $P_{0(2\text{-Propanol})}$=36 Torr.

MLD on 5A zeolite surface is expected to form a uniform, hybrid alucone coating, whose morphology and composition are expected to be independent of the coating thickness due to the self-limiting feature of the two surface reactions (Figure 2.16a) and the same substrate surface/hydroxyl group distribution and density. In addition, bonding of the alucone with 5A zeolite at the interface is also expected to be the same. During calcination, carbon compound will be removed, and the micropores will be generated in the MLD coating and the whole coating will shrink approximately 1/3, as reported before[14]. At the same time, interfacial shear force between the microporous Al_2O_3 coating and 5A zeolite will be generated due to the different thermal expansion coefficients of alumina[35] and zeolite[36]. According to an analytical model based on continuum

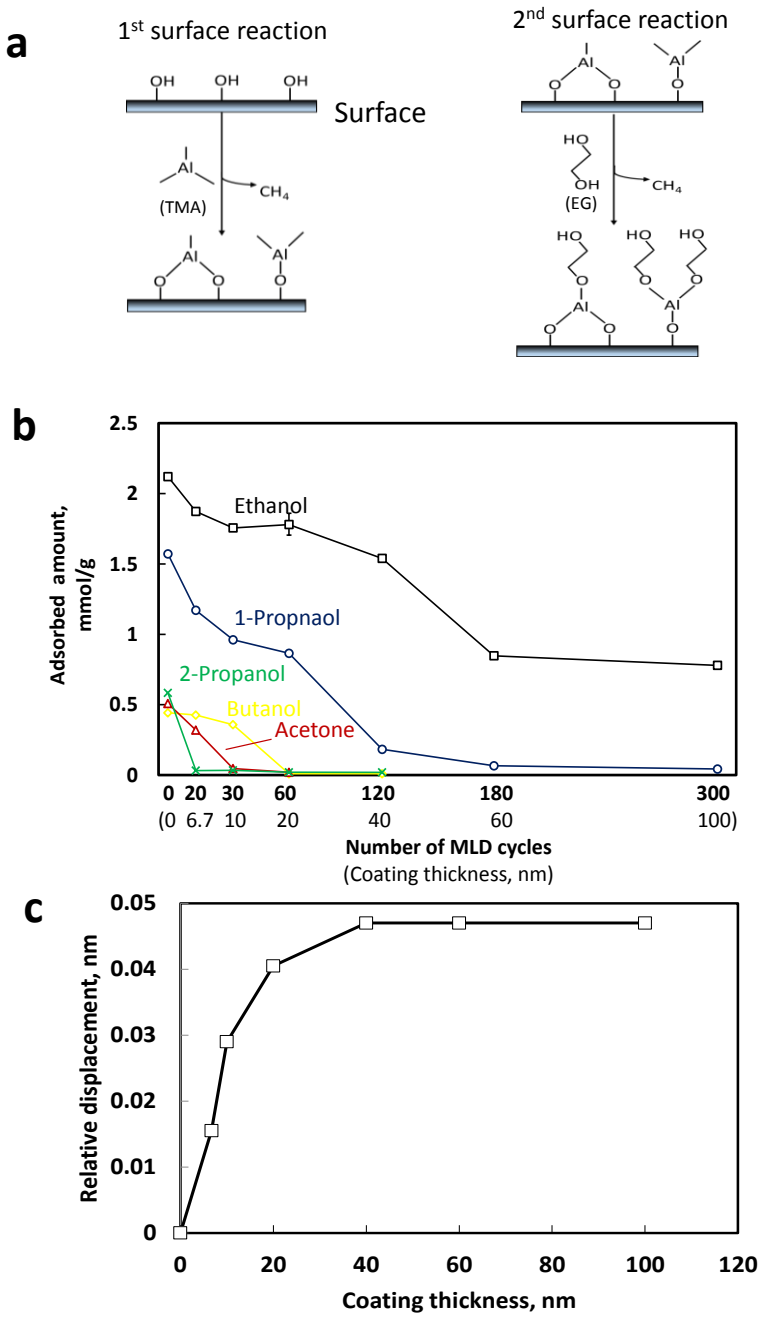

Figure 2.16 Analysis of MLD coatings on zeolite surface and pore misalignment with different MLD coating thicknesses: (a) Two self-limiting surface reactions of alucone MLD on a substrate surface; (b) Adsorbed amount of molecules with different sizes on 5A zeolite with different cycles of MLD/coating thickness up to 300 cycles/100 nm; (c) Relative displacement of the microporous Al_2O_3 coating on 5A zeolite surface vs. thickness of the coating; relative displacement is defined as the size difference between molecular "gate" and the 5A zeolite pore opening (~0.5 nm).

mixture theories, Nassar *et al*.[24] found that the interfacial thermal stress between two contacting materials increases with the increase of the adhesive/coating thickness; as a result, thicker coatings may lead to larger shift/relative displacement between two contacting materials. Figure 2.16b shows that the molecular "gate" size decreases with the increase of the coating thickness when coating is thinner than 40 nm, suggesting a continuous shift with the increase of the coating thickness. This is consistent with the modelling results. However, when the resistance, namely chemical bonding between the MLD coating and 5A zeolite surface, balances the thermal shear force, the relative movement between the Al_2O_3 coating and 5A zeolite surface stops and thus no obvious decrease of the molecular "gate" size was detected for coatings thicker than 40 nm. Figure 2.16c summarizes the relative shift/displacement between the microporous MLD coating and 5A zeolite surface, which clearly reflects the above discussed trend.

2.5 CONCLUSION

In summary, we demonstrated a completely new concept, pore misalignment, to form a size-screening "gate" on the 5A zeolite surface. The size of the "gate" can be adjusted by changing microporous alumina coating thickness, whereas the internal cavity of zeolites will be maintained. This novel concept has great potential to be utilized to fill pore size gaps of the zeolite family and to design zeolite-based molecular-sieving sorbents for selective separation of molecules with very small size differences and may potentially be used for size-selective catalysis using zeolites/molecular sieves.

2.6 ACKNOWLEDGEMENT

We gratefully acknowledge the support by the Department of Energy (DOE) Advanced Research Projects Agency-Energy (ARPA-E) under Grant No. DE-AR0000247 and by the National Science Foundation under Grant No. 1402772.

2.7 REFERENCES

[1] D.M. Ruthven, Zeolites as selective adsorbents, Chem. Eng. Prog. 84 (1988) 42-50.
[2] D.W. Breck, W.G. Eversole, R.M. Milton, T.B. Reed, T.L. Thomas, Crystalline zeolites. 1. The properties of a new synthetic zeolite, type-A, J. Am. Chem. Soc. 78 (1956) 5963-5971.
[3] B.F. Mentzen, P. Gelin, The silicalite/p-xylene system : Part I — Flexibility of the MFI framework and sorption mechanism observed during p-xylene pore-filling by X-ray powder diffraction at room temperature, Mater. Res. Bull. 30 (1995) 373-380.
[4] S.M. Kuznicki, V.A. Bell, S. Nair, H.W. Hillhouse, R.M. Jacubinas, C.M. Braunbarth, B.H. Toby, M. Tsapatsis, A titanosilicate molecular sieve with adjustable pores for size-selective adsorption of molecules, Nature 412 (2001) 720-724.
[5] P.S. Wheatley, P. Chlubná-Eliášová, H. Greer, W. Zhou, V.R. Seymour, D.M. Dawson, S.E. Ashbrook, A.B. Pinar, L.B. McCusker, M. Opanasenko, Zeolites with continuously tuneable porosity, Angewandte Chemie 126 (2014) 13426-13430.
[6] W.J. Roth, P. Nachtigall, R.E. Morris, P.S. Wheatley, V.R. Seymour, S.E. Ashbrook, P. Chlubná, L. Grajciar, M. Položij, A. Zukal, A family of zeolites with controlled pore size prepared using a top-down method, Nat. Chem. 5 (2013) 628-633.
[7] R.E. Morris, J. Čejka, Exploiting chemically selective weakness in solids as a route to new porous materials, Nat. Chem. 7 (2015) 381-388.
[8] M. Niwa, S. Kato, T. Hattori, Y. Murakami, Fine control of the pore-opening size of the zeolite mordenite by chemical vapour deposition of silicon alkoxide, Journal of the Chemical Society, Faraday Transactions 1: Physical Chemistry in Condensed Phases 80 (1984) 3135-3145.
[9] M. Niwa, M. Kato, T. Hattori, Y. Murakami, Fine control of the pore-opening size of zeolite ZSM-5 by chemical vapor deposition of silicon methoxide, The Journal of Physical Chemistry 90 (1986) 6233-6237.
[10] J.-H. Kim, A. Ishida, M. Okajima, M. Niwa, Modification of HZSM-5 by CVD of Various Silicon Compounds and Generation of Para-Selectivity, J. Catal. 161 (1996) 387-392.
[11] S. Aguado, G. Bergeret, C. Daniel, D. Farrusseng, Absolute Molecular Sieve Separation of Ethylene/Ethane Mixtures with Silver Zeolite A, J. Am. Chem. Soc. 134 (2012) 14635-14637.
[12] A. Anson, C.C.H. Lin, T.M. Kuznicki, S.M. Kuznicki, Separation of ethylene/ethane mixtures by adsorption on small-pored titanosilicate molecular sieves, Chem. Eng. Sci. 65 (2010) 807-811.

[13] M. Shi, A.M. Avila, F. Yang, T.M. Kuznicki, S.M. Kuznicki, High pressure adsorptive separation of ethylene and ethane on Na-ETS-10, Chem. Eng. Sci. 66 (2011) 2817-2822.
[14] X.H. Liang, M. Yu, J.H. Li, Y.B. Jiang, A.W. Weimer, Ultra-thin microporous-mesoporous metal oxide films prepared by molecular layer deposition (MLD), Chem. Commun. (2009) 7140-7142.
[15] H. Zhou, S.F. Bent, Fabrication of organic interfacial layers by molecular layer deposition: Present status and future opportunities, J. Vac. Sci. Technol. A 31 (2013) 18.
[16] M. Yu, H.H. Funke, R.D. Noble, J.L. Falconer, H2 separation using defect-free, inorganic composite membranes, J. Am. Chem. Soc. 133 (2011) 1748-1750.
[17] H. Zhou, M.F. Toney, S.F. Bent, Cross-linked ultrathin polyurea films via molecular layer deposition, Macromolecules 46 (2013) 5638-5643.
[18] X. Liang, J. Li, M. Yu, C.N. McMurray, J.L. Falconer, A.W. Weimer, Stabilization of Supported Metal Nanoparticles Using an Ultrathin Porous Shell, ACS Catal. 1 (2011) 1162-1165.
[19] A.A. Dameron, D. Seghete, B.B. Burton, S.D. Davidson, A.S. Cavanagh, J.A. Bertrand, S.M. George, Molecular layer deposition of alucone polymer films using trimethylaluminum and ethylene glycol, Chem. Mat. 20 (2008) 3315-3326.
[20] J.A.C. Silva, A.E. Rodrigues, Sorption and diffusion of n-pentane in pellets of 5A zeolite, Ind. Eng. Chem. Res. 36 (1997) 493-500.
[21] H. Li, Z.N. Song, X.J. Zhang, Y. Huang, S.G. Li, Y.T. Mao, H.J. Ploehn, Y. Bao, M. Yu, Ultrathin, Molecular-Sieving Graphene Oxide Membranes for Selective Hydrogen Separation, Science 342 (2013) 95-98.
[22] J. Karger, H. Pfeifer, NMR self-diffusion studies in zeolite science and technology, Zeolites 7 (1987) 90-107.
[23] M. Yu, J.C. Wyss, R.D. Noble, J.L. Falconer, 2,2-Dimethylbutane adsorption and diffusion in MFI zeolite, Microporous Mesoporous Mat. 111 (2008) 24-31.
[24] S.A. Nassar, V.L. Virupaksha, Effect of adhesive thickness and properties on the biaxial Interfacial shear stresses in bonded joints using a continuum mixture model, J. Eng. Mater. Technol. 131 (2009) 9.
[25] B.B. Bond-Watts, R.J. Bellerose, M.C.Y. Chang, Enzyme mechanism as a kinetic control element for designing synthetic biofuel pathways, Nat. Chem. Biol. 7 (2011) 222-227.
[26] G.R.M. Dowson, M.F. Haddow, J. Lee, R.L. Wingad, D.F. Wass, Catalytic conversion of ethanol into an advanced biofuel: unprecedented selectivity for n-butanol, Angew. Chem.-Int. Edit. 52 (2013) 9005-9008.
[27] S. Atsumi, T. Hanai, J.C. Liao, Non-fermentative pathways for synthesis of branched-chain higher alcohols as biofuels, Nature 451 (2008) 86-U13.
[28] T. Tsuchida, J. Kubo, T. Yoshioka, S. Sakuma, T. Takeguchi, W. Ueda, Reaction of ethanol over hydroxyapatite affected by Ca/P ratio of catalyst, J. Catal. 259 (2008) 183-189.
[29] H.S. Ghaziaskar, C.B. Xu, One-step continuous process for the production of 1-butanol and 1-hexanol by catalytic conversion of bio-ethanol at its sub-/supercritical state, RSC Adv. 3 (2013) 4271-4280.
[30] D.T. Jones, D.R. Woods, Acetone-butanol fermentation revisted, Microbiol. Rev. 50 (1986) 484-524.

[31] T.M. Yurieva, L.M. Plyasova, O.V. Makarova, T.A. Krieger, Mechanisms for hydrogenation of acetone to isopropanol and of carbon oxides to methanol over copper-containing oxide catalysts, J. Mol. Catal. A-Chem. 113 (1996) 455-468.
[32] S. Gumma, O. Talu, Gibbs dividing surface and helium adsorption, Adsorption 9 (2003) 17-28.
[33] Z.N. Song, Y. Huang, L. Wang, S.G. Li, M. Yu, Composite 5A zeolite with ultrathin porous TiO2 coating for selective gas adsorption, Chem. Commun. 51 (2015) 373-375.
[34] R.K. Vyas, Shashi, S. Kumar, Determination of micropore volume and surface area of zeolite molecular sieves by D-R and D-A equations: A comparative study, Indian J. Chem. Technol. 11 (2004) 704-709.
[35] P.F. Becher, C.H. Hsueh, S.B. Waters, Thermal-expansion anisotropy in hot-pressed sic-whisker-reinforced alumina composites, Mater. Sci. Eng., A 196 (1995) 249-251.
[36] M. Noack, M. Schneider, A. Dittmar, G. Georgi, J. Caro, The change of the unit cell dimension of different zeolite types by heating and its influence on supported membrane layers, Microporous Mesoporous Mater. 117 (2009) 10-21.

CHAPTER 3

COMPOSITE 5A ZEOLITE WITH ULTRATHIN POROUS TiO_2 COATINGS FOR SELECTIVE GAS ADSORPTION

3.1 ABSTRACT

A composite zeolite adsorbents was prepared by conformally depositing an ultrathin porous TiO_2 coating on the external surface of 5A zeolite by molecular layer deposition (MLD) and subsequent calcination. The composite adsorbent showed approximately 3 times higher ideal adsorption selectivity for CO_2/CH_4 and CO_2/N_2 and 5 times higher for propylene/propane than the bare 5A zeolite. Moreover, the composite adsorbents showed a 44 times of diffusivity difference between propylene and propane, in strong contrast with ~1 for the bare 5A. Adsorption kinetics measurements of the composite adsorbents with different thickness of porous TiO_2 coatings suggest the narrowed pores may locate at the interface of the coating and the substrate 5A zeolite.

3.2 INTRODUCTION

Adsorptive separation is an important technology for gas separation in industry [1-4]. Porous adsorbents with desirable adsorption and/or diffusion properties are essential for designing energy-efficient, adsorption-based separation processes. Zeolites/molecular sieves, a class of crystalline microporous oxides, are one of the most widely used adsorbents in adsorptive processes, because of their uniform, molecular-sized pores and

high chemical, thermal, and mechanical stabilities[5]. Despite there are more than 200 types of zeolites, not all the desired pore sizes can be found. This makes it a great challenge to achieve size-selective separation for some industrially important mixtures composed of molecules with very small size differences, such as O_2/N_2, N_2/CH_4, ethylene/ethane, propane/propylene, etc. Therefore, it would be highly favorable if the pore sizes of the zeolites/molecular sieves can be tuned to achieve adsorption separation based on very small size differences, typically ~0.01 nm.

Pores of zeolites/molecular sieves have been adjusted by simple and reliable methods, such as dehydration and ion exchanges [6-9]. For example, the effective pore size of titanium silicate ETS-4 was gradually contracted through dehydration at elevated temperature to achieve difficult size-based separations[8]; 5A zeolite pore opening was narrowed by silver exchange to successfully distinguish ethylene from ethane by molecular sieving[9]. These methods, however, are valid only for some specific zeolites and/or may not be used to continuously tune zeolite pore sizes. More effective techniques, therefore, are still needed to further fine tune zeolite pore sizes. Molecular layer deposition (MLD) is a technique to deposit hybrid coatings by conducting a series of sequential, self-limiting surface reactions on a substrate [10, 11]. The self-limiting nature of surface reactions leads to several characteristic advantages of MLD coating growth, such as exquisite control over coating thickness at sub-nanometer level and achieving continuous, conformal pinhole-free coatings on high aspect ratio structures [12-14]. Here, we report a novel use of MLD to prepare ultrathin, conformal microporous TiO_2 coatings on 5A zeolite to modify the zeolite pore opening. Porous TiO_2 coatings were formed by removing the organic compound in

the dense titanium alkoxide coatings, deposited by MLD, upon calcination in air at elevated temperature (see Supporting Information for experimental details).

3.3 EXPERIMENT RESULTS AND DISCUSSION

Field emission scanning electron microscopy (FE-SEM) shows that 5A zeolite crystals are cubic and have an average size of approximately 2 μm (Figure 3.10 in the Supporting Information). After depositing 60 cycles of MLD and calcination, an approximately 25 nm thick porous TiO_2 coating was formed on the 5A zeolite surface (Figure 3.1a), corresponding to a nominal microporous TiO_2 growth rate of 0.42 nm/cycle. X-ray diffraction (XRD) confirmed that all the peaks of 5A zeolite match those reported by Gramlich [15] before and after MLD, indicating TiO_2 MLD coatings had negligible effects on 5A zeolite crystal structure (Figure 3.9). X-ray photoelectron spectroscopy (XPS) shows the MLD coatings after calcination are TiO_2 (Table 3.1). Also, as the MLD coating cycles or coating thickness increased, the detectable amount of the underlying silicon decreased, and after 60 cycles of MLD, silicon can hardly be seen (Figure 3.1b), suggesting a continuous and uniform TiO_2 coating on the 5A zeolite surface, which effectively blocked electron penetration.

We measured the adsorption isotherms of various gas molecules with different kinetic diameters (CO_2: 0.33 nm[16]; N_2: 0.364 nm[16]; CH_4: 0.38 nm[16]; and n-C_4H_{10}: 0.46 nm[17]) to explore the effective pore sizes of the composite sorbents (Figure 3.4 and 3.5). Figure 3.2a shows the relative adsorbed amount changes of CO_2, CH_4 and butane on 5A zeolite and that with different cycles of MLD coatings. For the initial 15 cycles, adsorbed amounts of both CO_2 and CH_4 decreased approximately linearly, with higher decreasing rate of CH_4 than CO_2. This leads to almost constant ideal adsorption selectivity

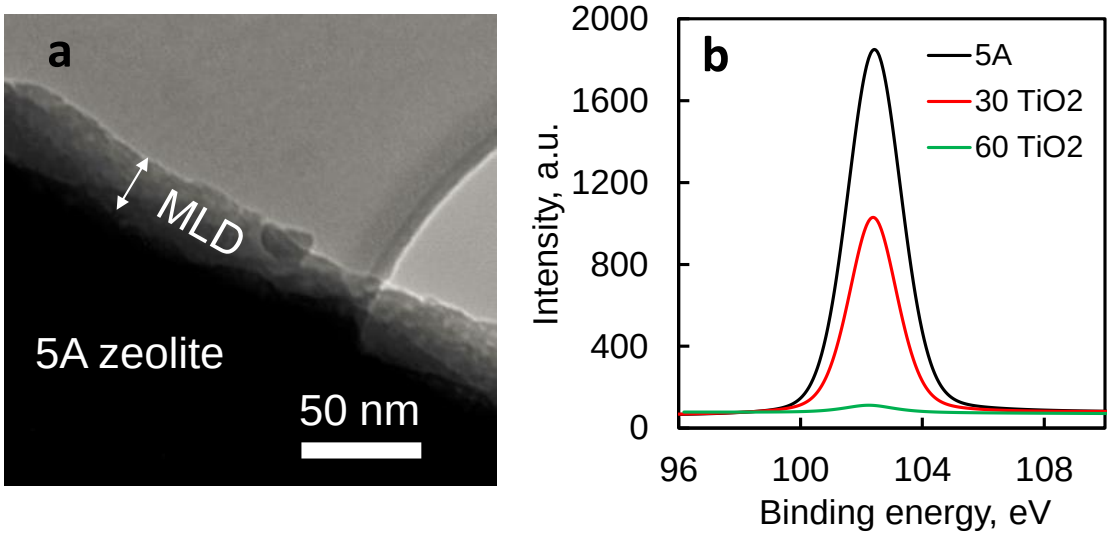

Figure 3.1 (a) Transmission electron microscopy (TEM) image of 60 cycles of TiO_2 MLD coating (after calcination) on 5A zeolite. (b) X-ray photoelectron spectroscopy (XPS) spectra of Si 2P of 5A zeolite with (30 and 60 cycles) and without MLD coatings.

of CO_2 over CH_4. From 15 to 30 cycles, adsorbed amount of CO_2 decreased following the same trend, but that of CH_4 decreased even faster, resulting in an increased selectivity from 8.7 to 15.2. From 30 to 60 cycles, adsorbed amount of CO_2 kept almost constant, while that of CH_4 decreased about another 50%. Although butane showed a similar linear decrease below 15 cycles, a sharp decrease was seen between 15 and 30 cycles; from 30 to 60 cycles, its adsorbed amount decreased to half of that at 30 cycles. As a result, the ideal adsorption selectivity of CO2 over butane increased drastically from 1.9 (bare 5A) to 24.9 (5A with 60 MLD cycles). This suggests with a microporous TiO_2 coating, formed from 60 cycles of MLD, the composite 5A sorbent should have an effective pore size smaller than butane (0.46 nm). Figure 3.2b shows that compared with bare 5A, ideal adsorption selectivity of CO_2 over N_2 and over CH_4 increased 2 and 1.8 times for 30 MLD cycles and 3.1 and 2.9 times for 60 MLD cycles, respectively. This seems to suggest that the average pore size may become smaller than N_2 and CH_4 after 60 cycles of MLD, although there may be a pore size distribution of the composite 5A adsorbents so both N_2 and CH_4 can still be

adsorbed. These results demonstrate 5A zeolite composite adsorbents with ultrathin (~25 nm) microporous TiO_2 coating may be a promising candidate for CO_2 capture in post combustion or CO_2 separation in nature gas purification. The high CO_2 selectivity and capacity of the 60 cycles of TiO_2 coated 5A zeolite composite adsorbents are comparable to other recent works [18-20].

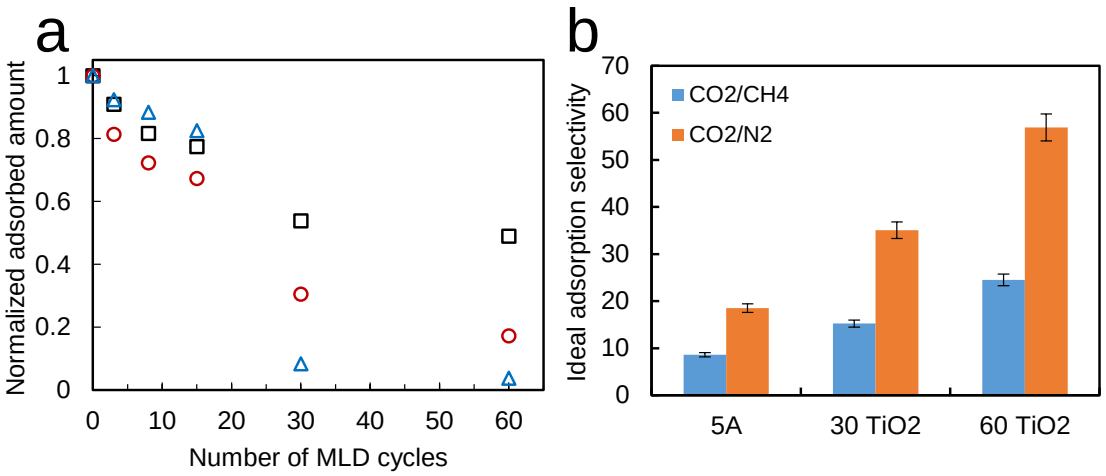

Figure 3.2 (a) Normalized sorption capacity change with the number of MLD coating cycles on 5A: CO_2 (□), CH_4 (○), and butane (Δ). (b) Ideal adsorption selectivity of CO_2/CH_4 and CO_2/N_2 on 5A and 5A with 30 and 60 cycles of MLD. All the sorption capacity is at 50 kPa and 20 ℃. As a reference, sorption capacities of CO_2, CH_4 and butane on 5A are 1.86, 0.22 and 0.97 mmol/g, respectively.

To understand the adsorption selectivity increase when MLD cycle numbers were ≥ 30, we firstly studied the coating quality by measuring CH_4 adsorption on 5A zeolite with MLD coatings that were not calcined and thus expected to be dense. Indeed, after 30 cycles of MLD, no measurable CH_4 uptake was seen (Figure 3.6). This is consistent with the dense MLD coating assumption. However, after 15 cycles of MLD, approximately 20% of CH_4 can still be adsorbed, compared with bare 5A. Apparently, 15 cycles of MLD did not form a continuous coating on the 5A zeolite surface, and thus the underneath zeolite pores may still be exposed. Therefore, a dense initial MLD coating is essential for reducing the effective pore size of the 5A composite sorbent. Since one precursor for the MLD, TiCl4

(0.64nm[21]), is much larger than 5A zeolite pore size, MLD coatings are expected to be on the external surface of 5A zeolite only. Therefore, the narrowest pores may locate at the interface between the porous TiO_2 coating and 5A zeolite or in the porous TiO_2 coating. We speculate the bottleneck is located at the interface, as supported by the diffusion rate measurements discussed below. Besides, it is likely that some zeolite pores have been blocked by the microporous TiO_2 coating on the 5A zeolite surface and thus not available for gas uptake. This may explain why the adsorbed amount for all the molecules decreased.

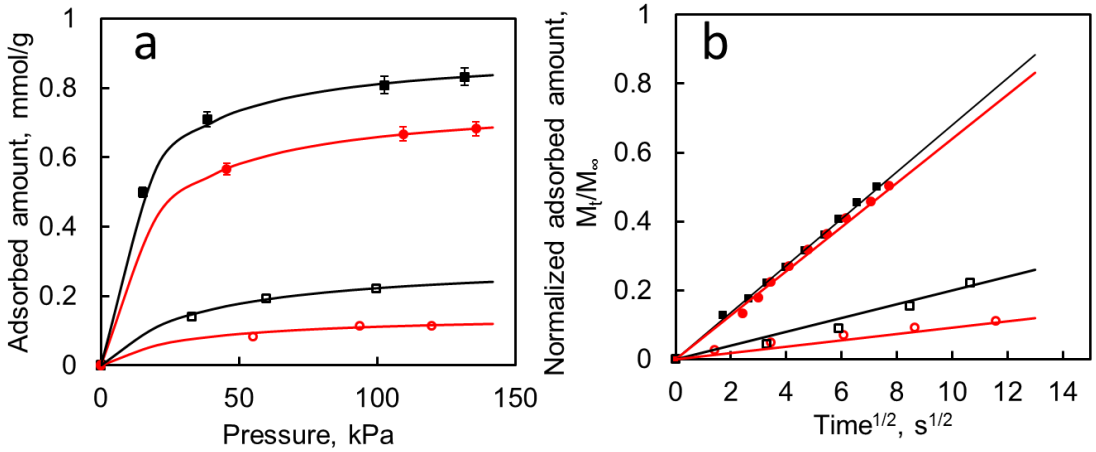

Figure 3.3 (a) Adsorption isotherms of propylene (■ and ●) and propane (□ and ○) on 30 cycles (squares) and 60 cycles (circles) of TiO_2 MLD coated 5A zeolite at 20 ℃. Solid lines are from Langmuir model fitting. (b) Adsorption uptake curves of propylene (■ and ●) and propane (□ and ○) on 30 cycles (squares) and 60 cycles (circles) of TiO_2 MLD coated 5A zeolite at 20 ℃. Mt is the adsorbed amount at time t, and M∞ is the adsorbed amount at equilibrium. Lines are from linear fitting.

As concluded above, with a microporous TiO_2 coating formed from 60 cycles of MLD the effective pore size is expected to be smaller than butane (0.46 nm) but may have a pore size distribution that covers the sizes of CO_2 and CH_4. To test the potential of the composite sorbent for separating other gas mixtures, we selected two important molecules, propane and propylene. Separation of propane/propylene mixtures is one of the most important and energy-consuming operation in the petrochemical industrial [22, 23].

Adsorption-based processes may work as an energy-efficient alternative for propane/propylene separation[9]. The critical diameters of propane and propylene are 0.446 and 0.431 nm, respectively [24]. Therefore, significantly increased adsorption selectivity of propylene over propane, after 60 cycles of MLD coating, is expected. Adsorption isotherms of propane and propylene on bare 5A zeolite (Figure 3.7), 5A with 30 and 60 cycles of MLD are shown in Figure 3.3a. The ideal adsorption selectivity of propylene over propane at 100 kPa increased from 1.2 for bare 5A to 3.7 and 6.0 for the composite sorbent with 30 and 60 cycles of MLD coatings. Consistent with the other gas adsorption results above, adsorbed amount of propylene decreased approximately 44%. We also measured uptake kinetics of propylene and propane on 5A zeolite (Figure 3.8) and 5A composite adsorbent with 30 and 60 cycles of MLD (Figure 3.3b). When the microporous TiO_2coating thickness was doubled assuming a constant coating deposition rate, propylene adsorption kinetics was hardly affected. This suggests the major transport resistance is not in the MLD coating and the narrowest pores may locate at the interface between the microporous TiO_2 coating and 5A zeolite pores. The diffusivity ratio of propane to propylene for 5A zeolite and MLD coated 5A zeolite was estimated using an equation given by Kaerger and Ruthven for short time[25], D(propylene)/D(propane), increased drastically from ~1 for 5A to ~12 and ~44 for coated 5A zeolite with 30 and 60 cycles of MLD coatings. Therefore, 5A composite sorbent shows great potential of achieving effective propylene/propane separation based on both equilibrium uptake and diffusivity differences.

3.4 SUPPORTING INFORMATION

3.4.1 MATERIALS AND METHODS

3.4.1.1.MOLECULAR LAYER DEPOSITION ON 5A ZEOLITE

We used 5A zeolite from W.R.Grace & Co.-Conn. Zeolite samples were firstly outgassed at 200°C for 4 hours. The titanium alkoxide MLD films were prepared by using titanium tetrachloride ($TiCl_4$; 99.9%, Sigma Aldrich) and ethylene glycol ($HO(CH_2)_2OH$; 99%, Alfa Aesar). Each MLD cycle started with 240 second vacuum, then ethylene glycol was diffused into the reactor with a partial pressure of 50 mTorr and then settled for 120 second, 240 second vacuum was followed to evacuate extra unreacted ethylene glycol. Ultrahigh purity N_2 (Airgas) was used as the purge at 20 sccm for 30 second. Then 240 second vacuum was applied to evacuate N_2. After that, $TiCl_4$ was diffused into the reactor with a partial pressure of 150 mTorr and then settled for 120 second, followed by 240 second vacuum to evacuate extra unreacted $TiCl_4$. Ultrahigh purity N_2 (Airgas) was used as the purge at 20 sccm for 30 second. Then 240 second vacuum was applied to evacuate N_2. This whole process is one titanium alkoxide MLD cycle. Each cycle MLD was deposited on the zeolite sample at 100 °C. Then the coated samples were heated in air from room temperature to 250°C at a rate of 1°C/min^{-1}, kept at 250°C for 4 hours, and then cooled to room temperature at the same rate.

3.4.1.2 ADSORPTION EQUILIBRIUM AND KINETICS MEASUREMENTS

Ultra-high purity CO_2 (99.999%), N_2 (99.999%), CH_4 (99.999%), chemically pure 2.0 grade propane and n-butane were purchased from Airgas. Propylene (>99%) was purchased from Sigma-Aldrich. Gas adsorption isotherms were measured by a volumetric

method using a home-built adsorption system. Sorbent (~0.20 g) was firstly outgassed at 200 ℃ for 2 h. Helium was then used to calibrate the volume of adsorption cell with sorbent

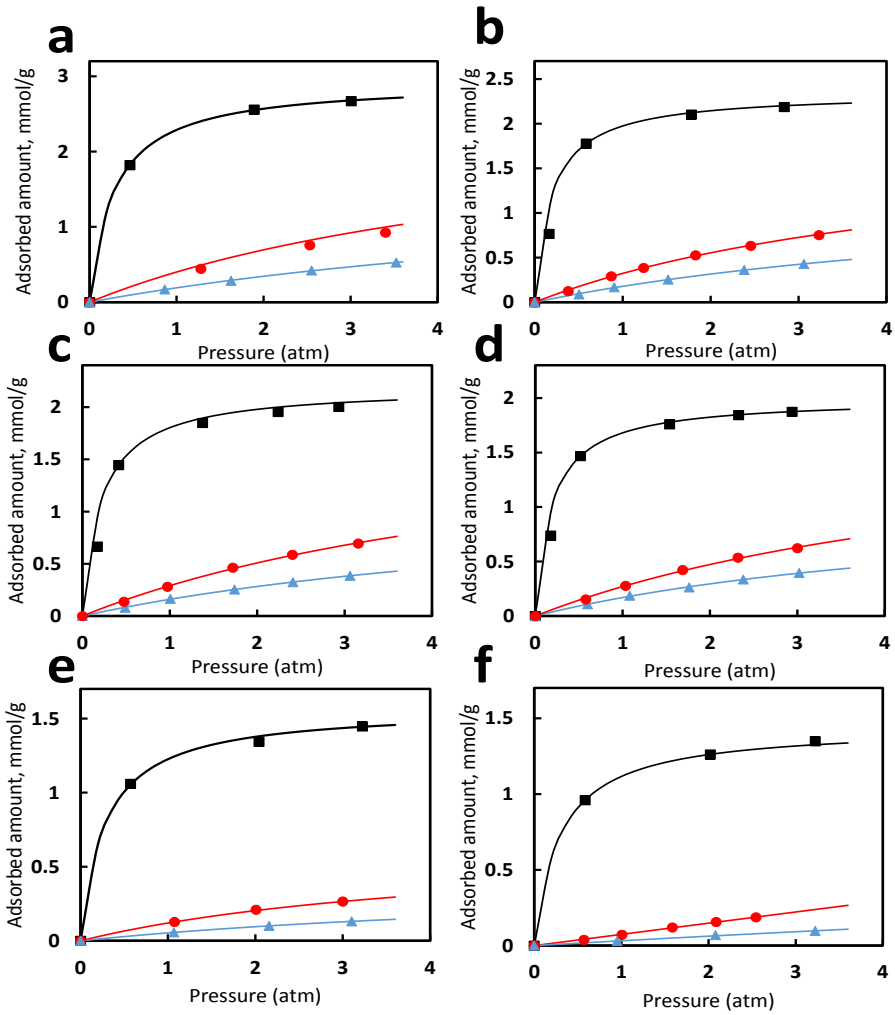

Figure 3.4 CO_2, N_2 and CH_4 adsorption isotherms at 20℃ on (a) 5A zeolite, (b) 3 cycles of TiO_2 coated 5A zeolite, (c) 8 cycles of TiO_2 coated 5A zeolite, (d) 15 cycles of TiO_2 coated 5A zeolite, (e) 30 cycles of TiO_2 coated 5A zeolite, and (f) 60 cycles of TiO_2 coated 5A zeolite. Solid lines indicate fits from Langmuir equation. CO_2 (■), CH_4 (●), and N_2 (▲).

at 20℃. After vacuum to remove residue gasses in the adsorption system, interested gases were introduced at 20℃. The pressure change was collected in real time using a Swagelok E model transducer and LabVIEW 2012 software. CO_2, N_2 and CH_4 adsorption isotherms on 5A zeolite and 5A zeolite with different TiO_2 MLD cycles are shown in Figure 3.4. Butane adsorption isotherm on 5A zeolite and 5A zeolite with different TiO_2 MLD cycles

is shown in Figure 3.5. CH_4 adsorption isotherms on 15 cycles of TiO_2 coated 5A zeolite before calcination and 30 cycles of TiO_2 coated 5A zeolite before calcination are shown in Figure 3.6. Propylene and propane adsorption isotherm on 5A zeolite is shown in Figure 3.7. Uptake kinetics of propylene and propane on 5A zeolite is shown in Figure 3.8.

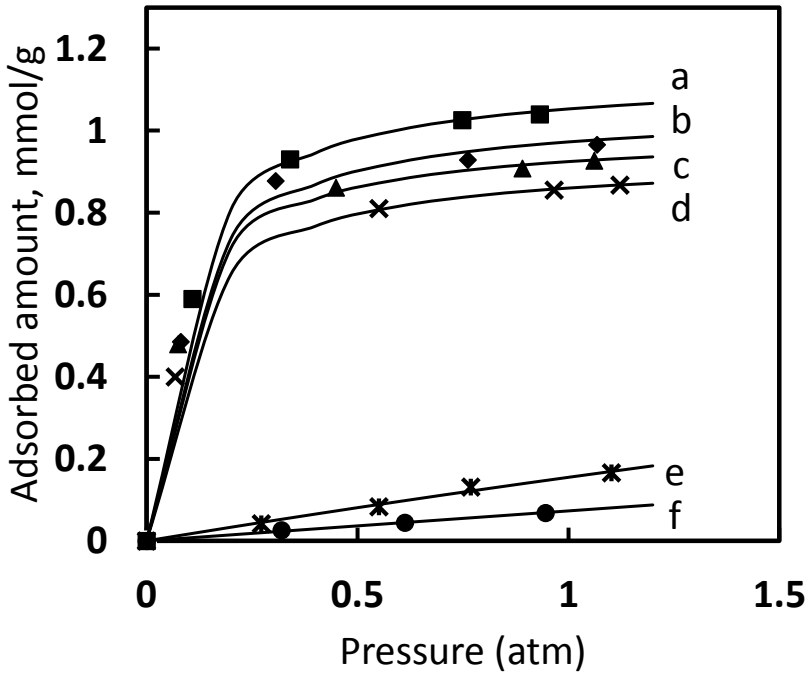

Figure 3.5 C_4H_{10} isotherms at 20℃ on (a) 5A zeolite, (b) 3 cycles of TiO_2 coated 5A zeolite, (c) 8 cycles of TiO_2 coated 5A zeolite, (d) 15 cycles of TiO_2 coated 5A zeolite, (e) 30 cycles of TiO_2 coated 5A zeolite, and (f) 60 cycles of TiO_2 coated 5A zeolite. Solid lines indicate fits from Langmuir equation.

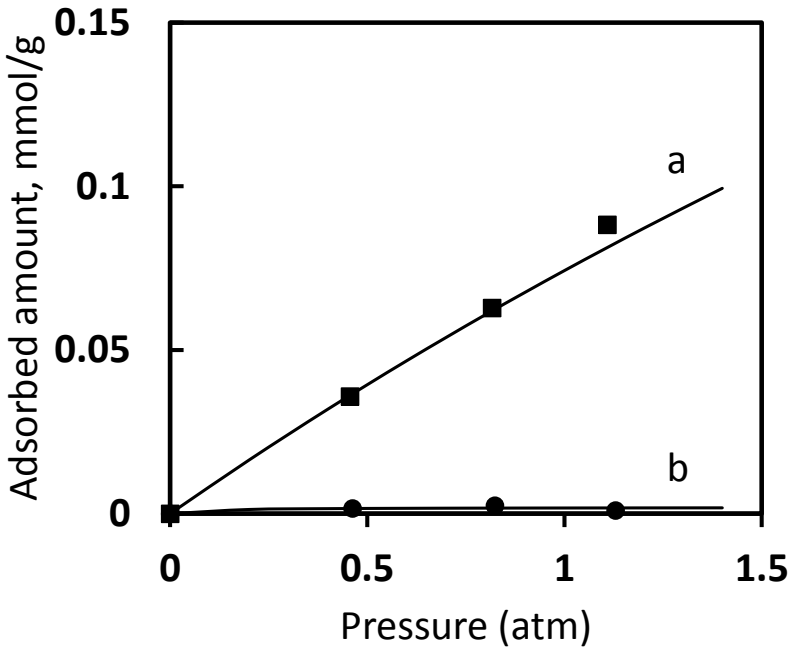

Figure 3.6 CH_4 isotherms at 20℃ on (a) 15 cycles of TiO_2 coated 5A zeolite before calcination, (b) 30 cycles of TiO_2 coated 5A zeolite before calcination. Solid lines indicate fits from Langmuir equation.

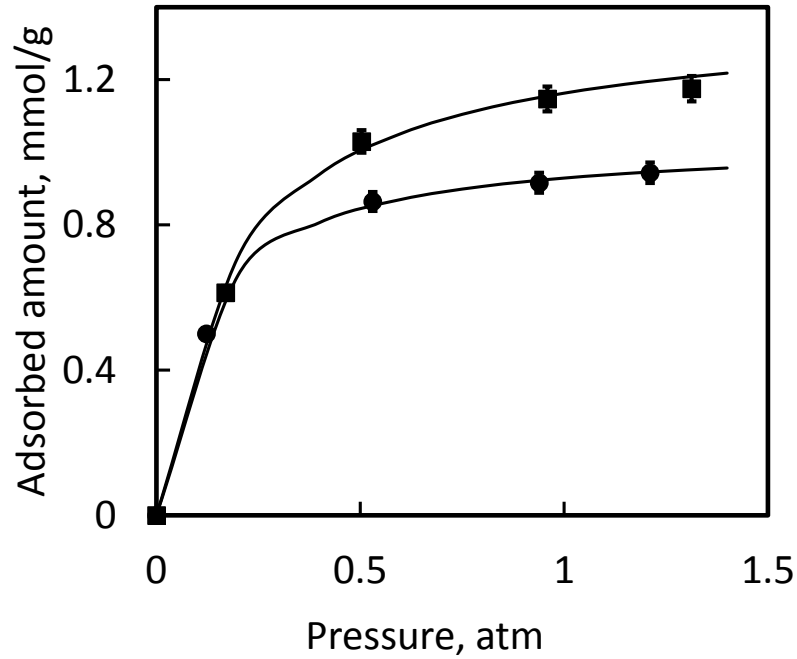

Figure 3.7 Adsorption isotherms of propylene (■) and propane (●) on 5A zeolite at 20 ℃. Solid lines are from Langmuir model fitting.

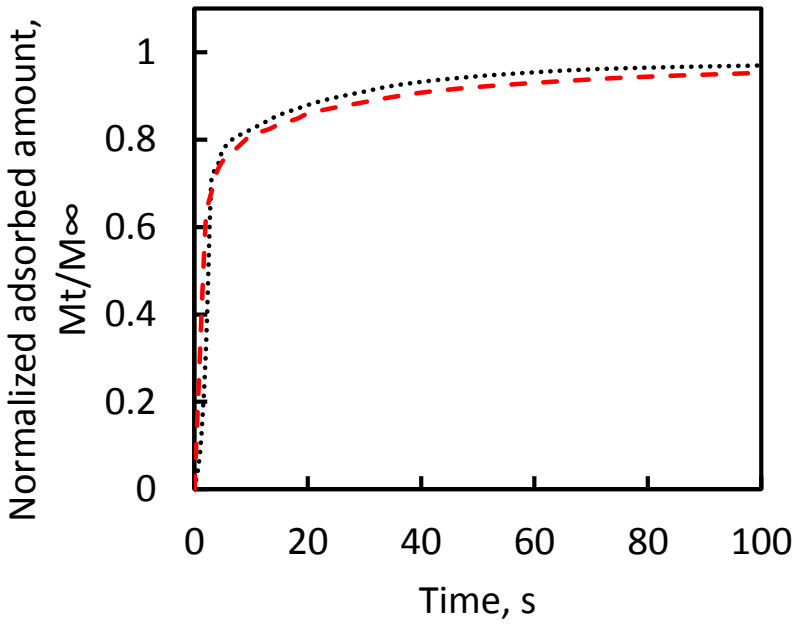

Figure 3.8 Adsorption uptake curves of propylene (red dash line) and propane (black dot line) on 5A zeolite at 20 ℃. M_t is the adsorbed amount at time t, and M_∞ is the adsorbed amount at equilibrium.

3.4.2 CHARACTERIZATION

3.4.2.1 X-RAY DIFFRACTION (XRD)

X-ray powder diffraction (XRD) was carried out using a Rigaku MiniFlex II diffractometer with Cu Kα radiation (λ = 0.15418 nm). The diffraction data was recorded for 2θ angles between 5° and 50°. The scanning rate is 2°/min. XRD pattern of 5A zeolite and 5A zeolite with different TiO_2 MLD coating were shown in Figure 3.9.

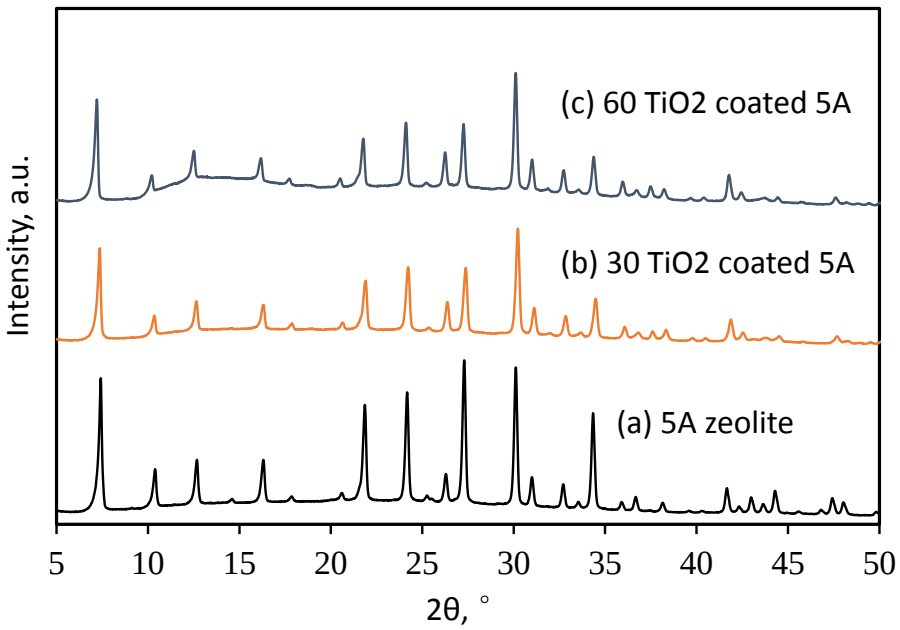

Figure 3.9 XRD patterns. (a) 5A zeolite, (b) 30 cycles of TiO_2 coated 5A zeolite, (c) 60 cycles of TiO_2 coated 5A zeolite.

3.4.2.2 X-RAY PHOTOELECTRON SPECTROSCOPY (XPS) ANALYSIS

The surface chemical compositions of 5A zeolite and TiO_2 MLD coated 5A zeolite were analyzed by XPS (Kratos Axis Ultra DLD instrument equipped with a monochromated Al Ka x-ray source and hemispherical analyzer capable of an energy resolution of 0.5 eV). Table 3.1 shows the MLD coatings after calcination are TiO_2. As the MLD coating thickness increased, much smaller amount underlying silicon can be seen (Figure 3.1b).

Table 3.1 Surface atomic concentrations of Al, Si, O and Ti of 5A zeolite and 5A zeolite with different cycles of MLD coatings (after calcination), measured from XPS spectra of Al 2P, Si 2P, O 1S and Ti 2P.

Cycles of MLD on 5A zeolite	Atomic concentration (%)			
	Al	Si	O	Ti
0	15.3	15.0	69.7	0.0
30	4.8	6.8	67.0	21.4
60	1.9	1.7	72.9	23.5

3.4.2.3.FIELF EMISSION SCANNING ELECTRON MICROSCOPY (FE-SEM)

The FE-SEM (Zeiss Ultraplus Thermal Field Emission Scanning Electron Microscope) images of 5A zeolite crystals were shown in Figure 3.10. 5A zeolite pellet were firstly crushed into powder. Then a proper concentration of 5A zeolite sample was loaded on the conductive carbon tape.

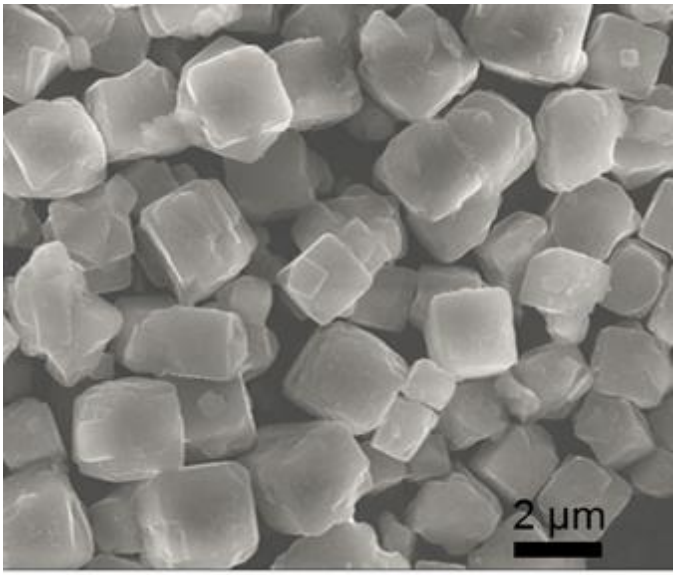

Figure 3.10 FE-SEM image of 5A zeolite.

3.4.2.4 TRANSMISSION ELECTRON MICROCSOPY (TEM)

The TEM (Hitachi H8000 Scanning Transmission Electron Microscope) images of 60 cycles of MLD coated 5A zeolite were shown in Figure 3.1b. 5A zeolite pellet were firstly crushed into powder. A proper concentration of 5A zeolite was dispersed in DI water and sonicated for 30 minute and then dripped on the TEM carbon grids.

3.5 CONCLUSION

In summary, the work reported here represents the first attempt of depositing ultrathin porous TiO_2 coatings by MLD on the 5A zeolite surface to modify zeolite pore sizes. The pore sizes were effectively reduced by a ~25-nm thick, microporous TiO_2 coating on 5A zeolite surface. As a result, adsorption selectivities for CO_2/N_2, CO_2/CH_4 and propylene/propane were significantly increased. We expect this approach can be applied, in principle, to other zeolite/molecular sieves, or zeolite membranes to fine tune the pore size and increase selectivity.

3.6 REFERENCES

[1] J.R. Li, R.J. Kuppler, H.C. Zhou, Selective gas adsorption and separation in metal-organic frameworks, Chem. Soc. Rev. 38 (2009) 1477-1504.
[2] H. Jarvelin, J.R. Fair, ADSORPTIVE SEPARATION OF PROPYLENE PROPANE MIXTURES, Ind. Eng. Chem. Res. 32 (1993) 2201-2207.
[3] C.L. Cavalcante, Industrial adsorption separation processes: Fundamentals, modeling and applications, Latin Am. Appl. Res. 30 (2000) 357-364.
[4] K.S. Knaebel, FOR YOUR NEXT SEPARATION CONSIDER ADSORPTION, Chem. Eng. 102 (1995) 92-&.
[5] D.M. Ruthven, Zeolites as selective adsorbents, Chem. Eng. Prog. 84 (1988) 42-50.
[6] T.M. Nenoff, J.B. Parise, G.A. Jones, L.G. Galya, D.R. Corbin, G.D. Stucky, Flexibility of the zeolite RHO framework. In situ X-ray and neutron powder structural characterization of cation-exchanged BePO and BeAsO RHO analogs, J. Phys. Chem. 100 (1996) 14256-14264.

[7] D.W. Breck, W.G. Eversole, R.M. Milton, T.B. Reed, T.L. Thomas, CRYSTALLINE ZEOLITES .1. THE PROPERTIES OF A NEW SYNTHETIC ZEOLITE, TYPE-A, J. Am. Chem. Soc. 78 (1956) 5963-5971.
[8] S.M. Kuznicki, V.A. Bell, S. Nair, H.W. Hillhouse, R.M. Jacubinas, C.M. Braunbarth, B.H. Toby, M. Tsapatsis, A titanosilicate molecular sieve with adjustable pores for size-selective adsorption of molecules, Nature 412 (2001) 720-724.
[9] S. Aguado, G. Bergeret, C. Daniel, D. Farrusseng, Absolute molecular sieve separation of ethylene/ethane mixtures with silver zeolite A, J. Am. Chem. Soc. 134 (2012) 14635-14637.
[10] X.H. Liang, M. Yu, J.H. Li, Y.B. Jiang, A.W. Weimer, Ultra-thin microporous-mesoporous metal oxide films prepared by molecular layer deposition (MLD), Chem. Commun. (2009) 7140-7142.
[11] H. Zhou, S.F. Bent, Fabrication of organic interfacial layers by molecular layer deposition: Present status and future opportunities, J. Vac. Sci. Technol. A 31 (2013) 18.
[12] S.M. George, Atomic Layer Deposition: An Overview, Chem. Rev. 110 (2010) 111-131.
[13] H. Zhou, M.F. Toney, S.F. Bent, Cross-linked ultrathin polyurea films via molecular layer deposition, Macromolecules 46 (2013) 5638-5643.
[14] M. Yu, H.H. Funke, R.D. Noble, J.L. Falconer, H2 separation using defect-free, inorganic composite membranes, J. Am. Chem. Soc. 133 (2011) 1748-1750.
[15] V. Gramlich, W.M. Meier, CRYSTAL STRUCTURE OF HYDRATED NAA - DETAILED REFINEMENT OF A PSEUDOSYMMETRIC ZEOLITE STRUCTURE, Zeitschrift Fur Kristallographie Kristallgeometrie Kristallphysik Kristallchemie 133 (1971) 134-149.
[16] H. Li, Z.N. Song, X.J. Zhang, Y. Huang, S.G. Li, Y.T. Mao, H.J. Ploehn, Y. Bao, M. Yu, Ultrathin, Molecular-Sieving Graphene Oxide Membranes for Selective Hydrogen Separation, Science 342 (2013) 95-98.
[17] A. Corma, From microporous to mesoporous molecular sieve materials and their use in catalysis, Chem. Rev. 97 (1997) 2373-2419.
[18] Y.S. Bae, O.K. Farha, A.M. Spokoyny, C.A. Mirkin, J.T. Hupp, R.Q. Snurr, Carborane-based metal-organic frameworks as highly selective sorbents for CO(2) over methane, Chem. Commun. (2008) 4135-4137.
[19] B. Wang, A.P. Cote, H. Furukawa, M. O'Keeffe, O.M. Yaghi, Colossal cages in zeolitic imidazolate frameworks as selective carbon dioxide reservoirs, Nature 453 (2008) 207-U206.
[20] Q.L. Liu, N.C.O. Cheung, A.E. Garcia-Bennett, N. Hedin, Aluminophosphates for CO2 Separation, ChemSusChem 4 (2011) 91-97.
[21] M.A. Cameron, I.P. Gartland, J.A. Smith, S.F. Diaz, S.M. George, Atomic layer deposition of SiO2 and TiO2 in alumina tubular membranes: Pore reduction and effect of surface species on gas transport, Langmuir 16 (2000) 7435-7444.
[22] J. Padin, S.U. Rege, R.T. Yang, L.S. Cheng, Molecular sieve sorbents for kinetic separation of propane/propylene, Chem. Eng. Sci. 55 (2000) 4525-4535.
[23] R.B. Eldridge, OLEFIN PARAFFIN SEPARATION TECHNOLOGY - A REVIEW, Ind. Eng. Chem. Res. 32 (1993) 2208-2212.
[24] W. Zhu, F. Kapteijn, J.A. Moulijn, Shape selectivity in the adsorption of propane/propene on the all-silica DD3R, Chem. Commun. (1999) 2453-2454.

[25] J. Karger, H. Pfeifer, NMR self-diffusion studies in zeolite science and technology, Zeolites 7 (1987) 90-107

CHAPTER 4:

ZEOLITE COMPOSITE SORBENTS WITH MLD COATINGS FOR HIGH SELECTIVITY AND HIGH CAPACITY CO_2 CAPTURE

4.1 ABSTRACT

Greatly improved sorbents for selective CO_2 capture were prepared by controlling calcination conditions for molecular layer deposition (MLD) coated zeolites (5A and 13X). These MLD coated zeolite composite sorbents showed CO_2/N_2 selectivity as high as 43-77, increased by a factor of 2.6-4.5 compared to the uncoated zeolite sorbents, while maintaining high CO_2 adsorption capacity (1.04-2.32 mmol/g) at 0.5 bar and 25 °C. Different mechanisms of selectivity enhancement for 5A and 13X was identified.

4.2 INTRODUCTION

Since the industrial era began, human activities have had an increasing effect on climate by releasing greenhouse gases, such as carbon dioxide (CO_2), nitrous oxide (N_2O) and methane (CH_4), to the atmosphere [1]. Consequently, the average global temperature has increased by 0.6 °C in recent 100 years [2]. In 2013, Intergovernmental Panel on Climate Change (IPCC) predicts an even faster increasing trend that by the year 2100, the global temperature will increase another 1.9 °C [3]. Among all the greenhouse gases, CO_2 is considered as the largest contributor accounting for 60% of global warming effect [4].

The concentration of CO_2 in the atmosphere has increased by 40% from 280 ppm to 400 ppm over the past century [3]. Hence, it is very important to reduce CO_2 emission in the mitigation of global warming effect. However, the control of CO_2 emission is still one of the most challenging issues since the main source of CO_2 emissions is the combustion of fuels with high carbon content, such as coal, petroleum, and natural gas; simultaneously, the global development depends on the current energy supply heavily [5-7]. An effective approach of reducing CO_2 emissions without decreasing energy demand is the implementation of CO_2 capture technologies [8, 9].

CO_2 capture can be achieved by various approaches: post-combustion capture where CO_2 is separated from the other components of the flue gas, pre-combustion capture with removal of CO_2 from the fuel prior to combustion, and oxy-combustion where the fuel is burned in an oxygen stream [8]. Among these three techniques, capture of CO_2 from flue gas (post-combustion) is the focus of recent research due to the large volume of CO_2 emission from existing coal-, oil- or natural gas-fired power plants [10, 11]. Current technologies for post-combustion CO_2 capture are largely based on chemical absorption of CO_2 by liquid solvents [10, 12]. However, problems associated with equipment corrosion, high energy consumption for regeneration, and sorbent degradation, make the process complicated and costly [13]. Membrane-based separation processes have emerged as an effective alternative in post-combustion CO_2 capture [5]. Unfortunately, many membranes must be further improved to overcome the trade-off between permeability and selectivity [5]. Meanwhile, the low pressure of CO_2 within the feed stream and thus low driving force for its permeation may limit the application of membranes in post-combustion CO_2 capture compared with adsorption-based separation processes [14]. Adsorption employs porous

adsorbents and has been widely considered as a low operation cost, low energy requirement, and low maintenance method [15-18]. An ideal adsorbent should possess high surface area, high porosity, reversible adsorption/desorption capability, structure stability, and potential for surface modification.[19, 20] With regard to post-combustion CO_2 capture, a variety of adsorbents have been studied, including activated carbon, calcium oxides, hydrotalcites, zeolites, and metal oxides [21]. Among them, zeolites, especially 5A zeolite and 13X zeolite, are considered as the promising adsorbents due to their high adsorption capacity at low pressure and their excellent thermal, chemical and mechanical stability [11, 22-24]. Although zeolites have shown a relatively high CO_2 capacity, their selectivity to CO_2 over N_2 is still low [19]. Therefore, it is in a great need to develop high quality adsorbents to improve CO_2/N_2 selectivity while maintaining a high CO_2 capacity.

In our previous work, our group have shown a new method to improve adsorptive selectivity of zeolites using molecular layer deposition (MLD) technique [25, 26]. The improved adsorptive separation performance of zeolites is because of the smaller pores at the interface resulting from the misalignment between MLD porous coating pores and zeolite pores. The pore misalignment probably originates from the thermal interfacial shear stress during calcination due to the different thermal expansion coefficients between zeolites and the MLD coating. We have shown that at a constant calcination condition, the extent of pore misalignment (or relative displacement) at the interface can be controlled by the MLD coating thickness, which was consistent with Nassar's analytical modelling study for the composite materials [27]. However, when the resistance, namely chemical bonding between the MLD coating and zeolite surface, balances the thermal shear force, the relative movement between the MLD coating and zeolite surface stops and thus no more obvious

relative displacement was observed for coatings thicker than 25 nm under constant calcination condition.[26] In Pan's recent study [28], it was found that the interfacial displacement of composite materials can be influenced by varying temperatures. In this work, we fixed the TiO_2 MLD coating thickness by fixing the MLD deposition cycles, different calcination temperature and calcination residence time were investigated for MLD coated zeolite composite sorbents. We found that the adsorptive separation performance of MLD coated zeolites can be further tuned to achieve greatly improved CO_2/N_2 separation by optimizing the calcination conditions.

4.3 EXPERIMENTAL SECTION

4.3.1 MATERIALS

Ethylene glycol (99%, $HO(CH_2)_2OH$;) was obtained from Alfa Aesar. Titanium tetrachloride (99.9%, $TiCl_4$) and 13X zeolites were obtained from Sigma Aldrich. 5A zeolites were obtained from W.R. Grace & Co.-Conn.

4.3.2 TITANIUM ALKOXIDE MLD COATING

Zeolites were firstly outgassed at 200°C for 4 h for removing the adsorbed water. The titanium alkoxide MLD coatings (-Ti-O-CH_2-CH_2-O-Ti-) were prepared by using $TiCl_4$ and EG as precursors. Each MLD cycle started with 240 s vacuum. $TiCl_4$ was then introduced into the reactor until a pressure of 150 mTorr and settled for 120 s, and then 240 s vacuum was followed to evacuate extra unreacted $TiCl_4$. Ultrahigh purity N_2 (Airgas) was used to further clean the reactor with a flow rate of 20 sccm for 30 sec controlled by a mass-flow controller. Then 240 s vacuum was applied to evacuate N_2. After that, EG was diffused into the reactor until a pressure of 50 mTorr and then settled for 120 s, followed

by 240 s vacuum to evacuate extra unreacted EG. Ultrahigh purity N_2 was used as the purge gas again. Then 240 s vacuum was applied to evacuate N_2. This whole process finishes one MLD cycle, totally 60 cycles of titanium alkoxide MLD coatings were deposited on the zeolites at 100 °C. Then the coated samples were heated in air from room temperature to different elevated temperature (200 °C, 250 °C, and 350 °C) at a rate of 1°C/min, kept at elevated temperature for different residence time (1 min, 2 h, 4 h, and 8 h) and then cooled to room temperature at the same rate.

4.3.3 CHARACTERIZATION

Surface composition of zeolites before and after MLD was analyzed by X-ray photoelectron spectroscopy (XPS, Kratos Axis Ultra DLD instrument equipped with a monochromated Al Ka X-ray source and hemispherical analyzer capable of an energy resolution of 0.5 eV). The infrared (IR) spectra were taken on a Bruker equinox 55 in a diffuse reflection mode. A Praying Mantis diffuse reflection compartment was used to allow the IR beam to be reflected on powder samples. For each spectrum, 64 scans were collected to ensure high signal to noise ratio. The IR spectra were scanned in the range of 4000-1000 cm^{-1} with resolution of 4 cm^{-1}. Pore size distribution of MLD coated zeolite adsorbents were calculated using Ar adsorption branch of the isotherms measured at -196 ºC using a Micrometeritcs ASAP 2020 unit. Prior to adsorption measurement, samples were degassed in situ at 170 °C overnight.

4.3.4 GAS AND WATER ADSORPTION ISOTHERM MEASUREMENTS

Ultra-high purity CO_2 (99.999%), and N_2 (99.999%) were purchased from Airgas. Gas adsorption isotherms were measured by a volumetric method using a home-built adsorption system. Sorbent (~0.10 g) was firstly outgassed at 200 ^oC for 2 h. Helium was then used to calibrate the volume of adsorption cell with sorbent at 25 ^oC. After vacuum to remove residue gasses in the adsorption system, interested gases were introduced at 25 ^oC. The pressure change was collected in real time using a Swagelok E model transducer and LabVIEW 2012 software.

4.4 RESULTS AND DISCUSSION

MLD coating on 5A zeolite was confirmed by analyzing the surface composition of 5A zeolites before and after MLD using XPS technique. In Figure 4.1a, the spectrum for the uncoated 5A zeolite showed a strong O_{1s} photoelectron peak at 531 eV, and Na_{Auger}, Ca_{2s}, Ca_{2p}, C_{1s}, Si_{2s}, Al_{2s}, Si_{2p}, Al_{2p} peaks at 500, 440, 349, 285, 151, 138, 99, and 73 eV, respectively. This is consistent with the typical 5A zeolite chemical composition [29]. After MLD, the peaks of Na, Ca, Si, and Al disappeared (Figure 4.1b). Instead, the oxygen, titanium and carbon signals were observed at 531 eV (O_{1s}), 460 eV (Ti_{2p}), 285 eV (C_{1s}) and 33 eV (Ti_{3p}), suggesting the entire zeolite surface has been conformally covered by MLD coating. XPS is a surface characterization technique, usually with a detection depth limit around 10 nm [30]. Therefore, the XPS results verified the deposition of MLD coatings on the zeolites.

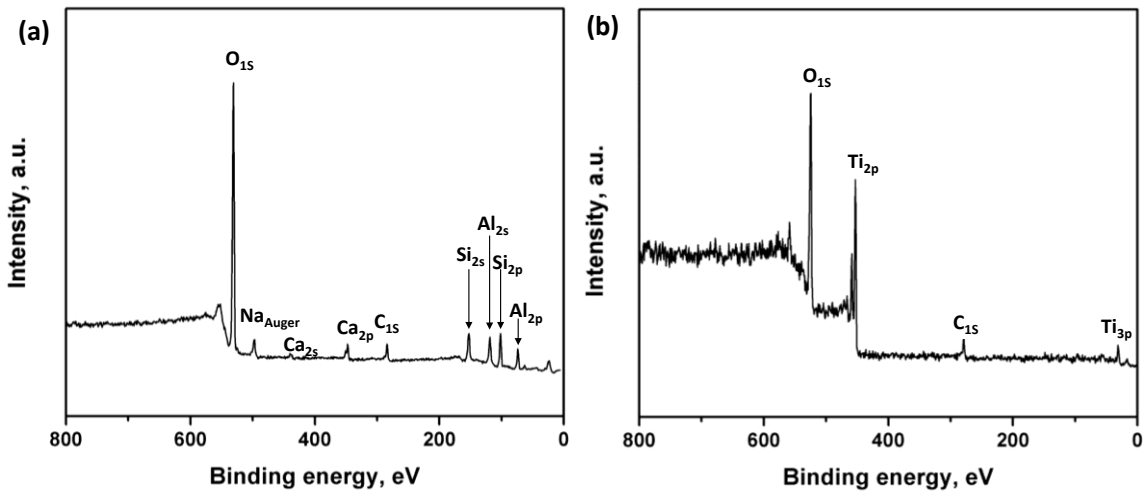

Figure 4.1. XPS spectra of uncoated 5A zeolite (a), and MLD coated 5A zeolite (b).

The successful removal of the organic compound in MLD coating by calcination was examined by IR as shown in Figure 4.2. Absorbances were observed in the range of 2890-2950 cm^{-1} only for MLD coated 5A zeolite without calcination (5A-MLD-Uncal), which correspond to the $-CH_2$ asymmetric and symmetric stretching vibrations [31, 32] in the hybrid MLD coating (-Ti-O-CH_2-CH_2-O-Ti-). After calcination at 250 ^oC for different times (1 min, 2 h and 8 h), $-CH_2$ stretching vibrations disappeared. Furthermore, a small shoulder appeared at around 1580 cm^{-1},which is the characteristic band for –OH on TiO_2 [33], suggesting that the organic compound in MLD coating was removed and the hybrid titanium alkoxide was converted to TiO_2.

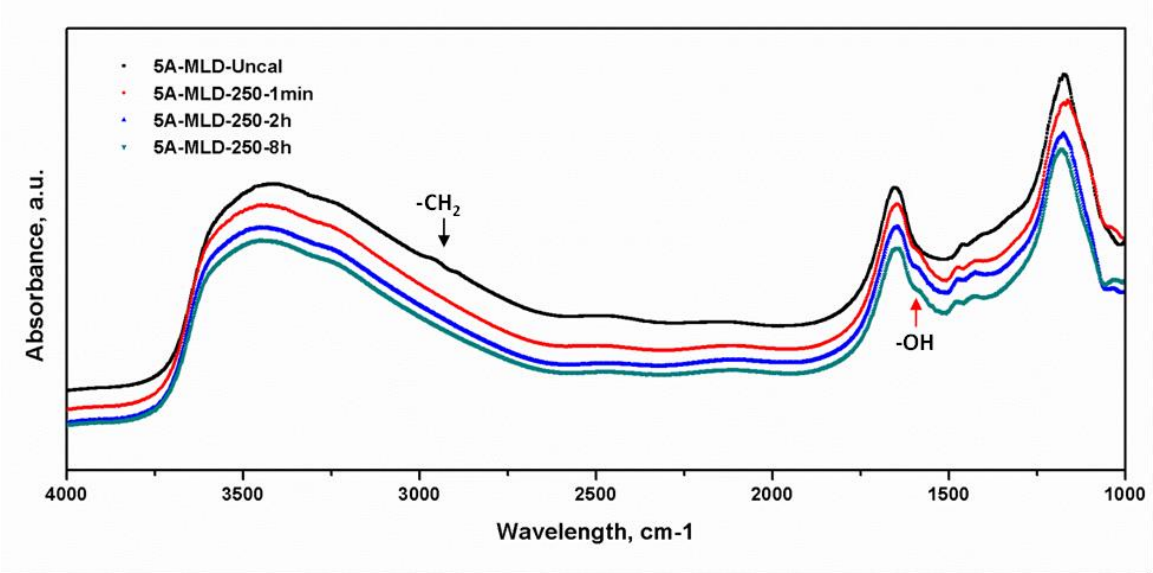

Figure 4.2. IR spectra of uncalcined MLD coated 5A zeolite and MLD coated 5A zeolite calcined at 250 °C for different time.

CO_2 and N_2 adsorption isotherms were measured on 5A zeolite and MLD coated 5A zeolite up to 3 bars as shown in Figures 4.3 and 4.4. Figure 4.3a showed the adsorption isotherms on uncoated 5A zeolite, which are consistent with literature data reported by Wang [34]. For MLD coated 5A zeolite, the calcination was firstly carried out at various residence time (1 min, 2 h, 4 h and 8 h), while maintaining the calcination temperature at 250 ^oC. These samples are labelled as 5A-MLD-250-1min, 5A-MLD-250-2h, 5A-MLD-250-4h, and 5A-MLD-250-8h, and corresponding abbreviations were used in the following discussion. Figure 4.3b-d showed adsorption loadings of both CO_2 and N_2 gradually decreased for MLD coated 5A zeolites as the calcination residence time increased from 1 min to 4 h, although adsorbed amounts of N_2 and CO_2 decreased at different rates. This led to a complex adsorption selectivity change with calcination residence time (see discussion below). However, the CO_2 and N_2 adsorption loadings increased again after 8 h calcination at 250 ^oC (Figure 4.3e). We then investigated the effect of calcination temperature (200 and

350 °C) while maintaining the residence time at 2 h. We found after calcination at 200 °C for 2 h, the adsorbed amounts of CO_2 and N_2 were still very low (< 5% of uncoated 5A) (Figure 4.4a), indicating 200 °C was not high enough to remove the organic compound in the dense hybrid MLD coating and convert it into porous coating. In contrast with the low adsorption capacity on MLD coated 5A zeolite calcined at 200 °C, high capacity of both CO_2 and N_2 (> 90% of uncoated 5A) on 5A-MLD-250-1min (Figure 4.5a) suggested that 1 min was enough to decompose the organic compound in the MLD coating when the calcination temperature was 250 °C, which is also consistent with the IR results (Figure 4.2). Figure 4.4b showed the CO_2 and N_2 adsorption isotherms when the calcination temperature increased to 350 °C. The adsorbed capacity at 0.5 bar for 5A, 5A-MLD-250-1min, 5A-MLD-250-2h, 5A-MLD-250-4h, 5A-MLD-250-8h, 5A-MLD-350-2h, and 5A-MLD-200-2h were summarized in Figure 4.5a for CO_2 (1.88, 1.79, 1.62, 1.04, 1.65, 1.52 and 0.021 mmol/g, respectively) and Figure 4.5b for N_2 (0.10, 0.090, 0.021, 0.018, 0.074, 0.035 and 0.005 mmol/g, respectively). Apparently, different calcination conditions affected the adsorptive properties of MLD coated 5A composite sorbents. Comparing with uncoated 5A zeolite, results showed that the adsorbed capacity reduction was much greater for N_2 (79%, 82% and 65%) than for CO_2 (14%, 44% and 19%) on MLD coated 5A zeolite with 2 and 4 h residence time at 250 °C and 2 h residence time at 350 °C. Accordingly, the ideal CO_2/N_2 selectivity (the ratio of CO_2 and N_2 adsorbed capacity) increased significantly from 19 (uncoated 5A) to 43 (5A-MLD-350-2h), 57 (5A-MLD-250-4h), and 77 (5A-MLD-250-2h) (Figure 4.5c). To understand the adsorption selectivity increase, we also studied the pore size distributions of 5A zeolite and MLD coated 5A composite sorbents after calcined under different conditions by argon sorption measurements. The argon sorption

isotherms for 5A, 5A-MLD-250-2h, 5A-MLD-250-8h and 5A-MLD-350-2h were presented in Figure 4.6a, 4.6c, 4.6e and 4.6g. The isotherms showed rapid argon uptake at low relative pressure, which was expected for the microporous zeolite materials. The pore size distribution was calculated by HK (Horvath-Kawazoe) method and shown in Figure 4.6b, 4.6d, 4.6f and 4.6h; the sharp peak at around 0.53 nm was assigned to 5A zeolite, and the pore diameter of MLD coatings after organic removal were estimated to be around 0.80 nm. Moreover, the pore diameter of MLD coating does not vary by changing the calcination condition. Therefore, we speculate the improved CO_2/N_2 selectivity can be attributed to the different extent of pore misalignment occurred at the interface between MLD coating and 5A zeolite surface under different calcination strategies.

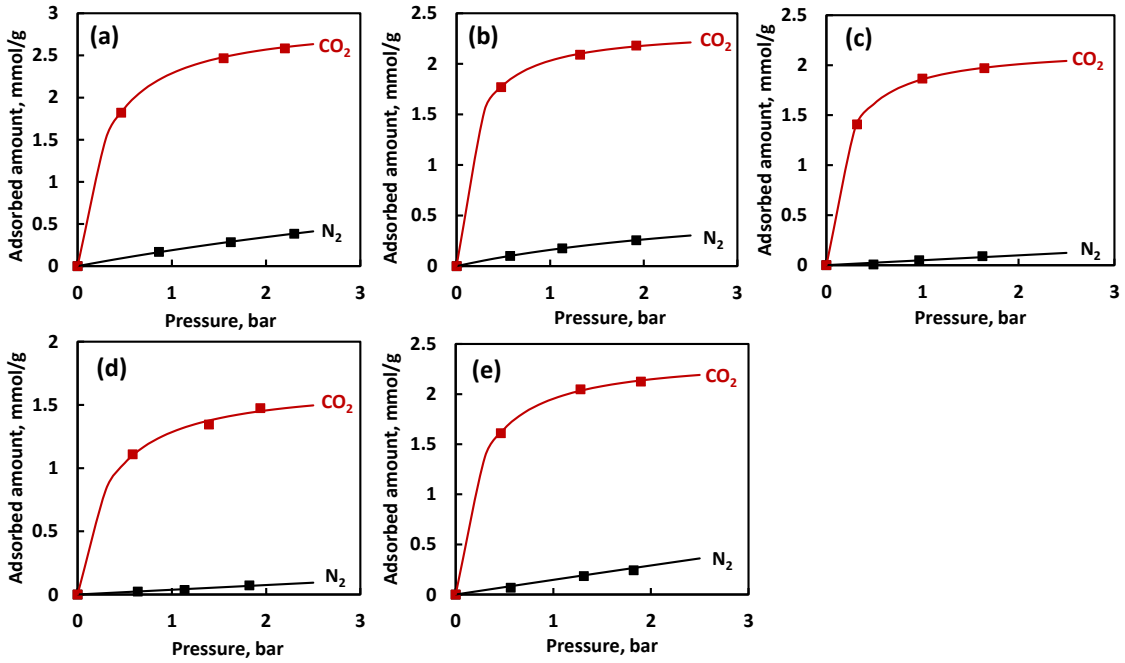

Figure 4.3. Experimental adsorption isotherms for CO_2 and N_2 on 5A zeolite (a), and MLD coated 5A zeolite calcined at 250 ^oC for different time, 5A-MLD-250-1min (b), 5A-MLD-250-2h (c), 5A-MLD-250-4h (d), and 5A-MLD-250-8h (e).

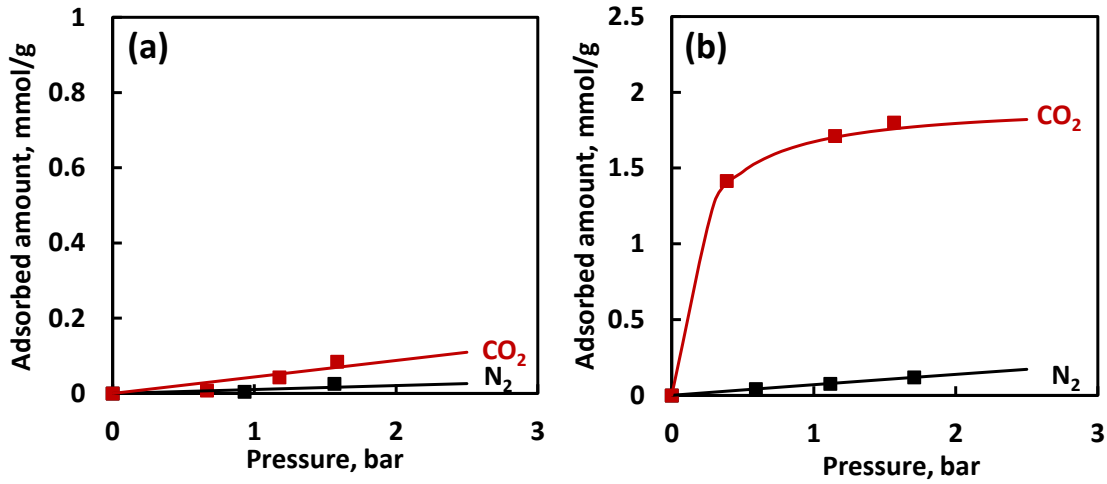

Figure 4.4. Experimental adsorption isotherms for CO_2 and N_2 on MLD coated 5A zeolite calcined at different temperature, 5A-MLD-200-2h (a), and 5A-MLD-350-2h (b).

To further confirm the adsorptive separation performance of MLD coated zeolite sorbents can be modified by controlling the calcination, MLD coatings were also deposited on 13X zeolite. CO_2 and N_2 adsorption isotherms on 13X with and without MLD coating and after calcination at 250 ^oC for different residence times were measured in a pressure range of 0-1 bar. 13X zeolite has a higher capacity of both CO_2 (3.28 mmol/g at 0.5 bar) and N_2 (0.21 mmol/g at 0.5 bar) compared with 5A zeolite as shown in Figure 4.7a. Compared with 2 h (Figure 4.7b) and 8 h (Figure 4.7d) residence time, 13X-MLD-250-4h (4 h residence time, Figure 4.7c) showed the lowest N_2 adsorption loadings, around 0.033 mmol/g at 0.5 bar. Meanwhile, the CO_2 adsorption loading was still as high as 2.32 mmol/g at the same pressure, resulting a higher CO_2/N_2 adsorptive selectivity as shown in Figure 4.7e. We made a comparison of our MLD coated zeolite sorbents with other representative porous materials, including zeolites, metal organic framework (MOF), aluminophosphates (AlPO), and zeolitic imidazolate framework (ZIF), for CO_2/N_2 adsorptive separation, as shown in Figure 4.8. The selectivity of CO_2/N_2 has been improved remarkably, especially

for 13X-MLD-250-2h (selectivity: 70) and 5A-MLD-25-2h (selectivity: 77), whereas the CO_2 adsorption capacity is still comparable and/or superior to most of the porous sorbents. Since microporous TiO_2 coatings can be deposited in 13X zeolite pores due to the smaller size of precursors of MLD than zeolite pores, the mechanism of enhanced CO_2/N_2 selectivity apparently may not be pore misalignment. Our speculation is TiO_2 coating may effectively wrap/deposit on strong adsorption sites, such as cations and acid sites, and thus weaken N_2 adsorption more than CO_2 adsorption. More study is under way to understand this behavior.

4.5 CONCLUSION

In conclusion, by varying the calcination conditions, we prepared novel MLD coated zeolites composite sorbents with greatly imoproved CO_2/N_2 selectivity while maintaining high CO_2 adsorption capacity. Specifically, our sorbents showed a CO_2/N_2 selectivity as high as 43-77 and CO_2 adsorption capacity 1.04-2.32 mmol/g at 0.5 bar and room temperature. Their separation performance is superior to most of the reported sorbents for CO_2 capture. Moreover, it has also been proved that MLD modification may be a very promising for zeolite modification for highly effective CO_2 capture.

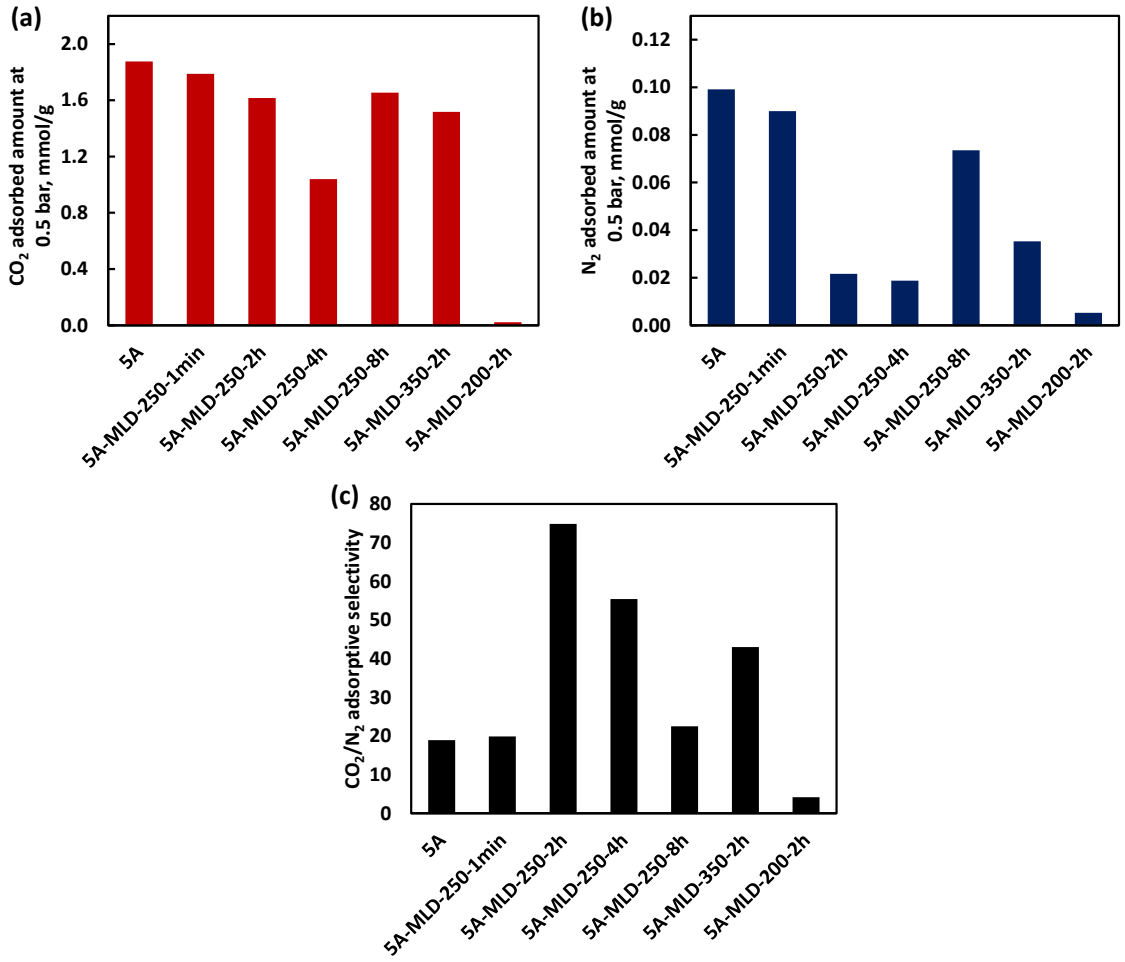

Figure 4.5. CO_2 adsorptive capacity at 0.5 bar on 5A and MLD coated 5A zeolite calcined at different conditions (a), N_2 adsorptive capacity at 0.5 bar on 5A and MLD coated 5A zeolite calcined at different conditions (b), CO_2/N_2 adsorptive selectivity at 0.5 bar on 5A and MLD coated 5A zeolite calcined at different conditions (c).

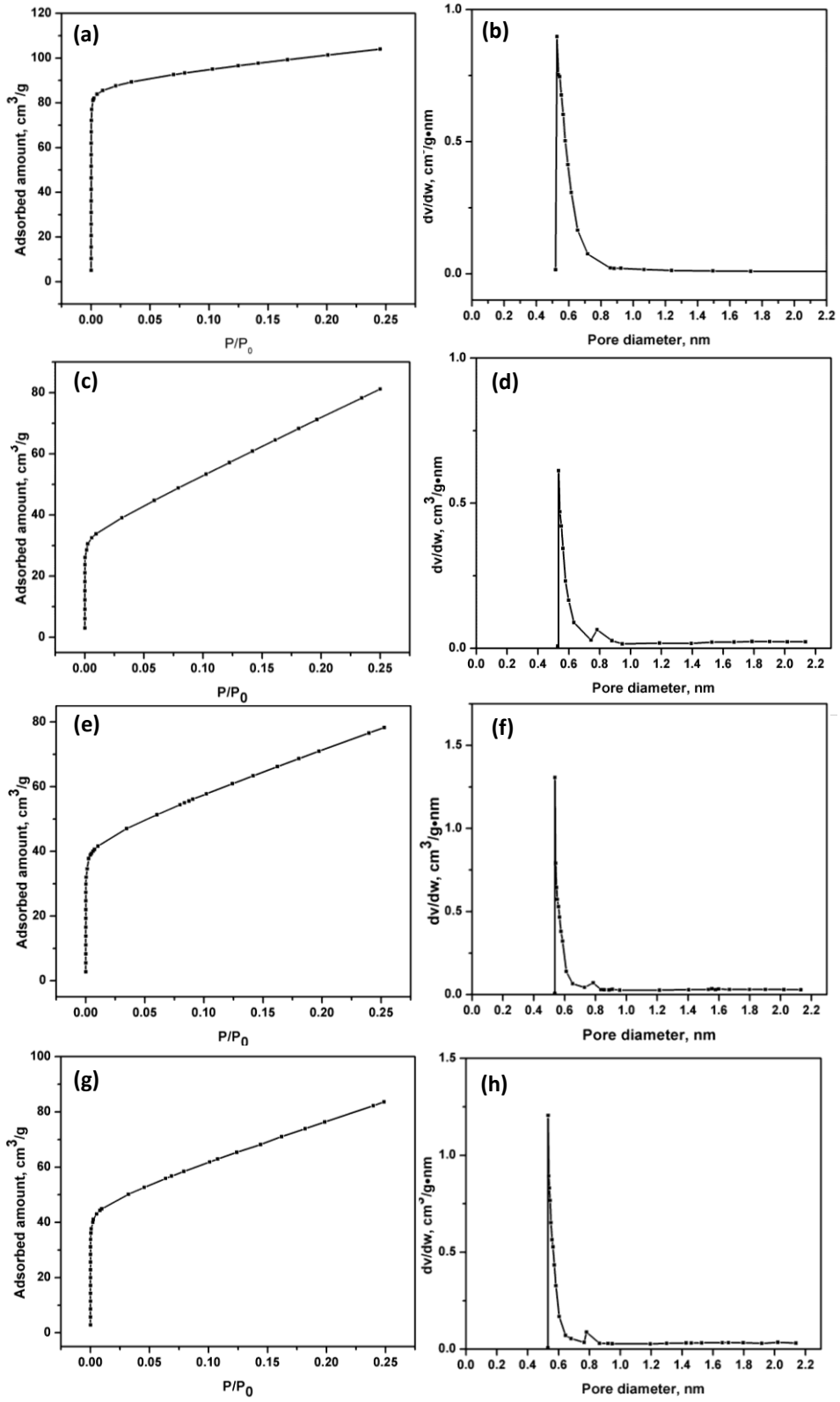

Figure 4.6. Argon adsorption isotherms measured at -196 ºC and pore size distributions for 5A (a, b), 5A-MLD-250-2h (c, d), 5A-MLD-250-8h (e, f) and 5A-MLD-350-2h (g, h).

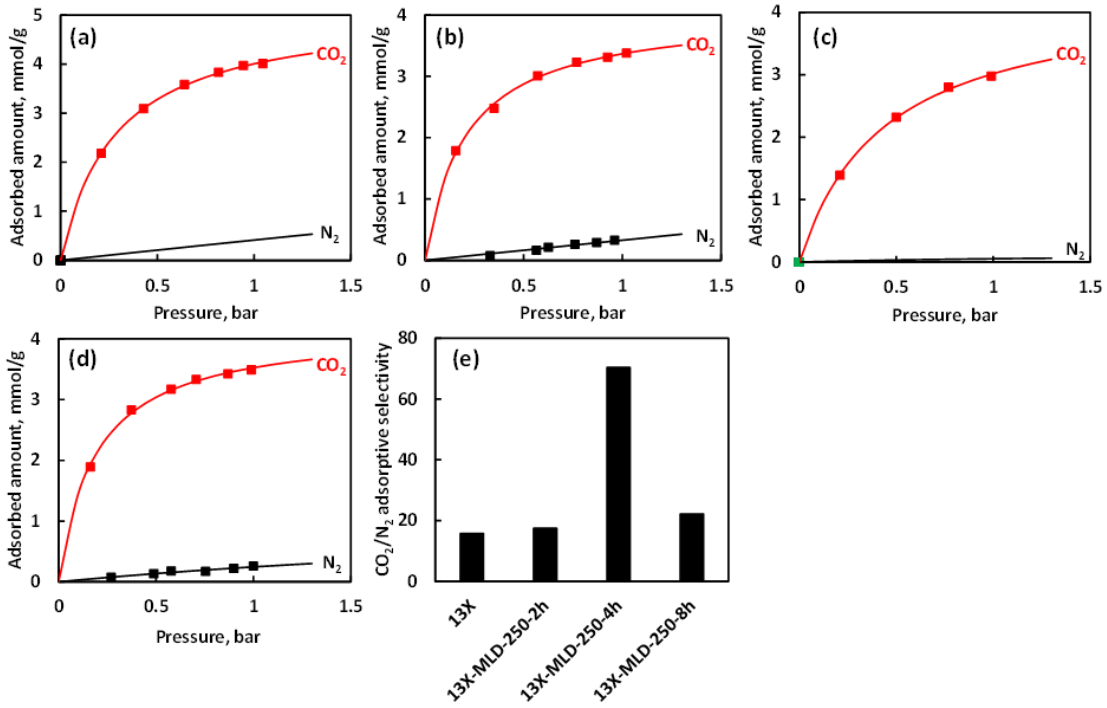

Figure 4.7. Adsorption isotherms of CO_2 and N_2 on 13X zeolite (a), and MLD coated 13X zeolite calcined at 250 °C for different time: 13X-MLD-250-2h (b), 13X-MLD-250-4h (c), 13X-MLD-250-8h (d), and CO_2/N_2 adsorptive selectivity at 0.5 bar on 13X zeolite and MLD coated 13X calcined at different conditions (e).

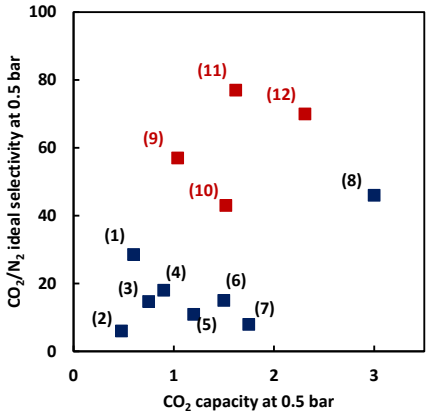

No.	Symbol	Material	Temperature, °C	Reference
(1)	■	Amine modified β-zeolite	30	(15)
(2)	■	MOF-177	20	(35)
(3)	■	$AlPO_4$-18	20	(36)
(4)	■	ZIF-68	25	(37)
(5)	■	HZSM-5	40	(38)
(6)	■	Carbon molecular sieve	25	(39)
(7)	■	Activated carbon	25	(40)
(8)	■	Bio-MOF-11	25	(41)
(9)	■	5A-MLD-250-4h	25	(this work)
(10)	■	5A-MLD-350-2h	25	
(11)	■	5A-MLD-250-2h	25	
(12)	■	13X-MLD-250-4h	25	

Figure 4.8. Comparison of MLD coated zeolite composite sorbents with porous adsorbents for CO_2/N_2 separation: CO_2/N_2 selectivity versus CO_2 adsorption capacity at 0.5 bar. Blue squares (1-8) represent porous adsorbents from the literatures [15, 35-41]; red squares (9-12) indicate MLD coated zeolite composite sorbents from this study.

4.6 REFERENCES

[1] G.P. Robertson, E.A. Paul, R.R. Harwood, Greenhouse gases in intensive agriculture: contributions of individual gases to the radiative forcing of the atmosphere, Science 289 (2000) 1922-1925.
[2] T.L. Root, J.T. Price, K.R. Hall, S.H. Schneider, C. Rosenzweig, J.A. Pounds, Fingerprints of global warming on wild animals and plants, Nature 421 (2003) 57-60.
[3] I.P.O.C. Change, Climate change 2007: the physical science basis, Agenda 6 (2007) 333.
[4] A. Yamasaki, An overview of CO2 mitigation options for global warming-Emphasizing CO2 sequestration options, Journal of Chemical Engineering of Japan 36 (2003) 361-375.
[5] N.C. Su, D.T. Sun, C.M. Beavers, D.K. Britt, W.L. Queen, J.J. Urban, Enhanced permeation arising from dual transport pathways in hybrid polymer-MOF membranes, Energy & Environmental Science (2016).
[6] A.L. Chaffee, G.P. Knowles, Z. Liang, J. Zhang, P. Xiao, P.A. Webley, CO 2 capture by adsorption: materials and process development, International journal of greenhouse gas control 1 (2007) 11-18.
[7] C.-T. Chou, C.-Y. Chen, Carbon dioxide recovery by vacuum swing adsorption, Sep. Purif. Technol. 39 (2004) 51-65.
[8] J.D. Figueroa, T. Fout, S. Plasynski, H. McIlvried, R.D. Srivastava, Advances in CO 2 capture technology—the US Department of Energy's Carbon Sequestration Program, International journal of greenhouse gas control 2 (2008) 9-20.
[9] Q. Zhang, R. Turton, D. Bhattacharyya, Development of Model and Model Predictive Control of a MEA-based Post-Combustion CO2 Capture Process, Ind. Eng. Chem. Res. (2016).
[10] S.A. Didas, S. Choi, W. Chaikittisilp, C.W. Jones, Amine–Oxide Hybrid Materials for CO2 Capture from Ambient Air, Accounts of chemical research 48 (2015) 2680-2687.
[11] C.-T. Chou, C.-Y. Chen, Carbon dioxide recovery by vacuum swing adsorption, Sep. Purif. Technol. 39 (2004) 51-65.
[12] A.S. Bhown, B.C. Freeman, Analysis and Status of Post-Combustion Carbon Dioxide Capture Technologies, Environ. Sci. Technol. 45 (2011) 8624-8632.
[13] S. Han, Y. Huang, T. Watanabe, S. Nair, K.S. Walton, D.S. Sholl, J.C. Meredith, MOF stability and gas adsorption as a function of exposure to water, humid air, SO 2, and NO 2, Microporous Mesoporous Mat. 173 (2013) 86-91.
[14] K. Sumida, D.L. Rogow, J.A. Mason, T.M. McDonald, E.D. Bloch, Z.R. Herm, T.-H. Bae, J.R. Long, Carbon dioxide capture in metal–organic frameworks, Chem. Rev. 112 (2011) 724-781.
[15] X. Xu, X. Zhao, L. Sun, X. Liu, Adsorption separation of carbon dioxide, methane and nitrogen on monoethanol amine modified β-zeolite, Journal of Natural Gas Chemistry 18 (2009) 167-172.
[16] X. Xu, X. Zhao, L. Sun, X. Liu, Adsorption separation of carbon dioxide, methane, and nitrogen on Hβ and Na-exchanged β-zeolite, Journal of Natural Gas Chemistry 17 (2008) 391-396.
[17] C.Y. Lee, Y.-S. Bae, N.C. Jeong, O.K. Farha, A.A. Sarjeant, C.L. Stern, P. Nickias, R.Q. Snurr, J.T. Hupp, S.T. Nguyen, Kinetic Separation of Propene and Propane in

Metal−Organic Frameworks: Controlling Diffusion Rates in Plate-Shaped Crystals via Tuning of Pore Apertures and Crystallite Aspect Ratios, J. Am. Chem. Soc. 133 (2011) 5228-5231.
[18] K. Morishige, Adsorption and Separation of CO2/CH4 on Amorphous Silica Molecular Sieve, The Journal of Physical Chemistry C 115 (2011) 9713-9718.
[19] H. Jasuja, J. Zang, D.S. Sholl, K.S. Walton, Rational Tuning of Water Vapor and CO2 Adsorption in Highly Stable Zr-Based MOFs, The Journal of Physical Chemistry C 116 (2012) 23526-23532.
[20] C.A. Grande, Advances in Pressure Swing Adsorption for Gas Separation, ISRN Chemical Engineering 2012 (2012) 13.
[21] S. Choi, J.H. Drese, C.W. Jones, Adsorbent materials for carbon dioxide capture from large anthropogenic point sources, ChemSusChem 2 (2009) 796-854.
[22] J. Merel, M. Clausse, F. Meunier, Experimental Investigation on CO2 Post−Combustion Capture by Indirect Thermal Swing Adsorption Using 13X and 5A Zeolites, Ind. Eng. Chem. Res. 47 (2008) 209-215.
[23] K. Chue, J. Kim, Y. Yoo, S. Cho, R. Yang, Comparison of activated carbon and zeolite 13X for CO2 recovery from flue gas by pressure swing adsorption, Ind. Eng. Chem. Res. 34 (1995) 591-598.
[24] J. Merel, M. Clausse, F. Meunier, Carbon dioxide capture by indirect thermal swing adsorption using 13X zeolite, Environmental progress 25 (2006) 327-333.
[25] Z.N. Song, Y. Huang, L. Wang, S.G. Li, M. Yu, Composite 5A zeolite with ultrathin porous TiO2 coating for selective gas adsorption, Chem. Commun. 51 (2015) 373-375.
[26] Z.N. Song, Y. Huang, W.W. Xu, L. Wang, Y. Bao, S.G. Li, M. Yu, Continuously Adjustable, Molecular-Sieving “Gate” on 5A Zeolite for Distinguishing Small Organic Molecules by Size, Sci. Rep. 5, 13981 (2015).
[27] S.A. Nassar, V.L. Virupaksha, Effect of adhesive thickness and properties on the biaxial Interfacial shear stresses in bonded joints using a continuum mixture model, J. Eng. Mater. Technol. 131 (2009) 9.
[28] H.-H. Pan, J.-C. Li, T.-C. Hou, K.-S. Liao, EFFECT OF TEMPERATURE TO MICRO-DISPLACEMENT OF INTERFACIAL TRANSITION ZONE IN CEMENTITIOUS MATERIALS BY ESPI MEASUREMENT.
[29] D.W. Breck, W.G. Eversole, R.M. Milton, T.B. Reed, T.L. Thomas, CRYSTALLINE ZEOLITES .1. THE PROPERTIES OF A NEW SYNTHETIC ZEOLITE, TYPE-A, J. Am. Chem. Soc. 78 (1956) 5963-5971.
[30] D.R. Baer, M.H. Engelhard, G.E. Johnson, J. Laskin, J. Lai, K. Mueller, P. Munusamy, S. Thevuthasan, H. Wang, N. Washton, Surface characterization of nanomaterials and nanoparticles: Important needs andchallenging opportunities, J. Vac. Sci. Technol. A 31 (2013) 050820.
[31] M. Janek, K. Emmerich, S. Heissler, R. Nüesch, Thermally induced grafting reactions of ethylene glycol and glycerol intercalates of kaolinite, Chem. Mat. 19 (2007) 684-693.
[32] A.A. Dameron, D. Seghete, B. Burton, S. Davidson, A. Cavanagh, J. Bertrand, S. George, Molecular layer deposition of alucone polymer films using trimethylaluminum and ethylene glycol, Chem. Mat. 20 (2008) 3315-3326.
[33] M. Che, G.C. Bond, Adsorption and catalysis on oxide surfaces, Elsevier, 1985.

[34] Y. Wang, M.D. LeVan, Adsorption equilibrium of carbon dioxide and water vapor on zeolites 5A and 13X and silica gel: pure components, Journal of Chemical & Engineering Data 54 (2009) 2839-2844.
[35] J.A. Mason, K. Sumida, Z.R. Herm, R. Krishna, J.R. Long, Evaluating metal-organic frameworks for post-combustion carbon dioxide capture via temperature swing adsorption, Energy & Environmental Science 4 (2011) 3030-3040.
[36] Q. Liu, N.C.O. Cheung, A.E. Garcia-Bennett, N. Hedin, Aluminophosphates for CO2 separation, ChemSusChem 4 (2011) 91-97.
[37] B. Liu, B. Smit, Molecular simulation studies of separation of CO2/N2, CO2/CH4, and CH4/N2 by ZIFs, The Journal of Physical Chemistry C 114 (2010) 8515-8522.
[38] P. Harlick, F. Tezel, Adsorption of carbon dioxide, methane, and nitrogen: pure and binary mixture adsorption by ZSM-5 with SiO2/Al2O3 ratio of 30, Sep. Sci. Technol. 37 (2002) 33-60.
[39] E. Kikkinides, R. Yang, S. Cho, Concentration and recovery of carbon dioxide from flue gas by pressure swing adsorption, Ind. Eng. Chem. Res. 32 (1993) 2714-2720.
[40] B.-K. Na, K.-K. Koo, H.-M. Eum, H. Lee, H.K. Song, CO2 recovery from flue gas by PSA process using activated carbon, Korean Journal of Chemical Engineering 18 (2001) 220-227.
[41] J. An, S.J. Geib, N.L. Rosi, High and selective CO2 uptake in a cobalt adeninate metal− organic framework exhibiting pyrimidine-and amino-decorated pores, J. Am. Chem. Soc. 132 (2009) 38-39.

CHAPTER 5:

TiO_2 NANOFILTRATION MEMBRANES PREPARED BY MOLECULAR LAYER DEPOSITION FOR WATER PURIFICATION

5.1 ABSTRACT

In this study, molecular layer deposition (MLD) was used as a novel and highly controllable method to prepare TiO_2 nanofiltration membranes with approximately 1 nm pores for water purification. Number of deposition cycles and precursors ($TiCl_4$ and ethylene glycol) were used to control membrane quality and final pore sizes, respectively. Optimized TiO_2 nanofiltration membranes had a pure water permeability as high as ~48 $L/(m^2 \cdot h \cdot bar)$. Salt and dye rejection measurements showed moderate rejection of Na_2SO_4 (43%) and $MgSO_4$ (35%) and high rejection of methylene blue (~96%). In addition, natural organic matter (NOM) removal testing showed high rejection (~99%) as well as significantly improved antifouling performance and recovery capability. MLD, as a new TiO_2 nanofiltration membrane preparation technique, has great potential to realize excellent control of membrane composition, thickness, and potentially pore sizes in a scalable way.

Keywords: Membranes; Nanofiltration; TiO_2; Molecular layer deposition

5.2 INTRODUCTION

Water scarcity is one of the most serious global issues because of the growing freshwater use and depletion of usable fresh water resources.[1] It is, therefore, in a great need to develop various energy-efficient water treatment technologies to realize water purification for different water sources and at different levels. Nanofiltration membranes are now widely used in drinking water and wastewater treatment, as well as pretreatment for desalination because of their ability to remove viruses, hardness, dissolved organic matter, and salts, especially multivalent ions.[2-5] Currently, polymers, such as cellulose acetate, polyamide, polyimide, and poly(ether)sulfone, are dominant materials in nanofiltration.[4, 6] Most of the polymeric nanofiltration membranes have advantages of flexibility, simple preparation process, and relatively low cost.[2] Compared with polymeric nanofiltration membranes, ceramic nanofiltration membranes, usually manufactured from Al_2O_3, ZrO_2, and TiO_2,[7] have better chemical, thermal and mechanical stability and long lifetime, and thus may be used in applications under extreme operating conditions.[2] Ceramic nanofiltration membranes are usually prepared by solution-based sol-gel method,[8-12] which needs careful control of the deposition process to produce high quality membranes. Typically, in this process, a gel needs to be carefully prepared from a colloidal or polymeric solution by adding organic additives to control the hydrolysis and condensation of alkoxides.[10, 13] In addition, membrane thickness cannot be precisely controlled at the sub-nanometer scale. This may severely limit sol-gel method for preparing ultrathin, high flux nanofiltration membranes. More importantly, pore sizes of ceramic nanofiltration membranes, prepared by the sol-gel method, are difficult to be precisely controlled at about 1 nm, especially for stable metal oxides, such as TiO_2.

Attempts to prepare TiO_2 nanofiltration membranes started from 1990s, and the average pore sizes obtained in these studies were in the range of 1.5~4.0 nm.[8-11, 13-16] To date, the tightest reported TiO_2 nanofiltration membranes, prepared by optimizing the sol-gel processing conditions, had a pore size of ~0.9 nm.[12, 13] Hydrolysis conditions of titanium alkoxides, however, need to be strictly controlled because of the extremely fast hydrolysis rate to avoid any local excess of water at any moment.[12]

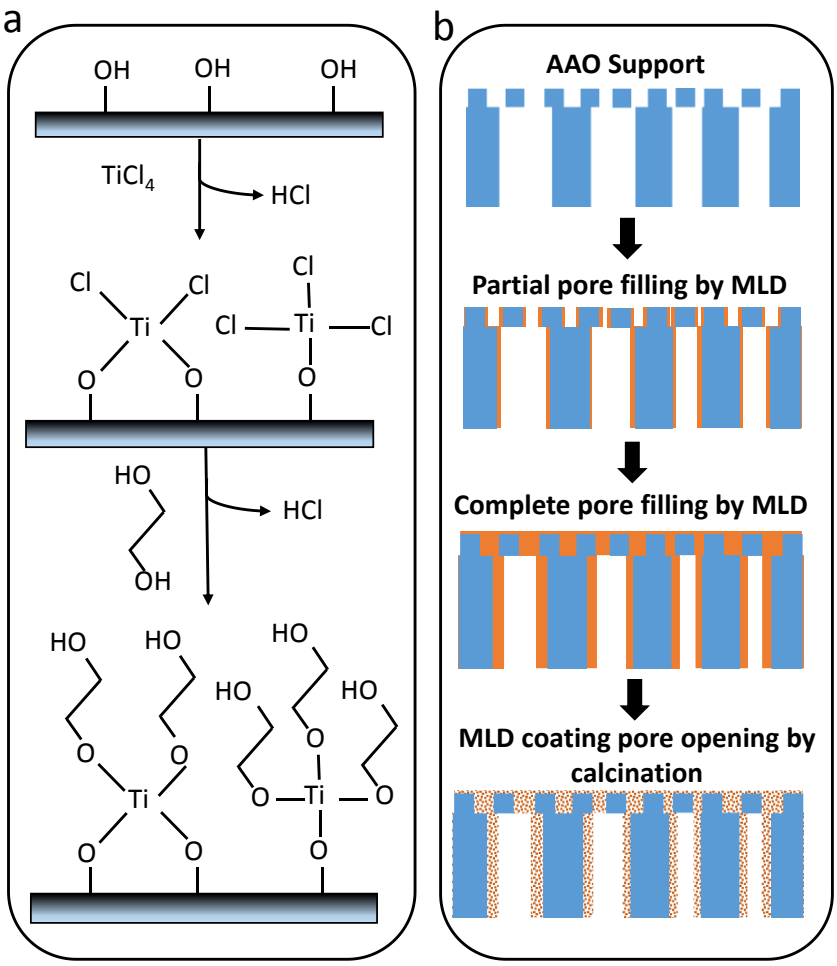

Figure 5.1. Schematic diagrams of MLD surface reactions for titanium alkoxide coating growth using $TiCl_4$ and EG as precursors (a) and a step-by-step procedure to prepare the TiO_2 nanofiltration membrane using an AAO support by MLD and subsequent calcination to open pores (b).

Molecular layer deposition (MLD), a gas phase deposition technique, is a subset of atomic layer deposition (ALD) and has been developed very recently.[17, 18] Similar to ALD, in MLD, two self-limiting surface reactions are conducted alternately to deposit organic-inorganic hybrid coatings on a substrate. During each surface reaction, precursor molecules react with surface reactive groups, such as -OH, and chemically bond a layer of precursor molecules on the surface; new reactive sites/functional groups on the linked precursor molecules will be utilized for further layer growth.[19] Compared with the dense inorganic coatings prepared by ALD, MLD growth has been demonstrated for a variety of organic-inorganic hybrid coatings by using suitable metal and organic precursors.[20] The obtained organic-inorganic hybrid coatings can subsequently be converted into porous coatings by removing the organic compound [18, 21, 22]. The potential of using ALD technique to reduce pore size of porous support has been investigated by several research groups.[23-26] However, it is difficult to precisely control the resulting pore size at nanometer level. This resulted from the unavoidable pore size distribution of the porous support, and smaller pores were completely sealed first, leaving the larger pores still open. Transport resistance was also expected to increase dramatically, because of the deposited dense coating by ALD. Molecular layer deposition has already been used to deposit ultra-thin porous coatings for metal catalysts stabilization[27] and highly selective catalysts.[28] Very recently, we have shown that forming an ultrathin, microporous MLD coating on 5A zeolite external surface greatly improved its size-selective adsorption via appropriate pore misalignment at the interface of the MLD coating and zeolite[21, 22]. Various microporous materials, such as Al_2O_3, SiO_2, and TiO_2, can be deposited by MLD technique. One reason we chose TiO_2 as the coating materials in this study is that TiO_2 has been considered as a

more stable material, especially its water stability[12, 29]. Figure 5.1a illustrates two surface reactions in one cycle of MLD using $TiCl_4$ and ethylene glycol (EG) as precursors to deposit titanium alkoxide coating. The self-limiting nature of the surface reactions of MLD offers advantages of exquisite control over coating thickness at sub-nanometer level, conformal pinhole-free coatings on high aspect ratio structures, and scale-up capability.[30-32] Here, we report an innovative use of MLD to fabricate TiO_2 nanofiltration membranes by depositing microporous TiO_2 coating on mesoporous support with excellent control of coating quality, thickness and nanometer-sized membrane pores, and their potential for water purification. We expect MLD will become a new method for preparing TiO_2 nanofiltration membranes with well controlled thickness, composition, and membrane pore sizes in a scalable way.

5.3 EXPERIMENTAL METHODS

5.3.1 MOLECULAR LAYER DEPOSITION PROCESS

Titanium alkoxide MLD coatings were deposited using titanium tetrachloride ($TiCl_4$; 99.9%, Sigma Aldrich) and ethylene glycol ($C_2H_6O_2$; 99%, Alfa Aesar) as precursors. The MLD coating process was carried out in a tubular reactor, as shown in Fig. 5.2. A LabVIEW software was used for programmed control of pneumatic valves for transient dosing. Each MLD cycle started with 240 sec vacuum. $TiCl_4$ was then gradually introduced into the reactor as a vapor, based on the driving force of its room-temperature vapor pressure, until a pressure of 20 Pa and settled for 120 sec to allow the surface reaction; 240 sec vacuum was followed to evacuate extra unreacted $TiCl_4$. Ultrahigh purity N_2 (Airgas) was used to purge the reactor with a flow rate of 20 sccm (standard cubic

centimeters per minute) for 30 sec controlled by a mass-flow controller (Aera FC-7800) to further clean the reactor. Then, 240 sec vacuum was applied to evacuate N_2. The above operation was repeated except that $TiCl_4$ was replaced by ethylene glycol (EG) at 6.7 Pa. A typical coating cycle consisted of the following sequence: evacuation, $TiCl_4$ dose, evacuation, N_2 purge, evacuation; EG dose, evacuation, N_2 purge, evacuation. The MLD reactor was wrapped by a heating tape covered by a thermal insulation tape. All MLD processes were conducted at 100°C controlled by a homemade temperature controller.

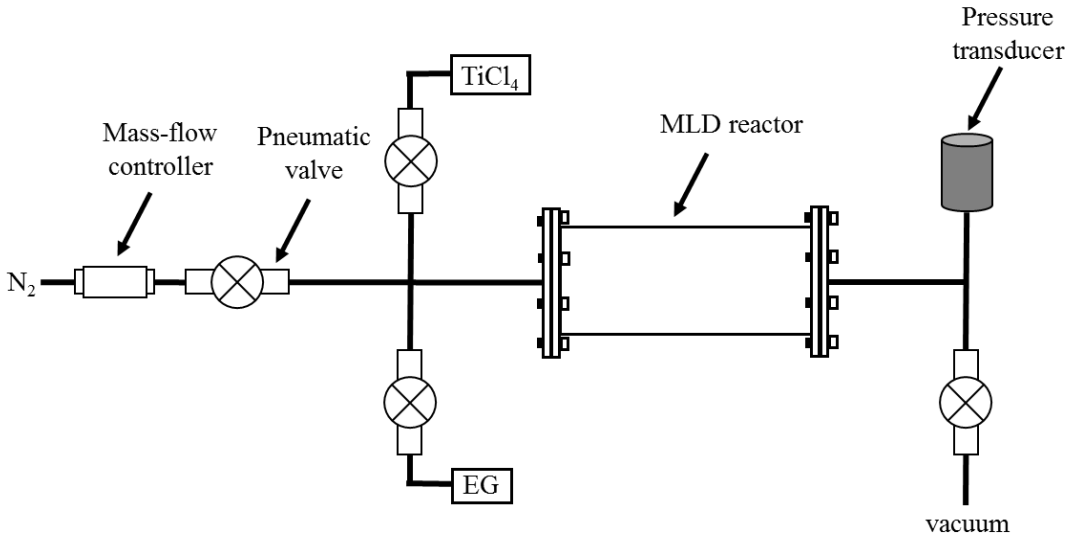

Figure 5.2. Schematic illustration of the deposition system used for molecular layer deposition.

5.3.2 MEMBRANES PREPARATION

Proposed MLD membrane forming process was shown schematically in Fig.51b. We used flat anodic aluminum oxide (AAO) membranes (Whatman) as the starting model support. These AAO membranes have an asymmetric structure with a diameter of 47 mm. The main body of AAO membranes is composed of large pores, ~100 nm, with ~60 μm thickness. The top selective layer has a thickness of approximately 300 nm and pore size

of ~20 nm. Before MLD, AAO membrane was outgassed under vacuum at 200°C for 1 h to remove adsorbed water. Different cycles of MLD were subsequently conducted to deposit titanium alkoxide coating in AAO support pores. After completely filling AAO pores by hybrid titanium alkoxide, microporous TiO_2 membrane was generated by removing organic compound in the dense hybrid coating by calcination in air in a muffle furnace at 250°C for 4 h with a heating and cooling rate of 1°C/min as reported before[21].

5.3.3 MEMBRANES CHARACTERIZATION

Field emission scanning electron microscopy (FESEM, Zeiss Ultra Plus) was used to observe the morphology of AAO before and after MLD. Surface roughness of AAO before and after MLD was measured using atomic force microscopy (AFM, AFMWorkshop). Surface chemical composition of AAO support and TiO_2 coated AAO was analyzed by X-ray photoelectron spectroscopy (XPS, Kratos Axis Ultra DLD instrument equipped with a monochromated Al Ka x-ray source and hemispherical analyzer capable of an energy resolution of 0.5 eV). N_2 adsorption isotherms at 77 K were measured using a Micromeritcs ASAP 2020 unit to determine pore size distribution of the MLD membrane. Prior to adsorption measurement, samples were ground to a fine powder and degassed in situ at 250°C for 4 h. Pore size distribution was calculated using adsorption branch of the isotherms. X-ray powder diffraction (XRD) measurements were carried out using a Rigaku MiniFlex II diffractometer with Cu Kα radiation (λ = 0.15418 nm). Diffraction data were recorded for 2θ angles between 5° and 50°.

5.3.4 MEMBRANE PERMEATION TESTS

Liquid permeation was conducted using a dead end, stirred cell filtration system (Sterlitech Corp.) with 300 mL total feed volume. Feed side was connected to a high-pressure nitrogen tank to control feed pressure in the range of 0-7 bar. A magnetic stir bar inside the tank was used to stir the feed liquid at a spinning rate of 1000 rpm to minimize concentration polarization. An electronic scale (Ohaus, CS Series) was used to measure mass of permeated liquid. DI water (pH: 5.3; conductivity: 0.86 μS) was used in all permeation measurements. Pressurized filtration of aqueous solutions of methylene blue (MB) (6.4 mg/L), NaCl (10 mM), Na_2SO_4 (10 mM), $MgCl_2$ (10 mM), and $MgSO_4$ (10 mM) was performed to evaluate water purification performance of the prepared TiO_2 nanofiltration membranes. All chemicals were obtained from Sigma-Aldrich, and no pH was adjusted in the prepared solutions. In each rejection test, liquid permeation was stabilized for 3 h before taking any measurement. Concentration of MB in the collected permeate was analyzed using a UV-vis spectrophotometer (Shimadzu UV-1800). Concentration of NaCl, Na_2SO_4, $MgCl_2$, and $MgSO_4$ was measured by a conductivity meter (Pour Grainger International, Lake Forest, IL, USA).

Suwannee River humic acid (SRHA) standard, as a model natural organic matter (NOM), was purchased from International Humic Substance Society (St. Paul, MN, USA) and used to evaluate anti-fouling performance of the TiO_2 nanofiltration membranes. Feed concentration SRHA in all filtration measurements was 5 mg/L. Permeate was collected at different water recoveries for flux and composition analysis. Concentration of SRHA was determined by UV-vis at a wavelength of 292 nm.

5.4 RESULTS AND DISCUSSION

5.4.1 TiO_2 NANOFILTRATION MEMBRANE CHARACTERIZATION

Surface morphology of the blank AAO support and gradual pore filling by TiO_2 MLD coating were observed by FESEM. The top surface view of the blank AAO support exhibited a porous structure consisting of 20-50 nm pores, the estimated porosity of AAO top selective layer is approximately 60%, as shown in Fig.5.3a. After 20 and 40 cycles of MLD on AAO support (AAO-20TiO_2 and AAO-40TiO_2; corresponding abbreviations for AAO with different cycles of MLD were used in the following description), the effective pore size of the AAO support gradually reduced (Fig.5.3b) due to the conformal TiO_2 MLD coating deposited on the pore wall as well as on the surface of the support. However, after 40 cycles of MLD coating, open pores were still visible. This is apparently because deposited MLD coating was not thick enough to completely fill support pores. Our previous work showed a TiO_2 MLD growth rate of ~0.42 nm/cycle at 100°C[21]. Therefore, only pores smaller than approximately 32 nm are expected to be completely filled after 40 cycles of MLD. Since pore size distribution (20-50 nm) of the AAO support (Fig. 5.3a) exists, pores larger than 32 nm were only partially filled after 40 cycles of MLD. When 60 cycles of MLD was applied, a dense, continuous coating was deposited on the AAO support free of visible defects (Fig. 5.3c), and higher magnification revealed a much thicker coating and complete filling of AAO pores (inset in Fig. 5.3c). Fig. 5.3d showed the cross-sectional view of the AAO-60TiO_2 membrane. The top AAO layer with 20-50 nm pores and a thickness of approximately 300 nm, which was supported on the bottom layer with larger pores of about 100 nm, has been completely filled with the TiO_2 MLD coating. Pressurized pure water permeation also confirmed that the MLD coating before

calcination was dense and impermeable to water, as discussed below. AFM showed that the AAO support had a roughness (Ra) of 24.5 nm (Fig. 5.4a). After depositing 60 cycles of TiO_2 MLD coating, the Ra value decreased to 8.69 nm (Fig. 5.4b). This decrease in the value of Ra is consistent with the fact that MLD has the advantage to deposit coatings with smooth morphologies[33]. XPS was used to detect the surface elements of the AAO and the AAO-60TiO_2 membrane. For bare AAO support, Fig.5.5a showed a substantial amount of aluminum on the top surface. After 60 cycles of MLD, aluminum in the AAO support can hardly been seen due to the shorter excited electron mean free path than the TiO_2 coating thickness. Our previous study showed the depth of analysis for an XPS measurement of TiO_2 porous coating is approximately 25 nm.[21] Fig. 5.5b shows two major peaks in AAO-60TiO_2 membrane, corresponding to Ti $2p_{3/2}$ and Ti $2p_{1/2}$, respectively. And, there was no Ti in the AAO support. Double sided tape was applied to glue AAO support and AAO-60TiO_2 membrane to the hollowed XRD sample holder to get rid of the background effect from XRD holder. In Fig. 5.6, a dash line was drawn at 2θ of 19º, which was assigned to the main peak of tape. Peak (2θ of 19º) intensity decreased when AAO was attached on the top of the tape due to the weakened X-ray (Fig. 5.6b). In Fig. 5.6c, the peak (2θ of 19º) intensity was even weakened for AAO-60TiO_2 (TiO_2 MLD coated AAO) membrane. In addition, a broad peak in the range of 20 to 25° was observed, which was ascribed to the amorphous TiO_2 [34]. The broad peaks near 2θ of 30º in Fig. 5.6b and 5.6c match that reported for amorphous AAO by Yang [35]. Figure 5.7 showed the pore size distribution of TiO_2 MLD coating after calcination at 250ºC, which was centered at approximately 1 nm. This is consistent with our previous work of TiO_2 MLD coated 5A zeolite composite adsorbents[21] and Patel's work on porous TiO_2 MLD

films[36]. Organic dye rejection was also measured to probe the effective pore size of TiO_2 nanofiltration membranes, as discussed below.

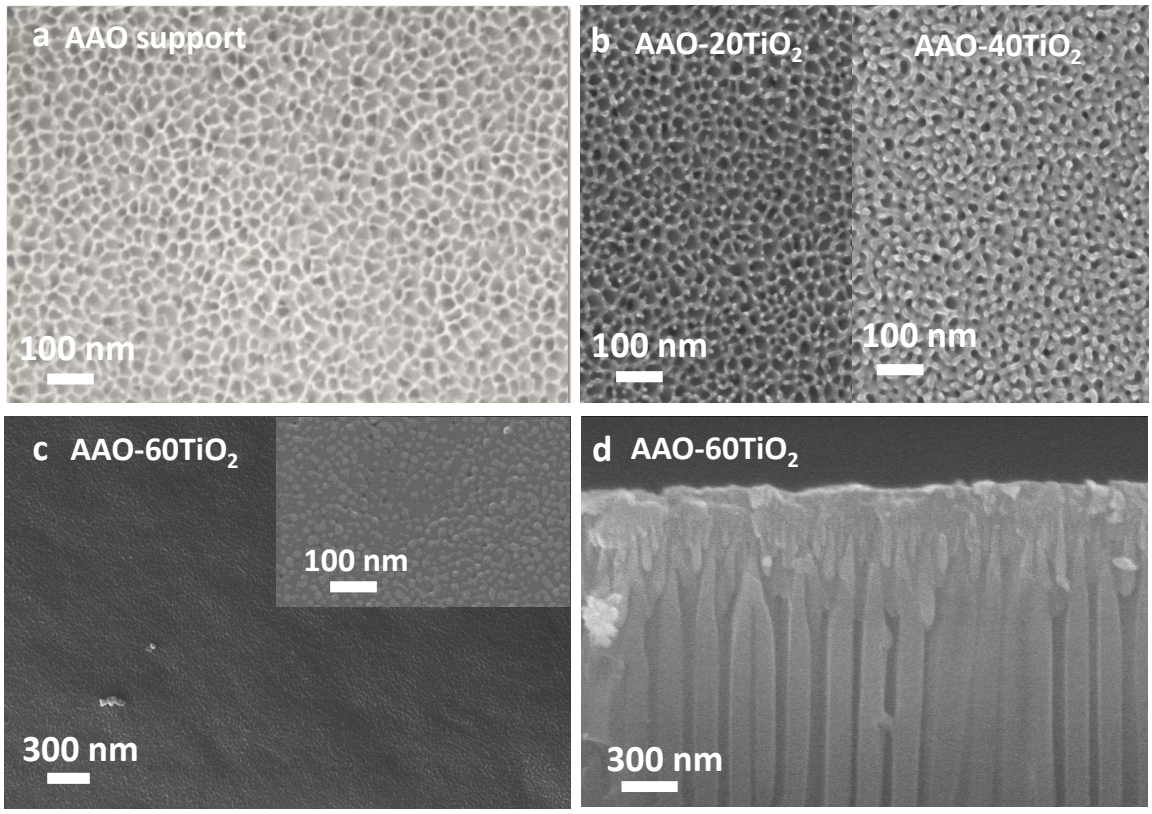

Figure 5.3. FESEM images of the top-surface of AAO support (a); AAO-20TiO_2 membrane (left) and AAO-40TiO_2 membrane (right) (b); AAO-60TiO_2 membrane (c) (the inset SEM image showed a higher magnification of AAO-60TiO_2 membrane); and cross-section of AAO-60TiO_2 membranes (d). All MLD coatings have been calcined at 250^{o}C in air.

5.4.2 EFFECT OF MLD CYCLES ON PURE WATER PERMEATION

Besides direct observation of the MLD coating on AAO support by FESEM, pressurized pure water permeation was also measured and used to determine number of MLD cycles that ensures a continuous, dense coating. Pure water permeability through AAO coated with different cycles of MLD was measured before and after calcination at

250°C. The permeability was calculated by the ratio of the volumetric filtrate flux (volume flow rate per membrane area) to the applied pressure. As shown in Fig. 5.8, before calcination, water permeability through bare AAO support (feed pressure: 1 bar) was 1520 L/(m^2·h·bar), and decreased to 595 and 195 L/(m^2·h·bar) after 20 (feed pressure: 2 bar) and 40 cycles of MLD (feed pressure: 4 bar), respectively. This is due to the gradual reduction of the AAO pores by the hybrid MLD coating deposited on the AAO pore walls. Apparently, after 40 cycles of MLD, the AAO support pores were still not completely filled. After 60 cycles of MLD, no observable water flux was found after 24 h permeation under pressure drop of 7 bar, corresponding to a pure water permeability lower than 0.1 L/(m^2·h·bar) (detection limit of our system). This suggests 60 cycles of MLD formed a defect-free, dense titanium alkoxide MLD coating on the AAO support. This is consistent with the SEM images of AAO-60TiO_2 in Fig.5.3c. After calcination in air at 250°C, a pure water permeability as high as 48 L/(m^2·h·bar) was obtained (feed pressure is 7 bar for all AAO-60TiO_2 and AAO-80TiO_2 membrane filtration test). This is in strong contrast with the low pure water permeability of commercial polymer membranes between 1-7 L/(m^2·h·bar)[37]. Further increasing MLD cycles to 80 also generated a defect-free, hybrid MLD coating with pure water permeability lower than our detection limit, and after calcination pure water permeability increased to 13 L/(m^2·h·bar). The decreased water permeability is apparently due to the thicker TiO_2 coating on AAO surface and thus increases transport resistance. It is interesting to find that the pure water permeabilty of calcined AAO-20TiO_2 membrane was even higher than calcined bare AAO support, although pores of AAO are expected to become narrower after MLD coating. This may be

attributed to the better stability of TiO_2 at elevated temperature[38]; alumina is much easier to dehydrate after thermal treatment, and thus its surface becomes less hydrophilic.

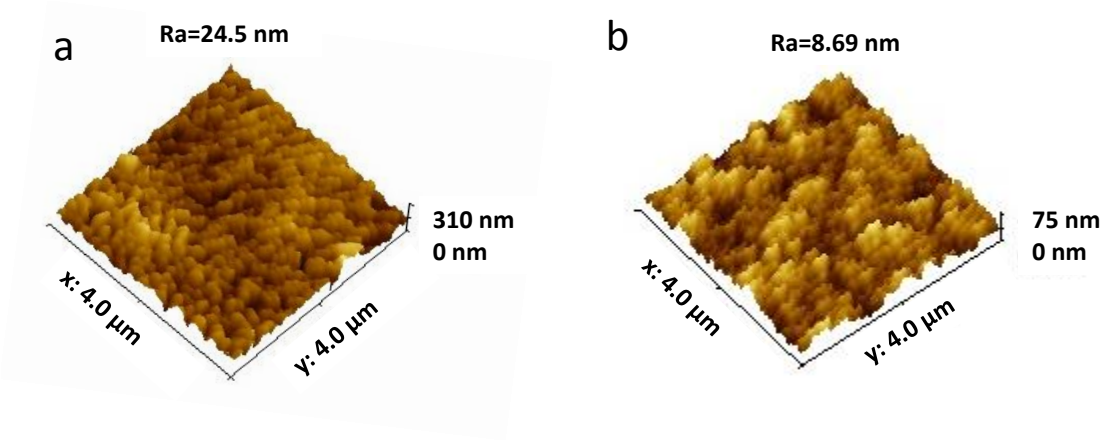

Figure 5.4. AFM images of the top-surface of bare AAO support (a) and AAO-60TiO_2 membrane (b).

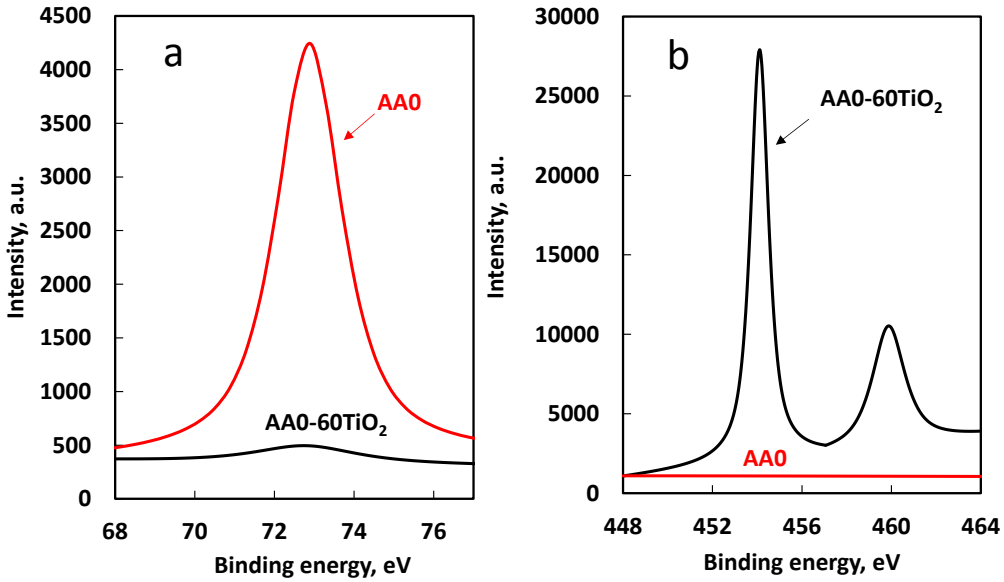

Figure 5.5. XPS spectra of AAO and AAO-60TiO_2 (after calcination): Al 2p (a) and Ti 2p (b).

5.4.3 WATER PURIFICATION BY TiO_2 NANOFILTRATION MEMBRANES

We first investigated water purification performance of the AAO-60TiO_2 nanofiltration membranes by measuring permeability and rejection for aqueous solutions of NaCl, Na_2SO_4, $MgCl_2$, and $MgSO_4$. AAO-60TiO_2 membrane showed permeabilities of

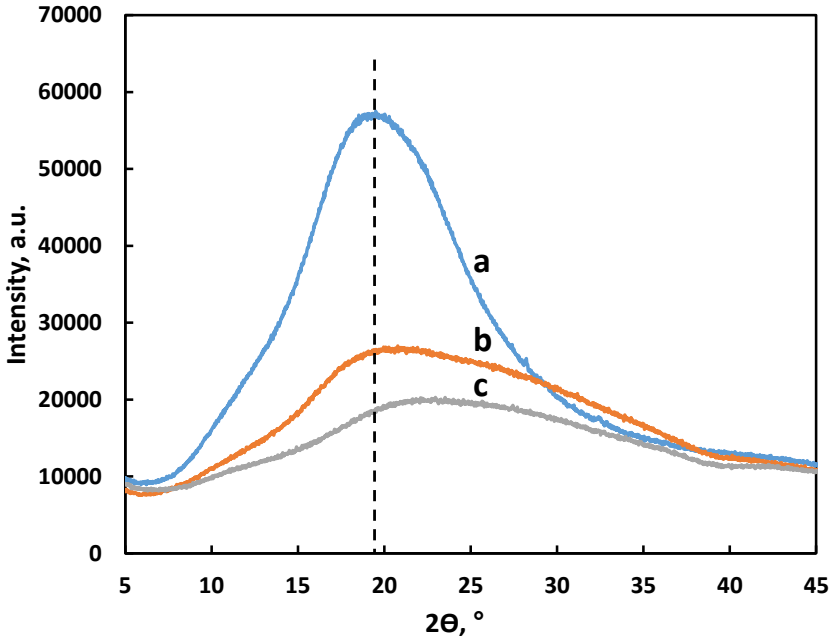

Figure 5.6. XRD patterns of double sided tapes (a), AAO support (b), and theAAO-60TiO_2 membrane (c).

7.2-10.5 L/(m^2·h·bar) for studied aqueous salt solutions (Fig. 5.9). The decline of permeability compared with pure water is probably because of the increased hydrodynamic resistance by ions adsorption in membranes, which was also observed in Tsuru's previous work[29]. For the salt rejection, decent rejection for Na_2SO_4, 43%, was observed, while moderate rejection (35%, 29%, and 24%) of $MgSO_4$, NaCl, and $MgCl_2$ was obtained, respectively, as shown in Fig.5.9. This observed order of salt rejection (Na_2SO_4 > $MgSO_4$

> NaCl > $MgCl_2$) can be ascribed to the Donnan exclusion[2, 39] for slightly negatively charged TiO_2 nanofiltration membranes[40]. According to Donnan exclusion theory, co-

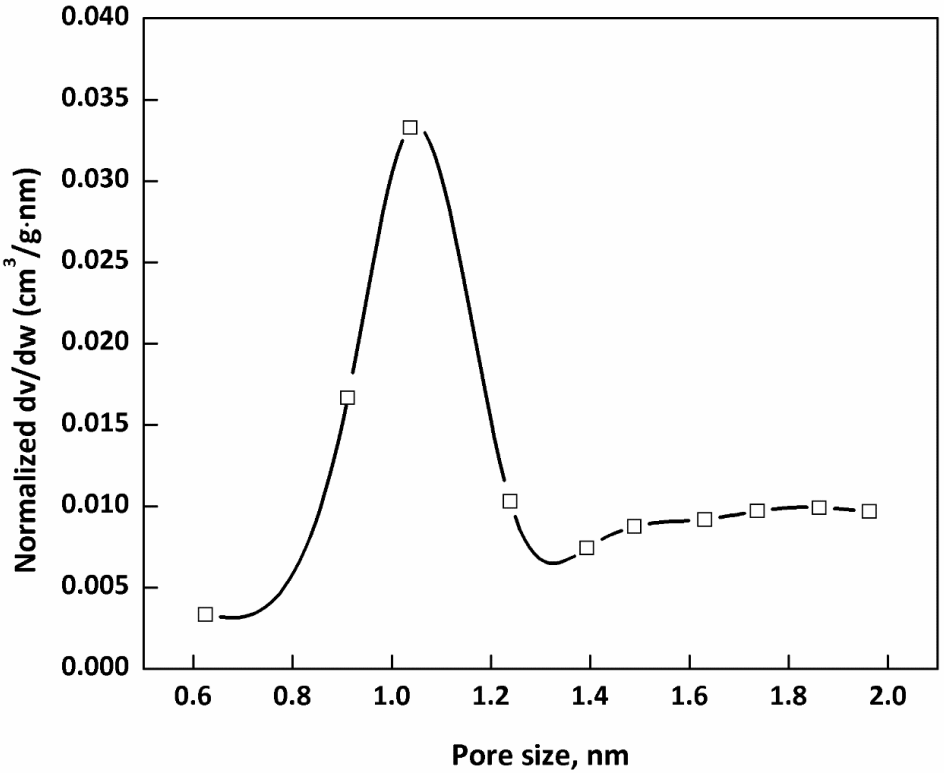

Figure 5.7. Pore size distribution of the AAO-60TiO_2 membrane.

ions, which have the same charge of membrane surface, tend to exclude from the membrane, and the repulsive force for divalent co-ions is greater than for monovalent co-ions. Counter-ion is also rejected in order to keep the electro-neutrality.[2] We also measured organic dye permeation, AAO-60TiO_2 membrane showed a high rejection (96%) for MB (cationic dye, MW = 373.90 $gmol^{-1}$) after 3 h filtration; much longer time permeation only slightly decreased its rejection (93% after 18 h). The high rejection of rigid dye could be mainly attributed to sieving by membrane pores.[41] But, the MB permeability was only ~3.3 L/(m^2·h·bar) (Fig. 5.9). We speculate the low permeability

during MB filtration might be because the size of MB (0.7 × 1.6 nm)[42] is comparable to the pore size of AAO-60TiO_2 nanofiltration membrane (~1 nm) and thus blocked membrane pores. Bare AAO support did not show rejection of the organic dye and salt solutions.

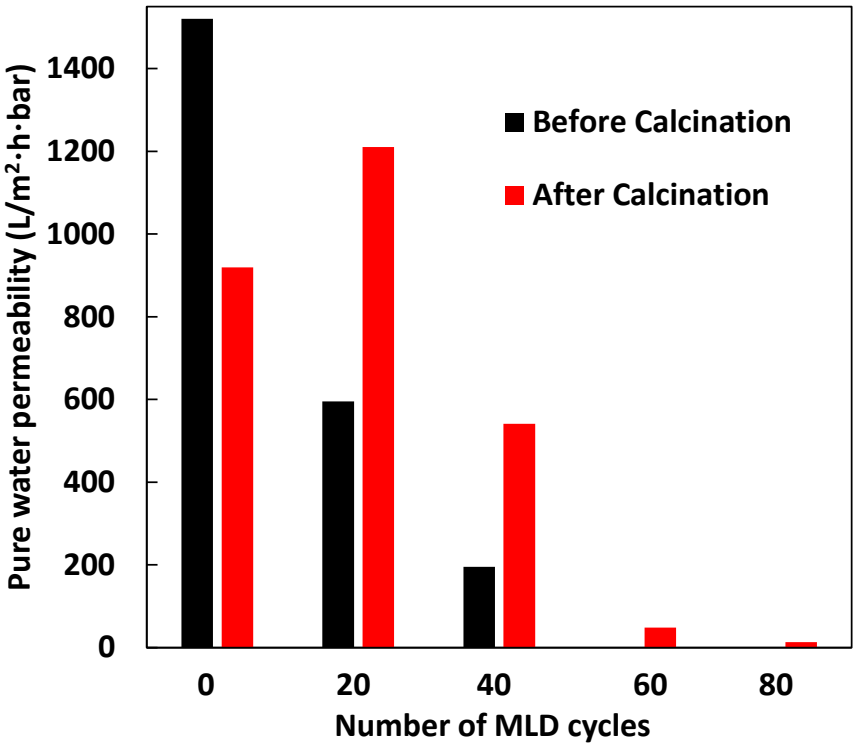

Figure 5.8. Pure water permeation through AAO with different cycles of MLD coatings before and after calcination at 250°C.

5.4.4 ANTIFOULING PERFORMANCE OF TiO_2 NANOFILTRATION MEMBRENES

Titanium dioxide (TiO_2) has received much attention in recent years to improve the antifouling property of membranes due to its hydrophilicity and great stability.[43, 44] Natural organic matter (NOM) is one of the major contributors to membrane fouling.[45]

NOM fouling tests were conducted using AAO-60TiO_2 membranes. Figure 5.10 showed the normalized fluxes in three cycles to evaluate the antifouling performance and recovery capability. Normalized flux is defined as the measured permeation flux at different water recovery divided by the initial flux in the first cycle.[46] As shown in Fig. 5.10, during the first cycle of NOM filtration, after collecting 10 mL (i.e., 20% water recovery) of SRHA solution, the permeate flux decreased by 62% for AAO-60TiO_2 membranes. Similar trend was also observed in the second and third cycle. After each NOM filtration cycle, we opened the module and conducted a simple membrane cleaning process by flushing the membrane surface with water at a rate of 4.0 L/min for 30 min. We found that AAO-60TiO_2 membrane showed a good flux recovery (77-84%), and this recovery capability was also superior to the reported polysulfone nanofiltration membrane[47]. NOM rejection was around 99% in each cycle for AAO-60TiO_2 membranes (Fig. 5.10).

5.5 CONCLUSION

TiO_2 nanofiltration membranes were prepared for the first time by using a novel technique, MLD. Influence of cycles of MLD on hybrid coating quality was investigated. Our results showed a defect-free, dense titanium alkoxide MLD coating was formed after complete support pore filling, and approximately 1 nm pores can be effectively generated by calcination at 250^oC in air. The AAO-60TiO_2 membrane showed a high pure water permeability of 48 L/(m^2·h·bar) and high rejection for MB and NOM, moderate rejection for salts, and good antifouling performance as well as recovery capability. Compared with traditional sol-gel method, MLD has the potential advantages of precise pore size control, simple fabrication process, and ability to scale up. We expect MLD will become a new

method for preparing TiO_2 nanofiltration membranes with well controlled thickness, composition, and membrane pore sizes.

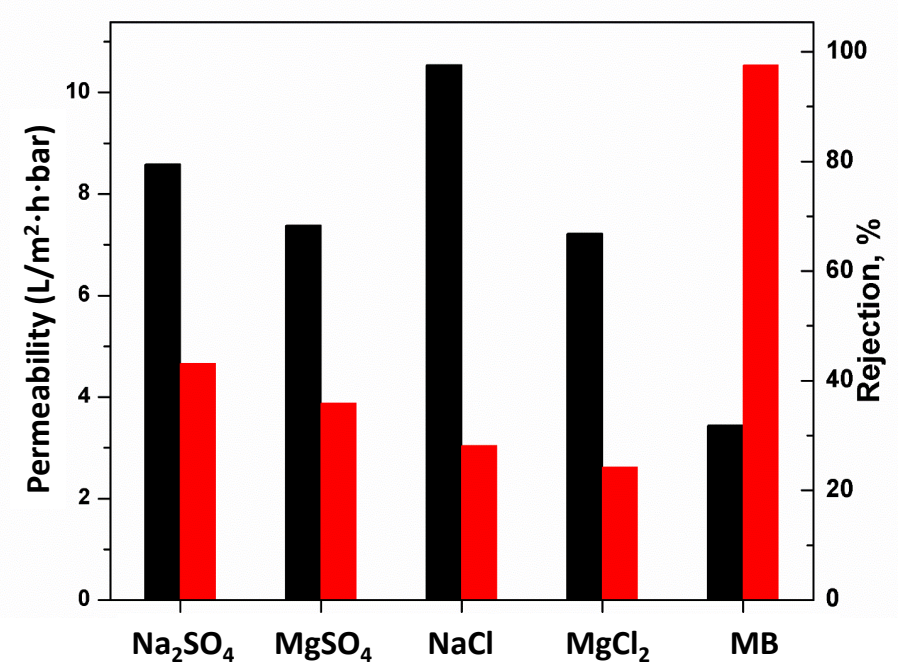

Figure 5.9. Permeation through AAO-60TiO_2 membrane (black bar) and rejection of AAO-60TiO_2 membrane (red bar).

5.6 ACKNOWLEDGEMENT

We gratefully acknowledge the financial support by the National Science Foundation (NSF) under Grant No. 1402772.

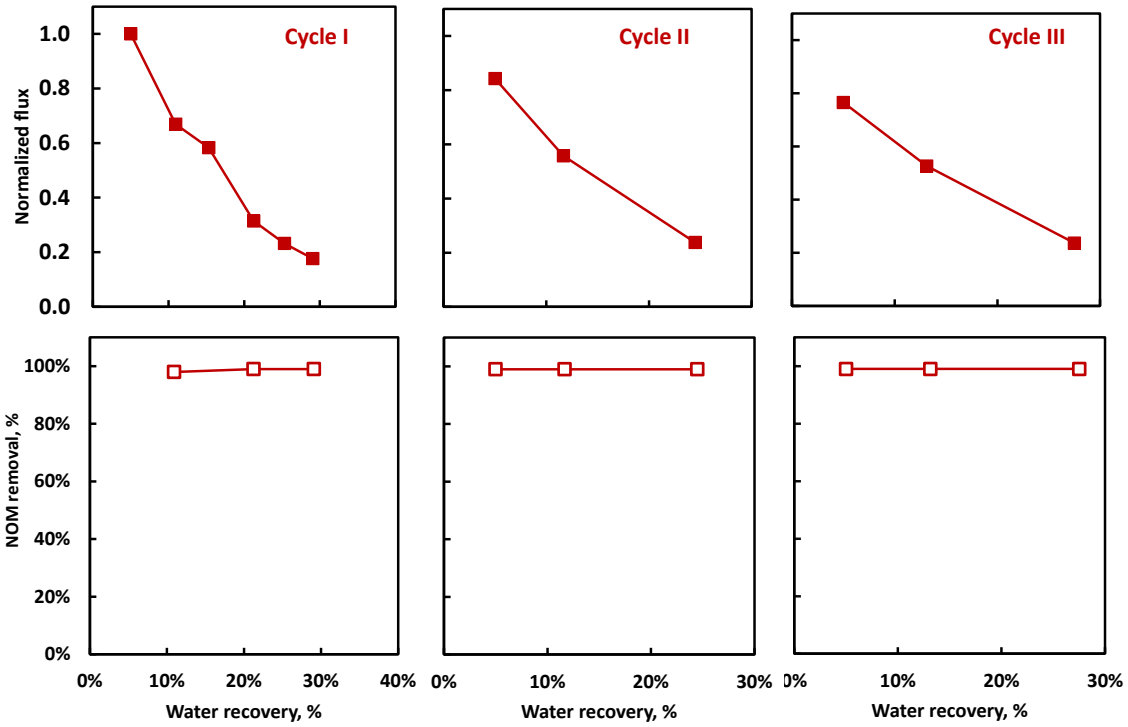

Figure 5.10. Three filtration cycles of NOM on AAO-60TiO_2 membrane: flux decline (first row) and NOM removal for the corresponding cycle (second row).

5.7 REFERENCES

[1] S. Zhu, S. Zhao, Z. Wang, X. Tian, M. Shi, J. Wang, S. Wang, Improved performance of polyamide thin-film composite nanofiltration membrane by using polyetersulfone/polyaniline membrane as the substrate, J. Membr. Sci. 493 (2015) 263-274.
[2] Y. Han, Z. Xu, C. Gao, Ultrathin Graphene Nanofiltration Membrane for Water Purification, Adv. Funct. Mater. 23 (2013) 3693-3700.
[3] N. Hilal, H. Al-Zoubi, N.A. Darwish, A.W. Mohammad, M. Abu Arabi, A comprehensive review of nanofiltration membranes: Treatment, pretreatment, modelling, and atomic force microscopy, Desalination 170 (2004) 281-308.
[4] A.W. Mohammad, Y.H. Teow, W.L. Ang, Y.T. Chung, D.L. Oatley-Radcliffe, N. Hilal, Nanofiltration membranes review: Recent advances and future prospects, Desalination 356 (2015) 226-254.
[5] D.A.L. Mahmut Selim Ersan , and Tanju Karanfil N-Nitrosodimethylamine (NDMA) Precursors Leach from Nanofiltration Membranes, Environ. Sci. Technol. Lett. 2 (2015) 66-69.
[6] B. Van der Bruggen, Chemical Modification of Polyethersulfone Nanofiltration Membranes: A Review, J. Appl. Polym. Sci. 114 (2009) 630-642.

[7] T. Van Gestel, C. Vandecasteele, A. Buekenhoudt, C. Dotremont, J. Luyten, B. Van der Bruggen, G. Maes, Corrosion properties of alumina and titania NF membranes, J. Membr. Sci. 214 (2003) 21-29.
[8] Q. Xu, M.A. Anderson, Sol–Gel Route to Synthesis of Microporous Ceramic Membranes: Preparation and Characterization of Microporous TiO2 and ZrO2 Xerogels, J. Am. Ceram. Soc. 77 (1994) 1939-1945.
[9] R.A. Peterson, M.A. Anderson, C.G. Hill Jr, Development of TiO2 membranes for gas phase nanofiltration, J. Membr. Sci. 94 (1994) 103-109.
[10] S. Benfer, U. Popp, H. Richter, C. Siewert, G. Tomandl, Development and characterization of ceramic nanofiltration membranes, Sep. Purif. Technol. 22-3 (2001) 231-237.
[11] T. Van Gestel, C. Vandecasteele, A. Buekenhoudt, C. Dotremont, J. Luyten, R. Leysen, B. Van der Bruggen, G. Maes, Salt retention in nanofiltration with multilayer ceramic TiO2 membranes, J. Membr. Sci. 209 (2002) 379-389.
[12] J. Sekulic, J.E. ten Elshof, D.H.A. Blank, A microporous titania membrane for nanofiltration and pervaporation, Adv. Mater. 16 (2004) 1546-1500.
[13] P. Marchetti, M.F.J. Solomon, G. Szekely, A.G. Livingston, Molecular Separation with Organic Solvent Nanofiltration: A Critical Review, Chem. Rev. 114 (2014) 10735-10806.
[14] Y. Cai, Y. Wang, X. Chen, M. Qiu, Y. Fan, Modified colloidal sol–gel process for fabrication of titania nanofiltration membranes with organic additives, J. Membr. Sci. 476 (2015) 432-441.
[15] H. Qi, S.D. Li, X.L. Jiang, J. Han, Preparation and Ions Retention Properties of TiO2 Nanofiltration Membranes, J. Inorg. Mater. 26 (2011) 305-310.
[16] M. Khalili, S. Sabbaghi, M.M. Zerafat, Preparation of ceramic gamma-Al2O3-TiO2 nanofiltration membranes for desalination, Chem. Pap. 69 (2015) 309-315.
[17] A.A. Dameron, D. Seghete, B.B. Burton, S.D. Davidson, A.S. Cavanagh, J.A. Bertrand, S.M. George, Molecular layer deposition of alucone polymer films using trimethylaluminum and ethylene glycol, Chem. Mat. 20 (2008) 3315-3326.
[18] X.H. Liang, M. Yu, J.H. Li, Y.B. Jiang, A.W. Weimer, Ultra-thin microporous-mesoporous metal oxide films prepared by molecular layer deposition (MLD), Chem. Commun. (2009) 7140-7142.
[19] H. Zhou, S.F. Bent, Fabrication of organic interfacial layers by molecular layer deposition: Present status and future opportunities, J. Vac. Sci. Technol. A 31 (2013) 18.
[20] X. Liang, A.W. Weimer, An overview of highly porous oxide films with tunable thickness prepared by molecular layer deposition, Current Opinion in Solid State and Materials Science 19 (2015) 115-125.
[21] Z.N. Song, Y. Huang, L. Wang, S.G. Li, M. Yu, Composite 5A zeolite with ultrathin porous TiO2 coating for selective gas adsorption, Chem. Commun. 51 (2015) 373-375.
[22] Z.N. Song, Y. Huang, W. W. Xu, L. Wang, Y. Bao, S.G. Li, M. Yu, Continuously Adjustable, Molecular-Sieving “Gate” on 5A Zeolite for Distinguishing Small Organic Molecules by Size, Sci. Rep. 5, 13981 (2015).
[23] J.W. Elam, D. Routkevitch, P.P. Mardilovich, S.M. George, Conformal Coating on Ultrahigh-Aspect-Ratio Nanopores of Anodic Alumina by Atomic Layer Deposition, Chem. Mat. 15 (2003) 3507-3517.

[24] G. Xiong, J.W. Elam, H. Feng, C.Y. Han, H.-H. Wang, L.E. Iton, L.A. Curtiss, M.J. Pellin, M. Kung, H. Kung, P.C. Stair, Effect of Atomic Layer Deposition Coatings on the Surface Structure of Anodic Aluminum Oxide Membranes, The Journal of Physical Chemistry B 109 (2005) 14059-14063.
[25] J.W. Elam, G. Xiong, C.Y. Han, H.H. Wang, J.P. Birrell, U. Welp, J.N. Hryn, M.J. Pellin, T.F. Baumann, J.F. Poco, J.H. Satcher, Atomic layer deposition for the conformal coating of nanoporous materials, J. Nanomater. (2006) 5.
[26] A.W. Ott, J.W. Klaus, J.M. Johnson, S.M. George, K.C. McCarley, J.D. Way, Modification of Porous Alumina Membranes Using Al2O3 Atomic Layer Controlled Deposition, Chem. Mat. 9 (1997) 707-714.
[27] T.D. Gould, A. Izar, A.W. Weimer, J.L. Falconer, J.W. Medlin, Stabilizing Ni Catalysts by Molecular Layer Deposition for Harsh, Dry Reforming Conditions, ACS Catal. 4 (2014) 2714-2717.
[28] Z.Y. Shang, R.L. Patel, B.W. Evanko, X.H. Liang, Encapsulation of supported metal nanoparticles with an ultra-thin porous shell for size-selective reactions, Chem. Commun. 49 (2013) 10067-10069.
[29] T. Tsuru, D. Hironaka, T. Yoshioka, M. Asaeda, Titania membranes for liquid phase separation: effect of surface charge on flux, Sep. Purif. Technol. 25 (2001) 307-314.
[30] M. Yu, H.H. Funke, R.D. Noble, J.L. Falconer, H2 separation using defect-free, inorganic composite membranes, J. Am. Chem. Soc. 133 (2011) 1748-1750.
[31] H.S. Chen, P.H. Chen, S.H. Huang, T.P. Perng, Toward highly efficient photocatalysis: a flow-through Pt@TiO2@AAO membrane nanoreactor prepared by atomic layer deposition, Chem. Commun. 50 (2014) 4379-4382.
[32] H. Zhou, M.F. Toney, S.F. Bent, Cross-linked ultrathin polyurea films via molecular layer deposition, Macromolecules 46 (2013) 5638-5643.
[33] H. Zhou, S.F. Bent, Highly Stable Ultrathin Carbosiloxane Films by Molecular Layer Deposition, The Journal of Physical Chemistry C 117 (2013) 19967-19973.
[34] S.H. Liu, L. Han, Y.Y. Duan, S. Asahina, O. Terasaki, Y.Y. Cao, B. Liu, L.G. Ma, J.L. Zhang, S.A. Che, Synthesis of chiral TiO2 nanofibre with electron transition-based optical activity, Nat. Commun. 3 (2012) 6.
[35] S.C. Yang, M. Sanghadasa, S. Priya, Highly ordered Pb(Zr0.52Ti0.48)O-3 piezoelectric nanorod arrays, Nanotechnology 24 (2013) 6.
[36] R.L. Patel, Y.-B. Jiang, X. Liang, Highly porous titania films coated on sub-micron particles with tunable thickness by molecular layer deposition in a fluidized bed reactor, Ceramics International 41 (2015) 2240-2246.
[37] P. Puhlfurss, A. Voigt, R. Weber, M. Morbe, Microporous TiO2 membranes with a cut off < 500 Da, J. Membr. Sci. 174 (2000) 123-133.
[38] J. Sekulić, M.W.J. Luiten, J.E. ten Elshof, N.E. Benes, K. Keizer, Microporous silica and doped silica membrane for alcohol dehydration by pervaporation, Desalination 148 (2002) 19-23.
[39] J. Schaep, B. Van der Bruggen, C. Vandecasteele, D. Wilms, Influence of ion size and charge in nanofiltration, Sep. Purif. Technol. 14 (1998) 155-162.
[40] A. Imhof, Preparation and Characterization of Titania-Coated Polystyrene Spheres and Hollow Titania Shells, Langmuir 17 (2001) 3579-3585.

[41] Y. Zhang, Y. Su, J. Peng, X. Zhao, J. Liu, J. Zhao, Z. Jiang, Composite nanofiltration membranes prepared by interfacial polymerization with natural material tannic acid and trimesoyl chloride, J. Membr. Sci. 429 (2013) 235-242.
[42] P. Simoncic, T. Armbruster, Cationic methylene blue incorporated into zeolite mordenite-Na: a single crystal X-ray study, Microporous Mesoporous Mat. 81 (2005) 87-95.
[43] S.S. Madaeni, S. Zinadini, V. Vatanpour, A new approach to improve antifouling property of PVDF membrane using in situ polymerization of PAA functionalized TiO2 nanoparticles, J. Membr. Sci. 380 (2011) 155-162.
[44] M. Safarpour, A. Khataee, V. Vatanpour, Preparation of a Novel Polyvinylidene Fluoride (PVDF) Ultrafiltration Membrane Modified with Reduced Graphene Oxide/Titanium Dioxide (TiO2) Nanocomposite with Enhanced Hydrophilicity and Antifouling Properties, Ind. Eng. Chem. Res. 53 (2014) 13370-13382.
[45] N. Hilal, H. Al-Zoubi, N.A. Darwish, A.W. Mohamma, M. Abu Arabi, A comprehensive review of nanofiltration membranes:Treatment, pretreatment, modelling, and atomic force microscopy, Desalination 170 (2004) 281-308.
[46] J.J. Song, Y. Huang, S.-W. Nam, M. Yu, J. Heo, N. Her, J.R.V. Flora, Y. Yoon, Ultrathin graphene oxide membranes for the removal of humic acid, Sep. Purif. Technol. 144 (2015) 162-167.
[47] J.A. Nilson, F.A. DiGiano, Influence of NOM composition on nanofiltration, J. AM. WATER. WORKS. ASS. 88 (1996) 53-66.

CHAPTER 6:

NANO-VALVED ADSORBENTS FOR CH_4 STORAGE

6.1 ABSTRACT

A novel concept of utilizing nanoporous coatings as effective nano-valves on microporous adsorbents was developed for high capacity natural gas storage at low storage pressure. The work reported here for the first time presents the concept of nano-valved adsorbents capable of sealing high pressure CH_4 inside the adsorbents and storing it at low pressure. Traditional natural gas storage tanks are thick and heavy, which makes them expensive to manufacture and highly energy-consuming to carry around. Our design uses unique adsorbent pellets with nano-scale pores surrounded by a coating that functions as a valve to help manage the pressure of the gas and facilitate more efficient storage and transportation. We expect this new concept will result in a lighter, more affordable product with increased storage capacity. The nano-valved adsorbent concept demonstrated here can be potentially extended for the storage of other important gas molecules targeted for diverse relevant functional applications.

6.2 INTRODUCTION

Natural gas, which consists mainly of methane and abundant in U.S. and worldwide, is considered to be a valuable alternative clean vehicular fuel compared to gasoline.[1,2] In addition, fracking technology dramatically makes methane inexpensive .[3] Therefore, in recent years, more and more attention has been concentrated on the

development of natural gas vehicles (NGV). However, the biggest issue that restricts the widespread adoption of today's NGV in U.S. and globally is fitted on-board fuel tanks that are too large, cumbersome, and expensive, since natural gas is typically stored in a cryogenic tank as liquefied natural gas (LNG) at 113 K due to the low critical temperature of methane (T_c = 191 K) or as compressed natural gas (CNG) at 200-300 bar.[4,5] A promising alternative is adsorbed natural gas (ANG), where the gas is stored as an adsorbed phase in porous materials. High surface area materials such as zeolites,[6] metal-organic frameworks (MOFs),[6-8] covalent organic frameworks (COF),[9-11] activated carbon,[6,12] and carbon nanotubes[13,14] have shown great potential for CH_4 storage for ANG technologies. However, CH_4 storage capacity of current adsorbents at ambient temperature and moderate pressure, typically lower than 35 bar, is much lower than the CH_4 storage volumetric target set by U.S. Department of Energy (DOE) which corresponds to 263 V (STP: 273.15 K, 1 atm)/V.[3,15] Therefore, it is critical to develop advanced materials/methods capable of storing high capacity CH_4 within the adsorbents at a relatively low pressure that facilitates more efficient storage and transportation.

Herein, we demonstrate a novel concept, in which nano-valved adsorbents are utilized for reversible, high capacity CH_4 storage at low storage pressure. The nano-valved adsorbents comprise of a nanoporous coating on the outer surfaces of the adsorbent pellets. The nanopores of the coating layer along with the adsorbate adsorbed in the nanopores function as a valve that can be opened and closed on demand for natural gas storage. Figure 6.1a shows the structure of nano-valved adsorbents and its functioning process. Methane loading occurs at high pressures with the nano-valve open. The nano-valve is then closed by adsorbing a strongly adsorbed sealing molecules in nanopores of the coating when the

adsorbents are fully loaded, holding high pressure methane within the adsorbent pellet. Loaded adsorbents can then be stored at low pressure, and the nano-valve can be re-opened to release the stored CH_4 when needed. In our current study, to demonstrate the concept of nano-valved adsorbents, 5A zeolite was selected as the model sorbent, because it is commercially available and has a reasonable CH_4 saturation amount. Sol-gel process was applied to prepare the high quality coating layer; besides the sol-gel process, a new coating technique, molecular layer deposition (MLD), was also applied for further pore size reduction of the coating layer. Some of us have shown that MLD can be used to deposit coatings with sub-nm pores.[16,17] 2,2-dimethyl butane (DMB) was used as the adsorbate for nano-valve closing. The nano-valve allows high pressure inside and low pressure outside. The maximum pressure drop that the adsorbed/sealing molecule can hold can be calculated using Young-Laplace equation and estimated to be higher than 200 bar at room temperature for a 1.5 nm pore filled with DMB (see Supporting Information).

6.3 RESULTS AND DISCUSSION

A high quality coating layer is the key to the proposed nano-valved adsorbent. In our study, MCM-48 (Mobil Composition of Matter number-48) was used because it is a periodic mesoporous amorphous silica possessing long range ordered framework with uniform mesopores.[18] In addition, the amorphous nature of MCM-48 promotes the formation of continuous layers, by overcoming the typical issues found in crystalline layers (i.e. formation of grain boundaries, intercrystalline defects which are detrimental for the integrity of the resultant layers). A typical coating procedure is shown in Figure 6.5 and described in detail in Supporting Information. Figure 6.1b shows a representative SEM image of the cross-sectional view of MCM-48 coated 5A beads (MCM-48-5A).

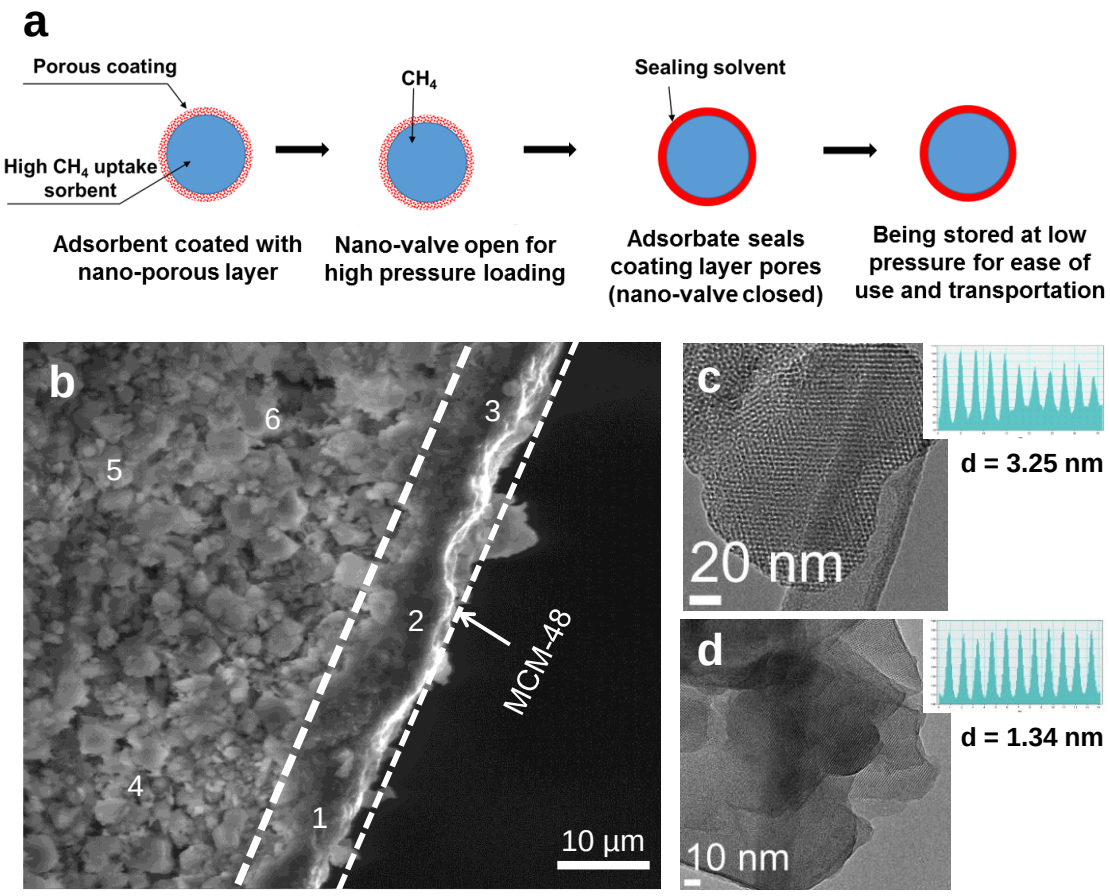

Figure 6.1. Diagram of CH_4 storage by using nano-valved adsorbents (a); cross-sectional SEM image of MCM-48-5A (EDS analysis points are indicated in the figure) (b); HRTEM images and pore sizes of MCM-48-5A adsorbent (c); HRTEM image and pore size of MLD-MCM-48-5A adsorbent (d).

The MCM-48 layer on the external surface of 5A beads was continuous with a thickness of ~7.5 µm. EDX (Energy Dispersive X-ray Spectroscopy) analysis results are shown in Table 6.1. Compared to the compositions of 5A zeolite (points 4-6), the MCM-48 region (points 1-3) consisted of "Si" and "O", suggesting no obvious penetration of the gel into 5A bead pores. BET area dropped by 19% compared with 5A zeolite after MCM-48 coating (Table 6.2).

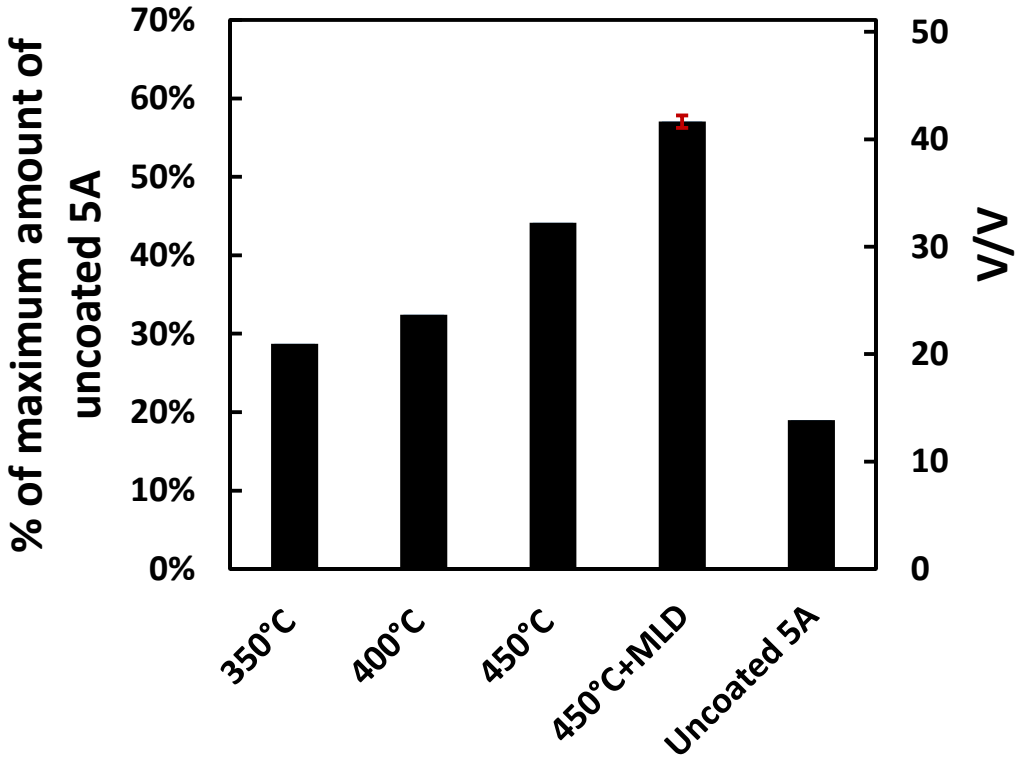

Figure 6.2 Steady state CH_4 storage capacity of MCM-48 coated 5A adsorbent calcined at different temperature and uncoated 5A zeolite.

Methane adsorption isotherm was measured for the bare 5A zeolite beads (Figure 6.6). The isotherm we obtained was consistent with literature data at low pressure reported by Nam et al.[19] Nam et al. did not measure the amounts of CH_4 adsorbed at pressure higher than 20 bar, whereas we have measured at pressure up to 120 bar. We found that CH_4 adsorption was saturated at ~100 bar with a saturation capacity of 2.67 mmol/g. Thus the maximum volumetric density (capacity) for the bare 5A was 73 V/V when using a bulk density of 1.22 g/ml obtained by Hg porosimetry analysis (see Supporting Information).

In a nano-valve functioning test, approximately 0.50 g adsorbent was loaded to the adsorption tank (Figure 6.7, details of valve functioning test was reported in Supporting Information). CH_4 was introduced at ~50 bar, at which ~95% of the maximum capacity

was expected to be adsorbed in equilibrium. We then adjusted the back pressure regulator and mass flow controller (MFC) to have CH_4 flow through reference tank that was filled with DMB liquid, and had the DMB saturated CH_4 flow through the sample cell to allow DMB adsorbing into the nanopores of the MCM-48 coating layer and sealing the valve. After introducing DMB for 1 h, the back pressure regulator was opened gradually to release the system pressure from ~50 bar to ~1 bar in another 1 h. We then systematically measured the CH_4 stored capacity as a function of time (CH_4 storage performance curve) by using a smaller scale high-precision transducer.

In the preparation of the MCM-48 layer, cetyltrimethyl ammonium bromide (CTAB) was used as the template. During calcination, the pore opening of MCM-48 layer was achieved by gradual removal of the organic template. Thus, the calcination conditions are expected to influence the valve functioning of the resulting coated adsorbents. Three different calcination temperatures (350, 400 and 450°C) were investigated. CH_4 storage performance curves are shown in Figure 6.8. For calcination temperatures at 350 and 400°C, a CH_4 storage capacity of < 52% of the maximum amount of bare 5A was obtained at time zero when the pressure of valve functioning test system was released down to 1 bar for storage (Figure 6.8a-b). This suggests that the nanopores of MCM-48 layer were only partially opened, and some template molecules were still left within the coating layer. When calcination temperature increased to 450°C, as shown in Figure 6.8c, an initial CH_4 storage capacity of 85% of the maximum amount of uncoated 5A was obtained. This was close to the highest capacity potentially achievable with the current valve sorbents considering the BET area decrease by about 19% after MCM-48 coating. Therefore, 450°C seems to be an appropriate temperature to completely open MCM-48 coating pores. We

did not further increase the calcination temperature in this study to avoid generating potential cracks due to the thermal stress at elevated temperatures. The CH_4 storage capacity of MCM-48 coated 5A zeolite decreased gradually with time (Figure S4a-c), and reached almost stable at 28.7%, 32.4% and 44.1% (20.9 V/V, 23.6V/V and 32.2V/V) of the maximum capacity of bare 5A zeolite after 4 h as shown in Figure 6.2 under 350, 400 and 450°C calcination; after further modification by MLD, the stable CH_4 storage capacity reached 57.1% (41.7 V/V), as discussed below; in comparison, bare 5A can only hold 19% (13.8 V/V) of the maximum capacity at the same pressure (Figure 6.2 and Figure 6.8d). High resolution transmission electron microscopy (HRTEM) images of MCM-48 coated 5A adsorbent are shown in Figure 6.1c and Figure 6.9. The images indicated pore sizes are in the range of 3.1-3.4 nm, which is the expected size range for the MCM-48 mesoporous silica structure. For clarity, pore size histograms have been included as insets in each HRTEM image. According to our estimation (See supporting Information) 3-nm pores should be able to hold > 100 bar pressure drop. Therefore, we speculate, for MCM-48 (450°C calcination) coated 5A sorbent, that the drop of the CH_4 storage capacity from 85% to 44% was due to the non-uniform coating pore sizes; the high quality coatings with small pores sealed adsorbed CH_4 at an amount of 44% of the maximum capacity of bare 5A, whereas the coatings with larger pores caused a gradual leak of CH_4. The non-uniformity can be improved by MLD post-treatment. MLD is a gas phase deposition technique capable of depositing ultrathin conformal coatings on high aspect ratio substrate with accurate angstrom-level coating thickness control.[16,17] We prepared 3 cycles of MLD coating on the 450°C calcined MCM-48 coated 5A adsorbent (MLD-MCM-48-5A) (See Supporting Information). After 3-cycle MLD treatment, the original MCM-48 pores were reduced to

~1.34-1.42 nm (Figure 6.1d and Figure 6.10). We then conducted 3 cycles of CH_4 storage test on the MLD-MCM-48-5A adsorbent with 50 bar loading pressure and 1 bar storage pressure. As shown in Figure 6.3, the CH_4 storage capacity decreased with time for the first 3 h. The stable CH_4 storage capacity was about 55.8-58.4% (40.7-42.6 V/V) of the maximum capacity of the uncoated 5A beads, which was about 200% higher than storage capacity of the uncoated 5A beads at the same storage pressure, suggesting good stability and reversibility of our nano-valved adsorbents for CH_4 storage. We made a comparison of our nano-valve adsorbents with other representative porous materials, including metal organic frameworks (MOFs) and covalent organic frameworks (COFs), for CH_4 storage. Figure 6.4 shows the CH_4 storage capacity of our nano-valve adsorbents stored at 1 bar is comparable to the reported materials with a storage pressure of 7-15 bar.

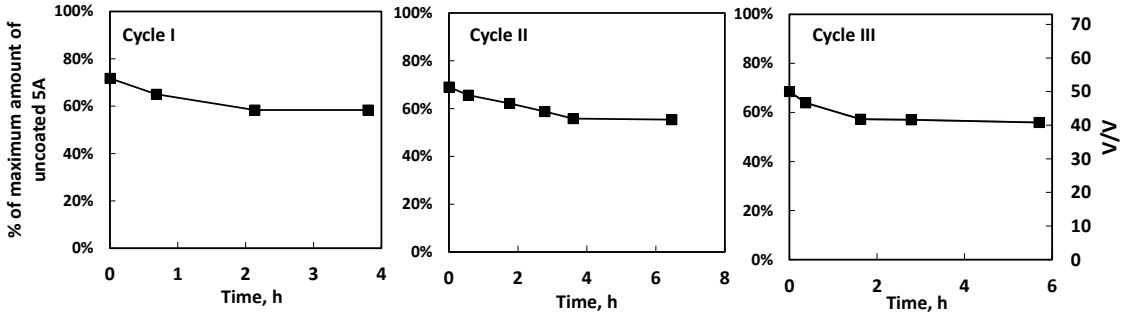

Figure 6.3 Three cycles of CH_4 storage test on MLD-MCM-48-5A adsorbent (loading pressure 50 bar, storage pressure 1bar).

We have demonstrated the proof-of-concept of nanovalved adsorbents on a commercially available adsorbent (zeolite 5A beads) displaying only moderate CH_4 uptake capacity. In principle, the amount of CH_4 stored by the proposed concept can be highly improved (to potentially reach the ARPA-E's target for energy densities) by choosing adsorbents having high CH_4 uptakes at high pressures. Among these materials, MOF-177 [20], COF-102 [11], and COF-105-Eth-trans [11] have shown remarkably high volumetric and

gravimetric densities at high pressures. As shown in Table 6.3, loading CH_4 on these materials at a pressure of 250 bar could meet the DOE ARPA-E's energy density targets for sorbent (volumetric energy density > 12.5 MJ/L, gravimetric energy density > 0.5 g CH_4/g sorbent.

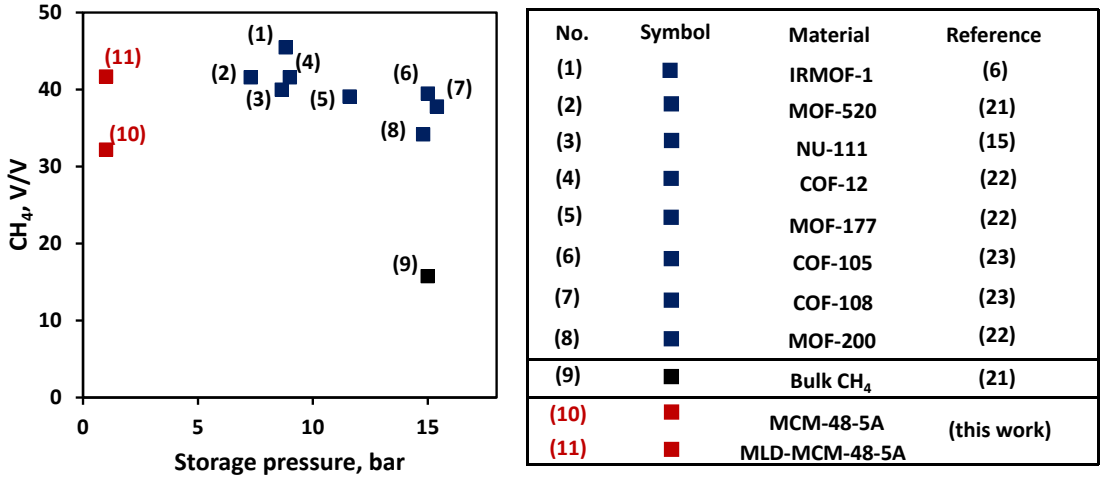

Figure 6.4 Comparison of nano-valve adsorbents with porous materials for CH_4 storage: CH_4 storage amount versus CH_4 storage pressure. Blue squares (1-8) represent porous materials from literatures[7,15,21-23]; bulk density of methane is represented by black square (9)[21]; red squares (10-11) indicate nano-valve adsorbents from this study.

6.4 SUPPORTING INFORMATION

6.4.1 NANO-VALVED ADSORBENT SYNTHESIS

MCM-48 solution was prepared by dissolving sodium hydroxide (98%, Sigma-Aldrich) and CTAB (cetyltrimethyammonium bromide) in deionized water at 40°C. The mixture was stirred for 30 minutes before adding TEOS (tetraethylorthosilicate). The molar composition of the solution was 1.0 TEOS: 0.48 CTAB: 0.46 NaOH: 56.0 H_2O. The solution was stirred for another 60 minutes and then it was transferred to autoclave, in which the 5A zeolite beads (2.5 mm diameter from W.R.Grace & Co) were placed. The MCM-48 solution and the 5A zeolite beads were hydrothermally treated at 100°C for 72 h. Then, the coated beads were removed from the autoclave, washed gently with water, and

dried at 120°C overnight. The template (CTAB) was removed by calcination in air in the 350-450 °C range for 4 h with a heating and cooling rate of 1°C/min.

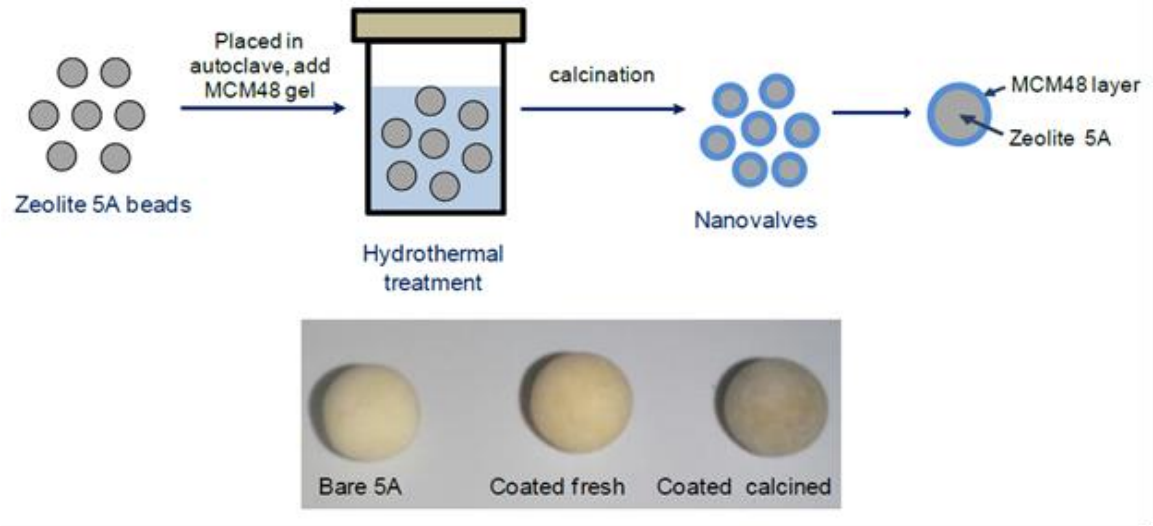

Figure 6.5 Diagram of coating procedure for MCM-48-5A adsorbent and pictures of samples.

6.4.2 GAS SORPTION MEASUREMENT

Ultra-high purity CH_4 (99.999%), and He (99.999%) were purchased from Airgas. Gas adsorption isotherms were measured by a volumetric method using a home-built adsorption system. Sorbent was firstly outgassed at 200°C for 2 h. Helium was then used to calibrate the volume of adsorption cell with sorbent at 20°C. After vacuum to remove residue gasses in the adsorption system, CH_4 was introduced at 20°C. The pressure change was collected in real time using a Swagelok E model transducer (0.0-100.0 psia) for low pressure, an ASHCROFT (0-200 bar) transducer for high pressure, and LabVIEW 2012 software.

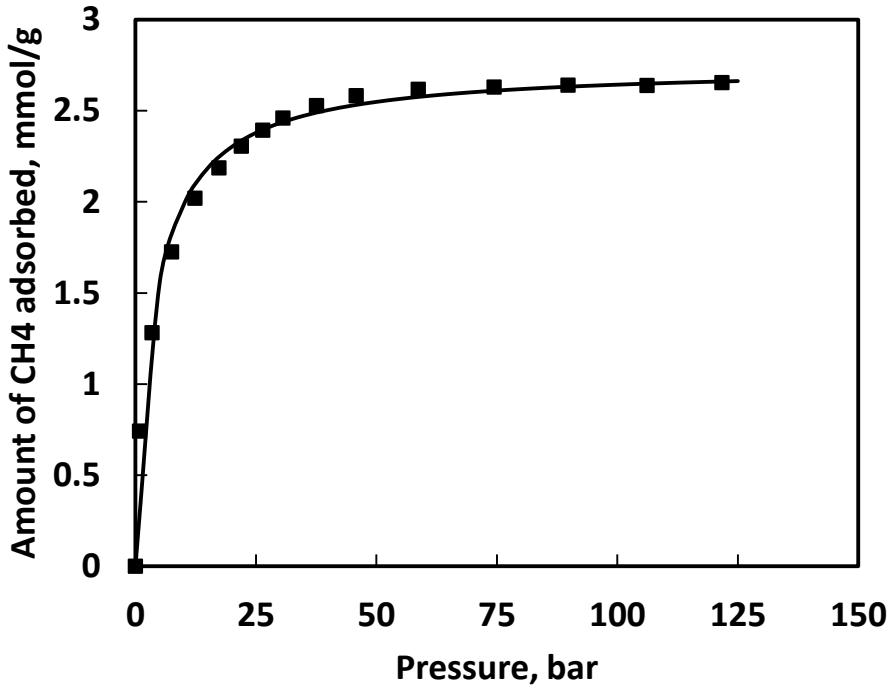

Figure 6.6 Adsorption isotherm of uncoated 5A zeolite beads at 20°C.

6.4.3 NANO-VALVE FUNCTIONING TEST

In a typical nano-valve functioning test (Figure 6.7), approximately 0.5g of adsorbent is added to the adsorption tank. A vacuum pump is used to evacuate the sample at 200°C and reference lines before testing. Then, CH_4 is introduced to the system at 50 bar and allowed enough time to reach equilibrium. When CH_4 adsorption reaches equilibrium at 50 bar, we then adjust the TESCOM back pressure regulator (R1) and BROOKS 5850 E series mass flow controllers (MFC-1, MFC-2) to have CH_4 continuously introduced to the system by closing V3, opening the valves V2, V8, V7 and V4 to maintain the whole system pressure at about 50 bar. Next, sealing molecule (2,2-DMB) vapor, in the reference tank, will be blown into the adsorption tank by a slow CH_4 flow. The sealing molecule vapor is used to seal the porous coating layer on the adsorbents. After 1 h, the valve V2 is

closed to stop feeding the CH_4, while maintaining the valve V1, MFC-2 open and adjust the R1 to release the system pressure gradually from 50 bar to 1 bar within 1 h. After reaching~1 bar, the storage system is closed (valves V1, V3, and V5 were closed) and the pressure change is monitored to calculate CH_4 leakage rate. After storage test, the sample cell is heated to 150°C to desorb the CH_4 sealed inside the coated adsorbents. The amount of CH_4 stored is calculated based on the system volume, pressure, and temperature.

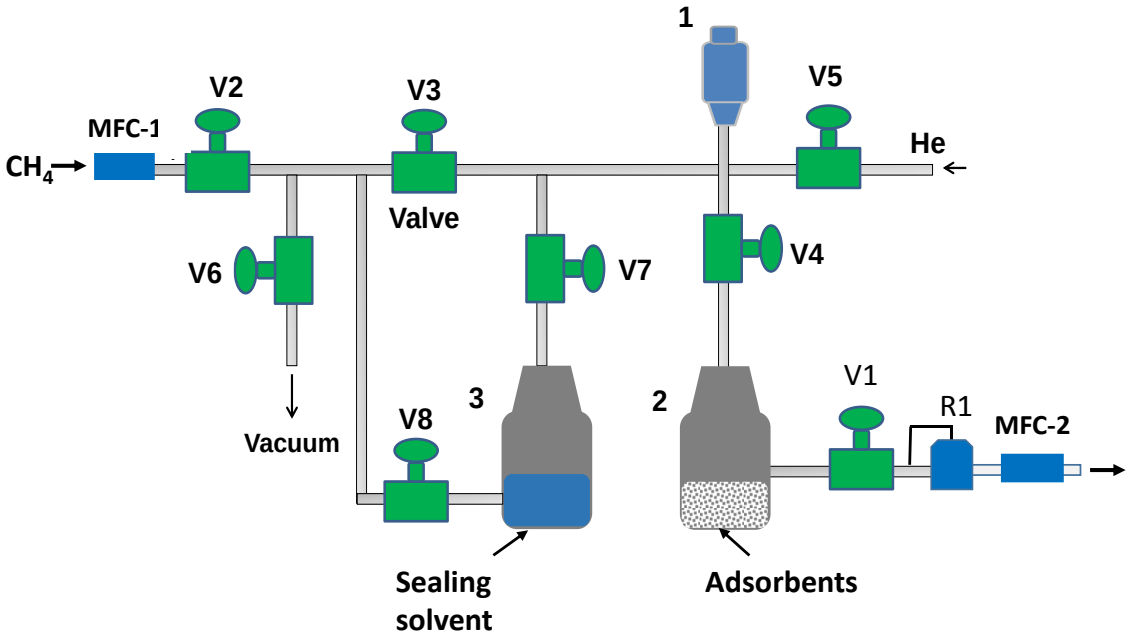

Figure 6.7 Nano-valved sorbent functioning testing system. 1-pressure transducer, 2-adsroption tank, 3-reference cell, MFC-mass flow controller, R1-back pressure regulator, V1-V8 valve.

Before we conducted QC testing for sorbents with coating, we examined the accuracy of calculating adsorbed CH_4 amount in sorbents by collecting CH_4 in gas phase by heating sorbents to 150-200°C. Specifically, we pressurized adsorption cell to ~2 bar and allowed CH_4 adsorption to reach steady state. Once it reached steady state, the

adsorbed amount in sorbents will be known from the adsorption isotherm. Then, the adsorption cell will be heated to a desired temperature between 150 and 200 °C to desorb CH_4 to the gas phase. By comparing CH_4 in the gas phase before and after heating, adsorbed amount of CH_4 is calculated. From our experiments for 5 sorbents, we found this method gave consistent adsorbed amounts with adsorption isotherm, and variation was within 3%. Therefore, our QC evaluation method is highly reliable.

Through these studies screened by low pressure QC test, the sample showed the highest amount of CH_4 stored will be selected for high pressure QC testing.

6.4.4 Molecular layer deposition on MCM-48-5A adsorbent

The MLD coatings were prepared by using trimethyl aluminum (TMA) (Al(CH3)3; 97%, Sigma Aldrich) and ethylene glycol (HO(CH2)2OH; 99%, Alfa Aesar) as precursors. Each MLD cycle started with 240 s vacuum. TMA was fed into the reactor until a pressure of 300 mTorr and then settled for 120 s; 240 s vacuum was followed to evacuate extra unreacted TMA. Ultrahigh purity N_2 (Airgas) was used as the purge gas at 20 sccm for 30 second. Then 240 s vacuum was applied to evacuate N_2. Ethylene glycol (EG) was then introduced into the reactor until a pressure of 50 mTorr and settled for 120 s; then the above evacuation and purge operation were repeated for EG dosing. This whole process finishes one MLD cycle. MLD reactions were conducted at 100 °C. After 3 cycles of MLD modification, the coated samples were heated in air from room temperature to 250°C at a rate of 1°C/min, kept at 250°C for 4 h, and then cooled to room temperature at the same rate.

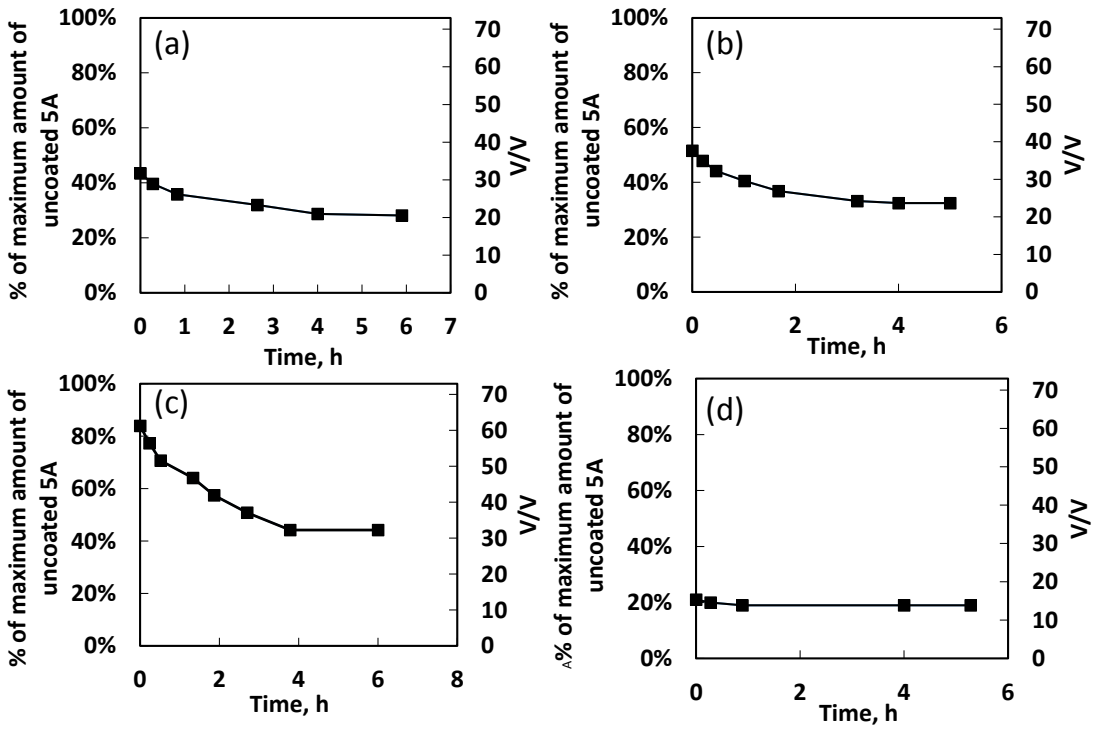

Figure 6.8 CH_4 storage test (loading pressure 50 bar, storage pressure 1bar) on MCM-48-5A adsorbent calcined at 350°C (a); calcined at 400°C (b); calcined at 450°C (c); uncoated 5A zeolite (d).

6.4.5 CHARACTERIZATION

6.4.5.1 SEM.

SEM images were collected on a Nova NanoSEM 600 FEI with an acceleration voltage of 10 kV. EDX was carried out to determine the composition of selected samples.

6.4.5.2 HRTEM

FEI Tecnai F20 transmission electron microscope operated at 200 KV was used to analyze the pore size of the MCM-48-5A and MLD-MCM-48-5A adsorbents. The samples were dispersed on lacey carbon films supported on 300 mesh TEM copper grids and Z-contrast scanning TEM (STEM) images were collected at spatial resolution of ~ 0.2 nm

using nanoprobe and Fischione Model 3000 High Angle Annular Dark Field (HAADF) detector. ImageJ, freely available software, was used to analyze STEM images and measure pores size distributions.

6.4.5.3 BET

N_2 BET surface areas were collected in a Micromeritics Tristar-3000 porosimeter at 77 K using liquid nitrogen as coolant. Before measurements, the samples were degassed at 300 ºC for 6 h.

6.4.5.4 Hg POROSIMETRY

Hg measurements were collected in a Autopore IV porosimeter. The volume of mercury in the penetrometer's stem was measured by determining the penetrometer's electrical capacitance. Autopore IV software was used to convert this electrical capacitance into data points showing the volume of mercury penetrating the pores of the sample.

6.4.6 ESTIMATION OF THE MAXIMUM HOLDING PRESSURE OF NANOPORES FILLED WITH ADSORBATES

We used Young-Laplace equation to estimate to the maximum holding pressure for nanopores filled with condensed sealing molecules:

$$\Delta P = 2\gamma \cos \theta / r,$$

where ΔP is the pore-entry pressure, γ is the liquid surface tension, θ is the contact angle, and r is pore radius. When 2,2-dimethylbuatne (DMB) is used as the sealing molecule in 1.5 nm alumina or silica pores, the estimated pressure that can push the liquid out of the

pore is approximately 200 bar, given the surface tension of DMB is 15.7 $mN \cdot m^{-1}$ (J. Chem. Eng. Data 2009, 54 (6) 1761) and assuming DMB completely wets the pore wall.

Table 6.1. Atomic EDS analysis for MCM-48-5A.

Element	5A region (points 4-6)	MCM-48 region (points 1-3)
Al	19.8	0.0
Si	22.3	31.4
O	49.6	68.6
Ca	3.5	0.0
Na	4.8	0.0

Table 6.2. BET area before and after MCM-48 coating.

Sample	BET area (m^2/g)	% of reduction
5A zeolite beads	453	baseline
MCM-48-5A adsorbent	367	19

Table 6.3. Energy densities of sorbents at 25°C with loading pressures of 250 and 300 bar.

Material	Crystal density (g/mL)	Energy density at 250 bar		Energy Density at 300 bar	
		Volumetric (MJ/L)	Gravimetric (g CH_4/g sorbent)	Volumetric (MJ/L)	Gravimetric (g CH_4/g sorbent)
MOF-177	0.42	12.7	0.54	13.3	0.556
COF-102	0.42	13.0	0.56	13.5	0.578
COF-105-Eth-trans	0.26	13.2	0.91	13.9	0.962

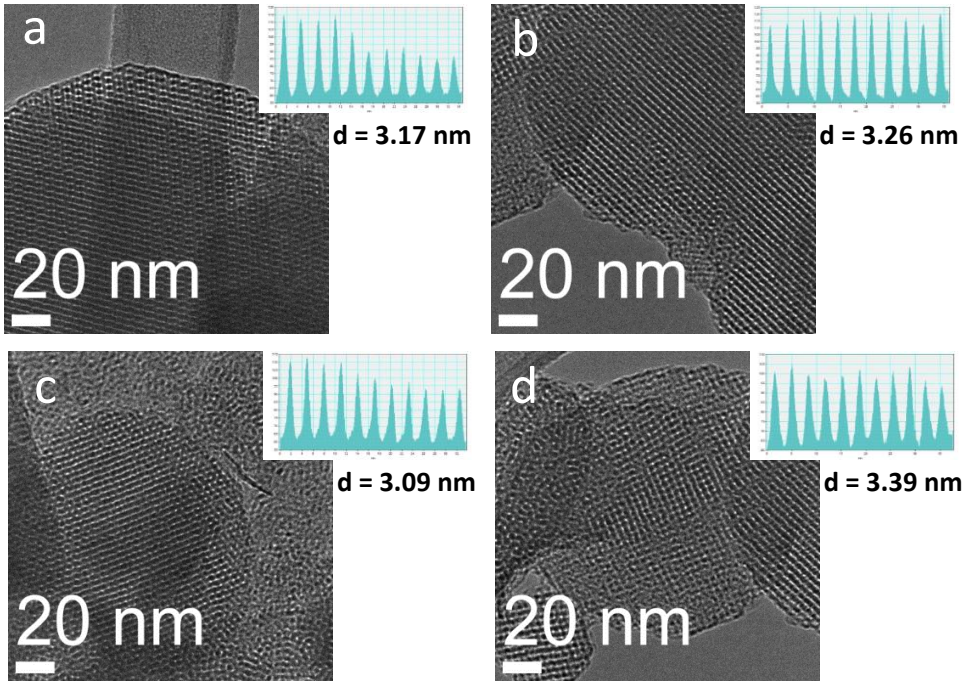

Figure 6.9. HRTEM images and pore sizes of MCM-48-5A adsorbents.

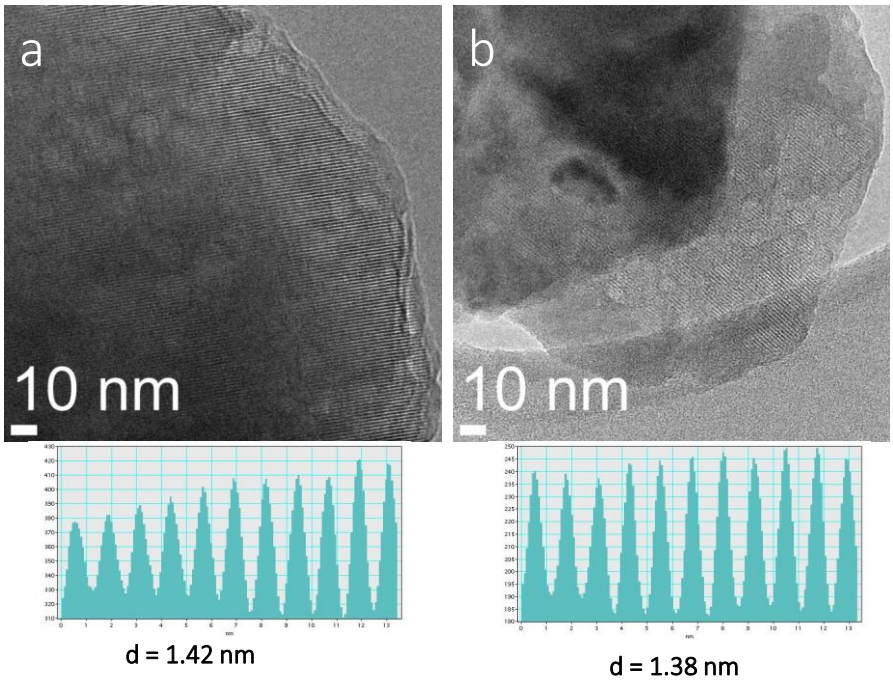

Figure 6.10 HRTEM images and pore sizes of MLD-MCM-48-5A adsorbents.

6.5 CONCLUSION

A novel concept of utilizing nanoporous coatings as effective nano-valves on microporous adsorbents was developed for high capacity natural gas storage at low storage pressure. Using 5A zeolite as a model adsorbent, ~7.5 μm thick, optimized MCM-48 coating with an average pore size of 3.25 nm was deposited on the external surface of the 5A beads. The nanopores of the MCM-48 coating functioned as a valve that can be opened and closed on demand. CH_4 was loaded at high pressure (≥50 bar) with the nano-valve open. The nano-valve was closed by adsorbing DMB in the pores of MCM-48 coating when the adsorbent was fully loaded. The loaded adsorbent can be stored at low pressure (~1bar) and the nano-valves can be opened again for releasing the stored CH_4 by desorbing DMB. After 4 h storage at low pressure (1 bar), MCM-48 coated 5A adsorbent can hold 44.1% (32.2 V/V) of the maximum capacity of bare 5A beads (73 V/V). After further pore size reduction to ~1.4 nm by molecular layer deposition (MLD), the CH_4 storage capacity increased to 55.8-58.4% (40.7-42.6 V/V) of the maximum capacity of the bare 5A beads, which was about 200% higher than storage capacity of the bare 5A beads at the same storage pressure.

6.6 ACKNOWLEDGEMENT

We gratefully acknowledge the support by the Department of Energy (DOE) Advanced Research Projects Agency-Energy (ARPA-E) under Grant No. DE-AR0000247.

6.7 REFERENCES

1 Alvarez, R. A., Pacala, S. W., Winebrake, J. J., Chameides, W. L. & Hamburg, S. P. Greater focus needed on methane leakage from natural gas infrastructure. *Proceedings of the National Academy of Sciences* **109**, 6435-6440 (2012).

2 Mason, J. A., Veenstra, M. & Long, J. R. Evaluating metal-organic frameworks for natural gas storage. *Chemical Science* **5**, 32-51 (2014).
3 Li, B. *et al.* A Porous Metal–Organic Framework with Dynamic Pyrimidine Groups Exhibiting Record High Methane Storage Working Capacity. *J. Am. Chem. Soc.* **136**, 6207-6210 (2014).
4 Tran, L. D., Feldblyum, J. I., Wong-Foy, A. G. & Matzger, A. J. Filling Pore Space in a Microporous Coordination Polymer to Improve Methane Storage Performance. *Langmuir* **31**, 2211-2217 (2015).
5 Menon, V. C. & Komarneni, S. Porous Adsorbents for Vehicular Natural Gas Storage: A Review. *Journal of Porous Materials* **5**, 43-58 (1998).
6 Saha, D., Bao, Z., Jia, F. & Deng, S. Adsorption of CO2, CH4, N2O, and N2 on MOF-5, MOF-177, and zeolite 5A. *Environ. Sci. Technol.* **44**, 1820-1826 (2010).
7 Düren, T., Sarkisov, L., Yaghi, O. M. & Snurr, R. Q. Design of New Materials for Methane Storage. *Langmuir* **20**, 2683-2689 (2004).
8 Furukawa, H. *et al.* Ultrahigh Porosity in Metal-Organic Frameworks. *Science* **329**, 424-428 (2010).
9 Mendoza-Cortes, J. L., Pascal, T. A. & Goddard, W. A. Design of Covalent Organic Frameworks for Methane Storage. *The Journal of Physical Chemistry A* **115**, 13852-13857 (2011).
10 Mendoza-Cortés, J. L., Han, S. S., Furukawa, H., Yaghi, O. M. & Goddard, W. A. Adsorption Mechanism and Uptake of Methane in Covalent Organic Frameworks: Theory and Experiment. *The Journal of Physical Chemistry A* **114**, 10824-10833 (2010).
11 Furukawa, H. & Yaghi, O. M. Storage of Hydrogen, Methane, and Carbon Dioxide in Highly Porous Covalent Organic Frameworks for Clean Energy Applications. *J. Am. Chem. Soc.* **131**, 8875-8883 (2009).
12 Zhou, Y. P., Dai, M., Zhou, L., Sun, Y. & Su, W. Storage of methane on wet activated carbon: influence of pore size distribution. *Carbon* **42**, 1855-1858 (2004).
13 Sun, Y., Liu, C., Su, W., Zhou, Y. & Zhou, L. Principles of methane adsorption and natural gas storage. *Adsorption* **15**, 133-137 (2009).
14 Yulong, W., Fei, W., Guohua, L., Guoqing, N. & Mingde, Y. Methane storage in multi-walled carbon nanotubes at the quantity of 80 g. *Mater. Res. Bull.* **43**, 1431-1439 (2008).
15 Peng, Y. *et al.* Methane Storage in Metal–Organic Frameworks: Current Records, Surprise Findings, and Challenges. *J. Am. Chem. Soc.* **135**, 11887-11894 (2013).
16 Song, Z. N., Huang, Y., Wang, L., Li, S. G. & Yu, M. Composite 5A zeolite with ultrathin porous TiO2 coating for selective gas adsorption. *Chem. Commun.* **51**, 373-375 (2015).
17 Song, Z. N. *et al.* Continuously Adjustable, Molecular-Sieving "Gate" on 5A Zeolite for Distinguishing Small Organic Molecules by Size. *Sci. Rep.* **5, 13981** (2015).
18 Kresge, C. T., Leonowicz, M. E., Roth, W. J., Vartuli, J. C. & Beck, J. S. Ordered mesoporous molecular sieves synthesized by a liquid-crystal template mechanism. *Nature* **359**, 710-712 (1992).

19 Nam, G.-M., Jeong, B.-M., Kang, S.-H., Lee, B.-K. & Choi, D.-K. Equilibrium Isotherms of CH4, C2H6, C2H4, N2, and H2 on Zeolite 5A Using a Static Volumetric Method. *Journal of Chemical & Engineering Data* **50**, 72-76 (2005).
20 Saha, D. & Deng, S. Structural stability of metal organic framework MOF-177. *The Journal of Physical Chemistry Letters* **1**, 73-78 (2009).
21 Gándara, F., Furukawa, H., Lee, S. & Yaghi, O. M. High methane storage capacity in aluminum metal–organic frameworks. *J. Am. Chem. Soc.* **136**, 5271-5274 (2014).
22 Mendoza-Cortes, J. L., Pascal, T. A. & Goddard III, W. A. Design of covalent organic frameworks for methane storage. *The Journal of Physical Chemistry A* **115**, 13852-13857 (2011).
23 Mendoza-Cortés, J. L., Han, S. S., Furukawa, H., Yaghi, O. M. & Goddard III, W. A. Adsorption mechanism and uptake of methane in covalent organic frameworks: theory and experiment. *The Journal of Physical Chemistry A* **114**, 10824-10833 (2010).

CHAPTER 7:

CONCLUSIONS

This thesis mainly focuses on study the preparation of porous metal oxide coatings by molecular layer deposition (MLD) and its application on porous materials pore size modification for selective adsorption separation, water purification and gas storage.

First, we demonstrated a completely new concept, pore misalignment, to continuously fine-tune the effective pore size of 5A zeolite by changing microporous Al_2O_3 coating thickness prepared by MLD for small organic molecules separation, whereas the internal cavity of zeolites are be maintained. This novel concept has great potential to be utilized to fill pore size gaps of the zeolite family and to design zeolite-based molecular-sieving sorbents for selective separation of molecules with very small size differences.

In addition to studying Al_2O_3 MLD porous coatings, ultrathin porous TiO_2 coatings were also deposited by MLD on 5A zeolite surface to modify zeolite pores. The effective pore size of 5A zeolite was reduced to be smaller than the size of butane (0.46 nm) by a ~25-nm thick MLD TiO_2 coating. As a result, The TiO_2 MLD coated zeolite showed great potential for achieving propylene/propane separation based on both equilibrium and diffusivity difference.

Additionally, we found that the adsorptive separation performance of TiO_2 MLD coated zeolite (5A and 13X) sorbents can be further modified by varying the calcination

conditions. The optimized composite sorbents showed greatly improved CO_2/N_2 selectivity while maintaining high CO_2 adsorption capacity. Specifically, our sorbents showed a CO_2/N_2 selectivity as high as 43-77 and CO_2 adsorption capacity of 1.04-2.32 mmol/g at 0.5 bar and room temperature. Their separation performance is superior to most of the reported sorbents for CO_2 capture.

Moreover, TiO_2 nanofiltration membranes were prepared for the first time by using MLD technique. Influence of cycles of MLD on hybrid coating quality was investigated. Our results showed a defect-free, dense titanium alkoxide MLD coating was formed after complete pore filling on anodic alumina oxide (AAO) support, and approximately 1 nm pores can be effectively generated by calcination at 250^oC in air. The AAO-60TiO_2 membrane showed a high pure water permeability of 48 L/(m^2·h·bar) and high rejection for methylene blue and natural organic matter, moderate rejection for salts, and good antifouling performance as well as recovery capability. Compared with traditional sol-gel method, MLD has the potential advantages of precise pore size control, simple fabrication process, and ability to scale up. We expect MLD will become a new method for preparing TiO_2 nanofiltration membranes with well controlled thickness, composition, and membrane pore sizes.

Finally, a novel concept of utilizing nanoporous coatings as effective nano-valves on microporous adsorbents was developed for high capacity natural gas storage at low storage pressure. Using 5A zeolite as a model adsorbent, ~7.5 μm thick, optimized MCM-48 coating with an average pore size of 3.25 nm was deposited on the external surface of the 5A beads. The nanopores of the MCM-48 coating functioned as a valve that can be opened and closed on demand. CH_4 was loaded at high pressure (50 bar) with the nano-

valve open. The nano-valve was closed by adsorbing DMB in the pores of MCM-48 coating when the adsorbent was fully loaded. The loaded adsorbent can be stored at low pressure (~1bar) and the nano-valves can be opened again for releasing the stored CH_4 by desorbing DMB. After 4 h storage at low pressure (1 bar), MCM-48 coated 5A adsorbent can hold 44.1% (32.2 V/V) of the maximum capacity of bare 5A beads (73 V/V). After further pore size reduction to ~1.4 nm by MLD technique, the CH_4 storage capacity increased to 55.8-58.4% (40.7-42.6 V/V) of the maximum capacity of the bare 5A beads, which was about 200% higher than storage capacity of the bare 5A beads at the same storage pressure.